

# Mechanical Spectroscopy of Interface Stress Relaxation in Magnesium Matrix Composites

THÈSE N° 4538 (2009)

PRÉSENTÉE LE 4 DÉCEMBRE 2009

À LA FACULTÉ SCIENCES DE BASE

INSTITUT DE PHYSIQUE DE LA MATIÈRE CONDENSÉE

PROGRAMME DOCTORAL EN PHYSIQUE

ÉCOLE POLYTECHNIQUE FÉDÉRALE DE LAUSANNE

POUR L'OBTENTION DU GRADE DE DOCTEUR ÈS SCIENCES

PAR

Abu Salek Md. Fahim CHOWDHURY

acceptée sur proposition du jury:

Prof. O. Schneider, président du jury

Prof. R. Schaller, Dr D. Mari, directeurs de thèse

Prof. N. Baluc, rapporteur

Prof. F. Chmelik, rapporteur

Prof. J. San Juan, rapporteur



ÉCOLE POLYTECHNIQUE  
FÉDÉRALE DE LAUSANNE

Suisse  
2009



To my parents and my wife Tamanna



## Abstract

Magnesium matrix composites made of pure (99.98%) magnesium reinforced with long carbon (Mg/C) and stainless steel (Mg/steel) fibers were processed by low pressure infiltration method. Mg/C composites were then oriented from the crystallographic point of view by Bridgman technique and finally three composites were obtained with  $\gamma = 0^\circ$ ,  $45^\circ$  and  $90^\circ$  ( $\gamma$  is the angle between the matrix-fiber interface and the normal to the basal plane). The results show that the damping level in the composite for  $\gamma = 0^\circ$  is almost 3 and 7 times higher than that of the composites with  $\gamma = 45^\circ$  and  $\gamma = 90^\circ$ , respectively.

From the result analysis it was possible to conclude that the damping originates in the hysteretic motion of dislocations in the magnesium matrix. As such a mechanism is not thermally activated, high damping is observed over a broad frequency range.

The complete evolution of the mechanical loss as a function of the vibration amplitude has been measured. The obtained result has been found to be in excellent agreement with the Granato-Lücke model for dislocation breakaway. The fit of the experimental points with the theoretical curve and the straight Granato-Lücke plot confirm that the microstructure evolution is controlled by the breakaway of dislocation segments from randomly segregated point defects (hysteretic damping). According to the Granato-Lücke model the critical stress for the breakaway could be estimated.

As a consequence of this analysis, the transient damping due to interface thermal stress relaxation has been interpreted by a model based on a solid friction mechanism. It has been shown that the model of Mayencourt and Schaller justifies the whole mechanical loss behavior. The model predicts two fit parameters  $C_1$  and  $C_2$ , which account for the respective evolution of the mobile dislocation density and interfacial strength. An anomalous behavior is observed for the parameter  $C_2$  as well upon heating as upon cooling, which is being reflected in the shear modulus evolution. This anomalous behavior is due to a “bonding-debonding” mechanism at the fiber-matrix interface due to the motion of dislocations, which depends on the orientation of the glide plane. Also, at high temperature, the interface is strong, which

helps in creep resistance of the composite, and at low temperature, the interface is weak, which is positive for improving toughness by interface crack deflection.

## **Key words**

(1) Metal matrix composites, (2) mechanical spectroscopy, (3) damping, (4) interface, (5) magnesium, (6) carbon fiber, (7) steel

## Résumé

Des matériaux composites à matrice de magnésium pur (99.98 %) renforcée par des fibres longues de carbone (Mg/C) ou d'acier (Mg/steel) ont été élaborés par infiltration basse pression. Certains composites Mg/C ont ensuite été orientés du point de vue cristallographique au moyen de la technique de Bridgman. On a ainsi obtenu trois variantes de Mg/C, différentes l'une de l'autre par l'angle  $\gamma$  que fait la normale au plan basal de la structure hexagonale du Mg avec l'interface fibre-matrice, càd.  $\gamma = 0^\circ$ ,  $45^\circ$  et  $90^\circ$ . Les résultats montrent que le niveau d'amortissement dans le cas.  $\gamma = 0^\circ$  est environ 3 et 7 fois supérieur à celui obtenu dans les composites  $\gamma = 45^\circ$  et  $\gamma = 90^\circ$ , respectivement.

A partir de l'analyse des résultats, il a été possible de conclure que l'origine de l'amortissement est le mouvement hystérétique des dislocations dans la matrice de magnésium. Comme un tel mécanisme n'est pas activé thermiquement, le fort amortissement est observé sur un large domaine de fréquence.

Ainsi, l'évolution complète des pertes mécaniques en fonction de l'amplitude des oscillations a été mesurée. Le résultat obtenu est en excellent accord avec le modèle de Granato-Lücke concernant le désancrage des dislocations de défauts ponctuels répartis aléatoirement. L'ajustement de la courbe théorique sur les points expérimentaux ainsi que le graphe de Granato-Lücke ont permis de déduire la valeur de la contrainte critique de désancrage des dislocations.

En conséquence de cette analyse, le frottement intérieur transitoire associé à la relaxation des contraintes thermiques aux interfaces a été interprété par un modèle basé sur le mouvement de dislocations contrôlé par des forces de frottement sec. Dans ce contexte, on montre que le modèle de Mayencourt et Schaller permet une interprétation complète du comportement des pertes mécaniques. Ce modèle donne accès à deux paramètres d'ajustage des courbes théoriques sur les points expérimentaux :  $C_1$  et  $C_2$ .  $C_1$  rend compte de l'évolution de la population de dislocations mobiles qui relaxent les contraintes d'interface, et  $C_2$  de la qualité de l'interface. Un comportement anormal du paramètre  $C_2$  est observé aussi bien au chauffage qu'au refroidissement, comportement qu'on retrouve dans l'évolution du module de cisaillement. Cette anomalie serait due à un mécanisme de « prise et perte » du contact à

l'interface fibre-matrice par le mouvement des dislocations et qui dépend de l'orientation de la matrice. Ainsi à haute température le contact est bon, ce qui favorise la résistance au fluage des composites à matrice magnésium, et à basse température le contact est moins bon, ce qui augmente la ténacité du composite par déviation des fissures le long des interfaces.

## **Mots-clés**

(1) Composites à matrice métallique, (2) spectroscopie mécanique, (3) amortissement, (4) interface, (5) magnésium, (6) fibres de carbone, (7) acier



# List of contents

<b>INTRODUCTION .....</b>	<b>1</b>
<b>CHAPTER 1: PROPERTIES OF METAL MATRIX COMPOSITES .....</b>	<b>5</b>
1.1 THE METAL MATRIX COMPOSITES .....	5
1.1.1 Matrix .....	6
1.1.2 Reinforcement.....	7
1.1.3 Interface.....	8
1.2 PROCESSING.....	8
1.3 THERMO-MECHANICAL PROPERTIES OF MMC'S .....	9
1.3.1 The elastic constants.....	10
1.3.2 Thermal stresses .....	12
1.3.3 Interfacial response .....	13
1.3.4 Thermal fatigue.....	14
1.3.5 Plastic deformation.....	15
1.4 LITERATURE REVIEW .....	16
1.4.1 Work with magnesium matrix composites .....	19
1.5 AIM OF THE RESEARCH.....	23
<b>CHAPTER 2: MECHANICAL SPECTROSCOPY.....</b>	<b>25</b>
2.1 ANELASTICITY .....	25
2.2 THERMAL ACTIVATION .....	28
2.3 MEASUREMENT OF INTERNAL FRICTION/MECHANICAL LOSS IN A PENDULUM .....	29
2.3.1 Free pendulum: (resonant system).....	30
2.3.2 Forced oscillations: (sub resonant mode).....	31
2.4 RELAXATION PHENOMENON IN METAL MATRIX COMPOSITES .....	32
2.4.1 Relaxation due to the dragging of solute atoms by dislocations .....	32
2.4.2 Relaxation due to hysteretic damping and Granato-Lücke model .....	33
2.4.3 Crack propagation and thermal fatigue .....	36
2.5 MODEL OF MAYENCOURT AND SCHALLER .....	37
2.5.1 Viscous friction mechanism.....	38
2.5.2 Solid friction mechanism .....	40

2.6 MECHANICAL SPECTROSCOPY WITH MAGNESIUM AND ITS COMPOSITES.....	42
<b>CHAPTER 3: SAMPLE PREPARATION AND EXPERIMENTAL TECHNIQUES ..</b>	<b>45</b>
3.1 SPECIMEN PROCESSING BY GAS PRESSURE INFILTRATION.....	45
3.2 THE PREFORMS .....	47
3.3 CRYSTALLOGRAPHIC ORIENTATION OF THE MATRIX .....	48
3.3.1 Directional solidification.....	48
3.3.2 Bragg-Brentano X-ray analysis.....	49
3.4 NOMENCLATURE OF THE PROCESSED SAMPLES .....	51
3.5 CHARACTERIZATION BY MICROSCOPY .....	52
3.6 MECHANICAL SPECTROSCOPY.....	53
3.6.1 Free decay torsion pendulum: (resonant system).....	53
3.6.2 Forced pendulum: (sub resonant mode).....	54
3.6.3 Free-free vibrating rod installation.....	56
<b>CHAPTER 4: EXPERIMENTAL RESULTS AND ANALYSIS.....</b>	<b>59</b>
4.1 CHARACTERISTIC MECHANICAL LOSS AND CORRESPONDING SHEAR MODULUS SPECTRA	59
4.2 EFFECTS OF THE HEATING AND COOLING RATE $\dot{T}$ AND OF THE VIBRATION FREQUENCY $\omega$ .....	64
4.3 ANALYSIS OF THE TRANSIENT DAMPING BY THE MODEL OF MAYENCOURT.....	68
4.4 THERMAL HYSTERESIS .....	71
4.5 MODULUS ANOMALY .....	72
4.6 CONCLUSION .....	75
<b>CHAPTER 5: STUDY OF DISLOCATION DAMPING DUE TO SOLID FRICTION</b>	<b>77</b>
5.1 HYSTERETIC MOTION OF DISLOCATIONS .....	77
5.2 ANALYSIS OF THE MECHANICAL LOSS SPECTRUM OF Mg/STEEL .....	78
5.3 EFFECTS OF THE VIBRATION AMPLITUDE.....	82
5.3.1 Intrinsic damping.....	82
5.3.2 Transient damping.....	84
5.4 DISCUSSION .....	84
5.5 CONCLUSION .....	85
<b>CHAPTER 6: CRYSTALLOGRAPHIC ORIENTATION OF THE MATRIX AND INTERFACE QUALITY .....</b>	<b>87</b>
6.1 EFFECT OF MATRIX ORIENTATION ON THE MECHANICAL LOSS SPECTRA.....	87

6.2 SPECTRUM ANALYSIS .....	92
6.2.1. <i>Damping level as a function of matrix orientation</i> .....	92
6.2.2. <i>C<sub>1</sub> and C<sub>2</sub> parameters as a function of matrix orientation</i> .....	97
6.2.3 <i>Effect of matrix orientation on the modulus anomaly</i> .....	101
6.2.4. <i>C<sub>1</sub> and C<sub>2</sub> parameters as a function of interface nature</i> .....	103
6.3 INTERFACIAL RESPONSE DUE TO MECHANICAL LOSS .....	105
6.4 CONCLUSION .....	106
<b>CHAPTER 7: GENERAL DISCUSSIONS.....</b>	<b>109</b>
<b>CONCLUSION .....</b>	<b>117</b>
<b>REFERENCES .....</b>	<b>119</b>
<b>APPENDIX.....</b>	<b>127</b>
<b>ACKNOWLEDGEMENTS .....</b>	<b>131</b>
<b>CURRICULUM VITAE .....</b>	<b>133</b>



## Introduction

Metal matrix composites (MMCs), because of their multi phase structure can offer a solution to the needs of light materials in the transportation industry and in structural application because they allow the combination of good mechanical properties and a high damping (Fleteren 1996). High damping materials allow undesirable mechanical vibration and wave propagation to be suppressed passively, which is proved to effective in control of noise and enhancement of vehicle and instrument stability. Pure magnesium exhibits the highest damping capacity among all commercial metallic materials (Ritchie 1987, Reihani 1979, Riehemann 1998, Sugimoto 1977), while poor mechanical properties for instance low mechanical strength prevents its wide application. The incorporation of a reinforcement such as fibers can compensate some of these limitations leading to engineering materials with high specific properties and improved wear resistance. Actually, with proper engineering, magnesium matrix composite can exhibit superior properties neither of the constituents alone can possess. The good mechanical properties and the in service life-time of such composites depend on the fiber-matrix interfacial strength, which is influenced by the load transfer between the metallic phase and the reinforcement.

Due to the change of temperature, thermal stresses arise at the interface because of the mismatch of thermal expansion coefficients between the matrix and the reinforcement. Relaxation of these interfacial thermal stresses plays an important role on the final mechanical properties of the composite. Thermal stresses can be relaxed either by interface debonding or by crack propagation. They are also relaxed by the creation and motion of dislocations, which instead preserves the interfacial bonding. Thus, it is very important to analyze the microstructure and understand the mechanism of relaxation in order to predict a possible degradation of the composite properties.

Mechanical spectroscopy (MS) is a non-destructive method to investigate the micro-structural mechanisms. It measures the energy dissipated in the material submitted to periodic oscillations, which in turns evaluates the damping capacity of the material. MS is very sensitive to the dynamics of the crystal defects in the material, which are responsible for the relaxation mechanism. Mechanical spectroscopy has already been used to investigate the

relaxation of thermal stresses at the interfaces of the metal matrix composites (Carenno-Morelli 2001).

Thermal stresses can be relaxed either by interface debonding or by crack propagation leading to damage accumulation in the matrix (Parrini 1996). They are also relaxed by the creation and motion of dislocations, which instead preserves the interfacial bonding. In fact, interfacial thermal stresses arising during heating or cooling induce an additional damping in the mechanical spectroscopy measurements superimposed on isothermal equilibrium damping. This additional response, which depends on the temperature variation rate  $\dot{T}$  and on the excitation frequency  $\omega$  can be referred to as transient damping.

Mayencourt and Schaller (Mayencourt 1998) have interpreted thermal stress relaxation in the magnesium matrix composites as due to hysteretic motion of dislocations from matrix-fiber interface. The model shows an evolution of the dislocation density and of the interfacial bonding as a function of the temperature. They have observed a non-linear relationship between the transient mechanical loss ( $\tan \phi_{Tr}$ ) and the measurement parameters  $\dot{T}/\omega$  for the case of Mg/Mg<sub>2</sub>Si, Mg/C and Mg/Al<sub>2</sub>O<sub>3</sub> composites. Couteau has observed a strong dependence of the fiber orientation on the transient mechanical loss ( $\tan \phi_{Tr}$ ) in the case of Mg/SiC composites (Couteau 2004). When a shear stress is applied, the transient damping has a much higher value for a rectangular bar shaped composite when the fibers are oriented perpendicular to the composite main axis than the fibers oriented along the of the composite axis.

The thermal stress relaxation at the interface of magnesium composites is mainly governed by the motion of dislocations along the glide plane, which is the basal plane (001). Dislocations are pinned by impurity atoms and when they experience a stress higher than the pinning stress, they breakaway from the pinning points and glide in the matrix. During mechanical spectroscopy measurements, an additional mechanical stress is imposed to the composite and depinning of the dislocation segments occurs only when the total stress (mechanical and thermal stresses) is larger than the critical stress for breakaway. Thus, the orientation of the glide plane is very important for the dislocations to achieve a favorable condition for gliding in order to increase the damping.

The type of the reinforcement plays a major role on the damping. The reinforcing element is chosen by considering the thermal expansion coefficient difference with the matrix as well as its elastic modulus. Magnesium and its alloys have been used as matrix and have been reinforced with different fibers. In this work, we have investigated magnesium reinforced with long C and stainless steel fibers. Both fibers have an excellent mechanical strength. Steel fibers have a low cost for fabrication. Moreover, they have a larger diameter compare to the other fibers. Thus by reducing the number of fibers, we can obtain a homogeneous distribution in the matrix.

The main goal of this work is to study the effect of the orientation of the matrix (from the crystallographic viewpoint) on the damping capacity and the interfacial strength of magnesium matrix composites.





# Chapter 1: Properties of metal matrix composites

## 1.1 The Metal Matrix Composites

Depending on the bonding between atoms, a material can be characterized into three distinct groups: metal, ceramic and polymer (Ashby 1996). Metallic bonding is characterized by delocalized electron gas, while the ceramic is composed of covalent or ionic bonding between the constituent atoms. The polymers form long carbon chains, which are interacting by Van der Waals type bond. Because of the strength of the covalent bond, the ceramics are very rigid, while the metals are more ductile and have a higher damping capacity. The polymers have a much lower density and rigidity than the metals and the ceramics.

However, several applications (transportation system, machine tools industries) require a material having the mechanical strength of a ceramic as well as the toughness and the high damping capacity of a metal together. A high damping capacity is observed in materials exhibiting poor mechanical properties, for instance low yield stress or hardness (such as magnesium). On the contrary, materials with good mechanical strength show a very low level of damping (such as steel). One can achieve good mechanical properties and a high damping capacity together by designing a composite material with two or more distinct phases, where the microscopic mechanism responsible for the dissipation of energy and the hardening mechanism are obtained separately by each phase (Sugimoto 1978).

Composite materials are applied since the middle of the twentieth century. They were first designed for military needs (Schwartz 1996, Miracle 2001). For instance, since 1940 composite materials were used in military aircrafts, tanks and radars. The use of metallic composites started in the fifties. The goal was to strengthen metallic materials while reducing their density. The development of boron and later SiC monofilament, during 1960-1970, largely contributes to the new fiber reinforced composites. The composites with long fibers were introduced after 1980. Composite materials are now used in a large number of applications: automobile, aerospace, electronic and construction (fig.1.1b) (Schwartz1996). For example, composites reinforced with SiC particle (Durante 1997, Sallit 1989) are used to manufacture rotors due to their excellent wear resistance. Adding rings of alumina fiber

reinforced composites in the piston of an engine increases the wear resistance (Rohatgi 1991). Al matrix composites reinforced with SiC are used in the electronic industry for packaging because of high thermal conductivity and low density (which is provided by the metallic matrix) and a low thermal expansion coefficient. The goal is to have a thermal expansion coefficient similar to those of the semiconductor like silicon of the order of  $5 \cdot 10^{-6}$  (Zweben 1988).

Because of their special construction, metal matrix composites (fig.1.1a) have high strength, high elastic modulus, high toughness and impact properties, high electrical and thermal conductivity, major weight savings due to higher strength to weight ratio, exceptional dimensional stability, higher creep resistance and improved cyclic fatigue resistance (Chawla 2006)). The character of the composites depends on the matrix, the reinforcement and the interface.

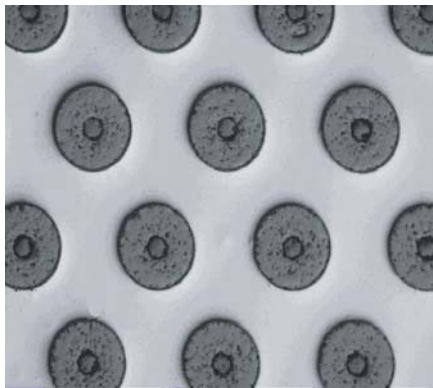


Fig. 1.1a: Titanium/SiC composites (Courtesy: University of Bristol, Department of Aerospace Engineering).



Fig. 1.1b: Aluminum matrix composite components used for power generation, high speed machinery and automotive applications (Courtesy: Composite Metal Technologies PLC).

### ***1.1.1 Matrix***

The matrix is the continuous material medium into which the reinforcement is embedded. Its main function is to transfer and distribute load to the reinforcements or fibers. This transfer of loads depends on the bonding interface between the matrix and the reinforcement and also on the fabrication technique. The matrix can be selected on the basis of oxidation and corrosion resistance or other properties. Almost all the structural alloy systems have been considered

for the matrix. For instance, alloys based on Al, Cu, Fe, Mg, Ti, Ni, Zn, Sn, Si, Ag, Co and Pb. However, aluminum and magnesium are more commonly used as the matrix element. In structural applications, the matrix is usually a light metal such as aluminum, magnesium or titanium, and provides a compliant support for the reinforcement. In high temperature applications, cobalt and cobalt-nickel alloy matrices are common. The chemical composition of the matrix is very important. Magnesium has been considered in this work as the matrix constituent because of its low density and high damping capacity (Reihani 1979, Sugimoto 1978, Riehemann 1998).

### ***1.1.2 Reinforcement***

The reinforcing material is embedded into the matrix, which increases the strength, stiffness and temperature resistivity. The prime role of the reinforcements is to carry the load. The reinforcement can be either continuous, or discontinuous. Discontinuous reinforcements such as whiskers, short fibers, or particles can be worked with standard metalworking techniques, such as extrusion, forging or rolling. Particles may have a dimension between 5-20  $\mu\text{m}$ . Different kinds of particles can be made in different ways: for instance, SiC is processed by reacting silica in the form of sand and carbon in the form of coke at 2400°C in an electric furnace, WC is obtained by carburization of tungsten metal, while the alumina  $\text{Al}_2\text{O}_3$  can be produced by a sol-gel process. Whiskers are mono crystalline short fibers with extremely high strength. This high strength is due to the absence of crystalline imperfections such as dislocations. Being mono crystalline there are no grain boundaries either. They have a length of few mm and a diameter of few  $\mu\text{m}$  and an aspect ratio between 50 and 10000.

Continuous reinforcement is obtained with monofilament wires, sheets or fibers such as carbon fibers, stainless steel fibers or silicon carbide fibers. Since the fibers are embedded into the matrix in a certain direction, the result is an anisotropic structure in which the alignment of the material affects its strength. Any material (metal, ceramic), which can be transformed into fibrous form can be used as a reinforcement. Fibers have a high degree of flexibility, higher strength than the bulk material of the same composition (Chawla 2006).

### ***1.1.3 Interface***

Because of the multiphase structure in the interface of the MMCs, there is a discontinuity in the chemical composition, elastic modulus, thermal expansion coefficient, and other thermodynamic properties such as the chemical potential. As the interfacial area per unit volume in the MMCs is very large, it plays an important role on the final properties of the composites. The interfacial zone will be at thermodynamic equilibrium only at temperatures where the two components are brought together. When the temperature is changed, a complex stress field exists because of the difference of thermal expansion coefficients between different layers. These stresses will be proportional to the difference in the elastic moduli of the components, to the difference in the thermal expansion coefficients and to the temperature difference between the initial equilibrium and the final temperature. In order to minimize the free energy, the phases in the interface will be involved in the generations of dislocations, grain boundary migration, crack nucleation and propagation. A good interface should have a strong bond between the matrix and the reinforcement and promote load transfer from the matrix to the reinforcement.

## **1.2 Processing**

There are many ways by which a reinforcement can be incorporated into a metallic matrix. Each technique has its own limitations in terms of component size and shape and imposes certain micro structural features on the product. Making the right choice of the fabrication procedure is important for the microstructure and the performance of a component as well for its commercial viability. Most of the fabrication processes involve processing in the liquid or solid state. Deposition techniques are also used.

The main solid state methods are based on powder metallurgy techniques (Ghosh 1993), which typically involve discontinuous reinforcements. The ceramic and metal powder are mixed, cold compacted, hot pressed and then undergo extrusion or forging. (Lloyd 1997).

Liquid metal infiltration of ceramic preforms is a usual technique to produce metal matrix composites. In this process, near net-shape composites are processed with a faster rate of casting at a relatively low temperature. The common liquid casting techniques are described below.

In squeeze casting method, liquid metal is infiltrated into a fibrous or particulate preform by applying a pressure (Clyne 1987, 1993). The molten metal is pushed by a piston into the heated preform by applying a pressure in the range between 50-100 MPa. Composites fabricated by the squeeze casting method have minimal reaction between fiber and the molten metal because of the short time of contact. This process has some disadvantages though. The application of high pressure can lead to fiber damage and inhomogeneous fiber distribution along the infiltration direction. Also the matrix exhibits porosity caused by gas entrapped during the processing (Janczak 1994).

In order to overcome the problems of squeeze casting, the low pressure infiltration method has been developed, in which the infiltration pressure is substantially reduced by using vacuum for preform outgasing. This avoids air entrapment (Mortensen 1988, Mortensen 1998, Masur 1989). As a consequence, a low cost facility can be developed using gas pressure to achieve infiltration. Complex shaped structures with high volume fractions of fibers can be obtained in this method under the controlled environment of a pressure vessel. Low pressure infiltration was used in this work for the fabrication of all the samples.

### **1.3 Thermo-mechanical properties of MMC's**

Metal matrix composites show a combination of mechanical stiffness from the reinforcement, a relatively low density and a high damping capacity from the metallic matrix. This combination makes it an attractive material for aerospace and relatively high temperature applications. Strengthening a MMC depends on its constituents: the matrix and the fibers. Most reinforcements are essentially elastic up to their fracture point, while the matrix undergoes plastic deformation. The interface region, however can suffer changes just as the matrix does during processing or service. Processing induced reactions and thermal stresses can cause changes in the matrix microstructure. These microstructural changes in the matrix in turn can affect the mechanical and physical behavior of the composite (Gang 1994). After infiltration due to the difference in the thermal expansion coefficients, thermal stresses arise at the interface. The final mechanical properties of the composite depend on the relaxation mechanism of these thermal stresses.

### 1.3.1 The elastic constants

The elastic modulus is one of the important properties taken into account when designing structural parts. If the Young's modulus is increased then it is usually possible to decrease the components thickness and therefore reduce the weight. The increase of the modulus at a given thickness also increases the stiffness. The elastic modulus of a composite material depends on the modulus of individual constituents: the matrix and the reinforcements. It also depends on the orientation and geometry of the reinforcements. The elastic modulus of a composite represents the stiffness of the composite. The applied stress  $\sigma_c$  is shared by both the matrix and fiber; the stress in each phase is proportional to its stiffness.

By applying an isostrain condition i.e.  $\epsilon_f = \epsilon_m = \epsilon_{cl} = \frac{\Delta l}{l_0}$ , the longitudinal Young's modulus  $E_{cl}$  (see fig.1.2) of the composite can be expressed by using the law of mixtures:

$$E_{cl} = V_f E_f + V_m E_m \quad (1.1)$$

Where  $f$ ,  $m$  and  $c$  denote the fiber, matrix and composite respectively and  $l$  denotes the longitudinal direction with respect to the fiber.  $V_f$  and  $V_m$  are the volume fractions of the fiber and matrix. Eq. 1.1 says that the elastic stiffness of the composite is a volume weighted average of the strength of the fiber and matrix (Chawla 2006).

By applying an isostress condition i.e.  $\sigma_f = \sigma_m = \sigma_{ct}$  and using the law of mixture one can calculate the transverse Young's modulus  $E_{ct}$  (see fig.1.2), which is

$$\frac{1}{E_{ct}} = \frac{V_m}{E_m} + \frac{V_f}{E_f} \quad (1.2)$$

Both the fiber and the matrix are subjected to the same shear stress and the shear modulus  $G$  can be expressed as

$$\frac{1}{G} = \frac{V_m}{G_m} + \frac{V_f}{G_f} \quad (1.3)$$

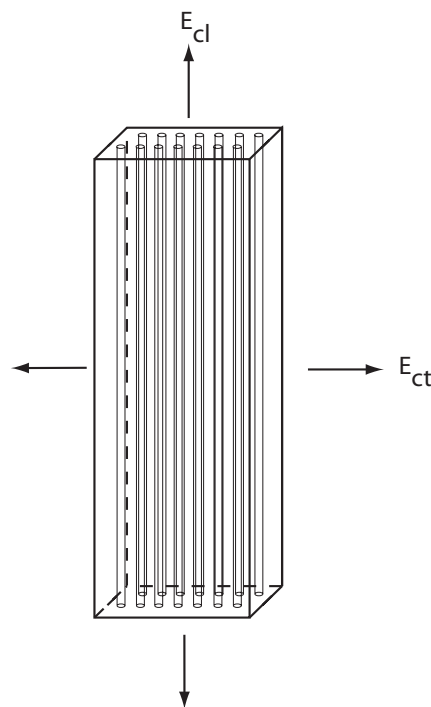


Fig.1.2: Schematic diagram of a long fiber reinforced metal matrix composite with the indication of the longitudinal ( $E_{cl}$ ) and transverse ( $E_{ct}$ ) Young's modulus.

As an example, fig. 1.3 shows that the Young's modulus for an Al9Si3Cu based composites depends on the volumetric fraction of the alumina fibers (Dinwoodie 1985).

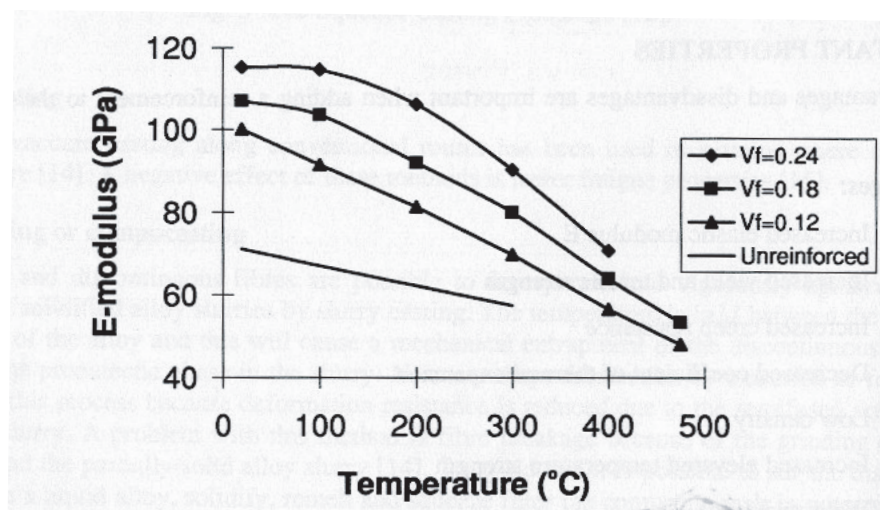


Fig. 1.3: E (Young's) modulus vs. temperature for an alloy Al9Si3Cu alloys with different amounts alumina fibers (Dinwoodie 1985).

### 1.3.2 Thermal stresses

The discontinuity in the thermal expansion coefficients causes thermal stresses to appear at the interface of the metal matrix composites. The thermal stresses generated depend on the reinforcement volume fraction, reinforcement geometry, thermal expansion coefficient mismatch, temperature interval (Chawla 2006, Arsenault 1989, Hull 1996). Thermal stresses due to a thermal mismatch will generally have a complex mathematical form, depending on the geometrical model chosen for a given composite.

The thermal stresses induced in a continuous fiber metal-matrix composite can be estimated by a simple one-dimensional model (fig. 1.4) (Taya 1989). The model is based on the assumption that the composite is initially stress free (fig. 1.4a) where as the moduli and coefficient of thermal expansions of the matrix and the fiber are denoted by  $E_m$  and  $E_f$ , and  $\alpha_m$  and  $\alpha_f$  respectively. If the temperature is increased by an amount  $\Delta T$ , then each phase in the composite would expand freely by  $\alpha_i \Delta T$  with  $i = m$  or  $f$  phase under no stress (fig. 1.4b). Due to the requirement of isostrain, the matrix is compressed while the fiber is stretched (fig. 1.4c). Denoting the isostrain measured from the initial stage by  $\varepsilon_c$ , one can establish the equilibrium in force along the axial direction

$$-\alpha_m V_m + \alpha_f V_f = 0 \quad (1.4)$$

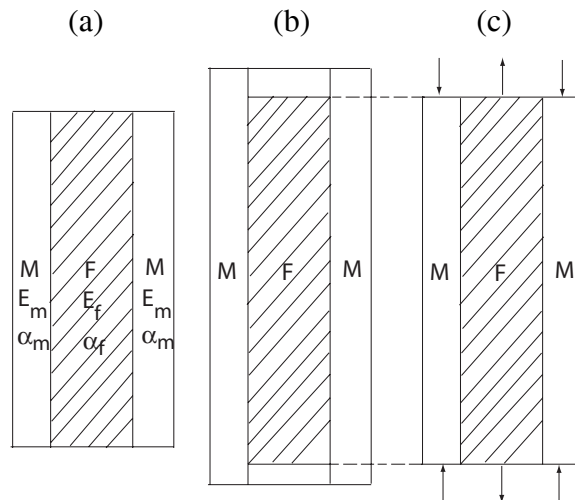


Fig. 1.4: One dimensional model for the analysis of the thermal stress in a continuous fiber metal matrix composite subjected to temperature change  $\Delta T (>0)$  where  $\alpha_m > \alpha_f$  was assumed, (a) initial configuration, (b) stress free configuration and (c) final equilibrium configuration.



Hooke's law holds for each phase:

$$\alpha_m \Delta T - \varepsilon_c = \frac{\sigma_m}{E_m} \quad (1.5)$$

$$\varepsilon_c - \alpha_f \Delta T = \frac{\sigma_f}{E_c} \quad (1.6)$$

From eqs. (1.4), (1.5) and (1.6), the thermal stresses in the matrix and the fiber can be obtained as

$$\sigma_m = \frac{V_f E_m E_f \Delta \alpha \Delta T}{E_c} \quad (1.7)$$

$$\sigma_f = \frac{V_m E_m E_f \Delta \alpha \Delta T}{E_c} \quad (1.8)$$

Here  $E_c$  is the modulus of the composite and is given by the law of mixture (eq.1.1). The analysis of the thermal stress field in the actual metal matrix composites is not so simple above and it requires more accurate models.

### ***1.3.3 Interfacial response***

The thermal stresses in the metal matrix composites are responsible for different phenomena. The metallic matrix is ductile, while the fiber is stiffer and has a higher elastic modulus. Under an applied stress, the fiber deforms first elastically. When the stress exceeds the matrix elastic limit, the matrix then deforms plastically. Load transfer occurs between the matrix and the fiber. If the load of the fiber exceeds its rupture strength, fracture occurs. Thus, it is evident that for this kind of material the mechanical behavior depends on the interface where the load transfer occurs i.e. the stress relaxation mechanism at the interface. When the interfacial stress is relaxed by the movement of dislocations, the mechanical resistance is improved. On the contrary, when the stress is relaxed by crack propagation and damage accumulation, the result is the degradation of the mechanical properties of the composite.

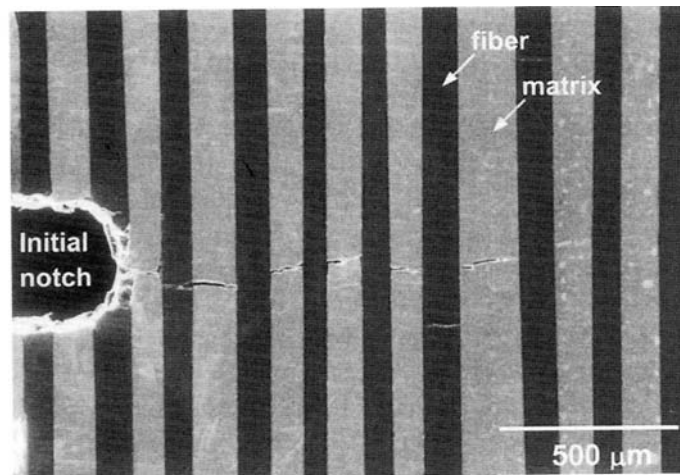


Fig. 1.5: Fatigue crack growth in a Ti- $\beta$ -21s/SiC<sub>f</sub>/SCS-6 composite exhibiting interfacial debonding (Chawla 2006).

The fatigue behavior of a composite is dominated by the fracture of the fibers when the fiber orientation is parallel to that of the stress, because the fiber holds the matrix and damage can occur only by the breaking of the fiber. However, when the fiber orientation is transverse to the stress, damage occurs preferentially by debonding at the interface. Thus, the quality of the interface has little influence on the fatigue resistance when applied stress is parallel to fibers, but it is crucial for the transverse case (Hac 1984, Davidson 1989).

### 1.3.4 Thermal fatigue

Under thermal cycling, the mechanical property of a material will be degraded. This phenomenon is called thermal fatigue (Derby 1991, Kim 1978, Kim 1991, Nakanishi 1989). The composites undergo mechanical fatigue like most other materials. The quality of the reinforcements and their size and shape play an important role in the type of fracture encountered (Miserez 2004). However, the evolution and the relaxation of the thermal stress strongly influence the behavior of the composite. Large internal stresses can occur when fiber reinforced composites are heated and cooled through a temperature range. Thermal fatigue is revealed by a damage accumulation in the matrix leading to cracking (Llorca 1994, Menet 1991, Patterson 1989, Chan 1989) or plastic deformation of the metal matrix around fibers (Daehn 1991).

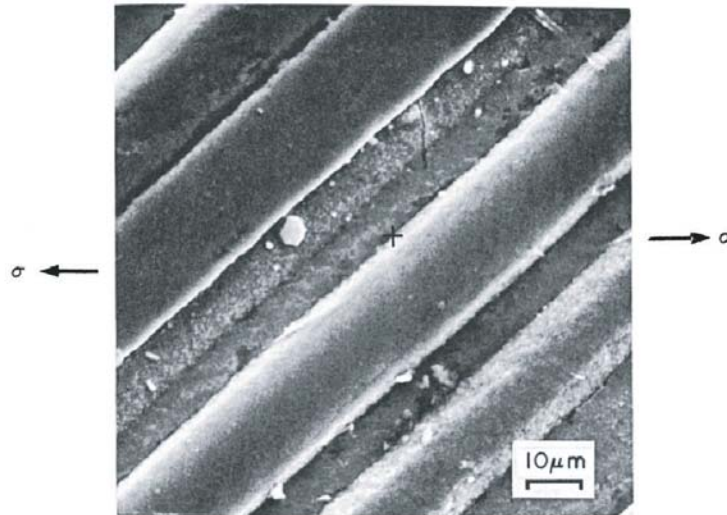


Fig. 1.6: An interface fatigue crack (+) in the ZE41A/Alumina composite with the fibers at 45° angle to the stress axis (Chan 1989).

### 1.3.5 Plastic deformation

When the thermal stresses accumulated at the interface are high enough to exceed the elastic limit of the matrix, dislocations are produced near the vicinity of the reinforcement. Transmission electron microscopy has revealed a variety of dislocation configuration surrounding the reinforcing phase, including long dislocation along the fibers (Arsenault 1983, Suresh 1989, Christman 1988, Rack 1987, Chawla 1991).



Fig. 1.7: End view of the  $\beta$  SiC fibers and surrounding dislocations presumably generated by differential thermal contraction stresses (Arsenault 1983).

The strength of the composite depends on the geometry and the state of the reinforcements (Arsenault 1991). Spherical reinforcements create dislocations distributed symmetrically

around the fiber (Hamann 1991) or in the case of short fiber the dislocation stacked around the edge of the fibers (Xin 1997). In the case of long fibers, the density of dislocation is even higher because of the large aspect ratio (Mortensen 1998).

## 1.4 Literature review

Metal matrix composites are subject to intensive research because of their superior mechanical and thermal properties, which makes them as an attractive candidate in the field of transportation and structural application. The compatibility of the reinforcement and the matrix is one of the major limitations for the liquid phase infiltration of the MMCs. The low-pressure infiltration process was developed for infiltration of Al alloys into ceramic preforms (Demir 2004). The preforms, which contain different amount of porosity, were infiltrated with different pressures and temperatures, which show that not only porosity but also pore size affects the infiltration rate. Infiltration temperature and pressure were both found to be effective for the infiltration but at low infiltration temperature, a high pressure is needed. Al-Si-Mg alloys were infiltrated into  $\text{Al}_2\text{O}_3/\text{SiC}$  preforms in spite of poor wetting properties. Bending behavior of resulting composites exhibits a high strength value. Maximum strength (558 MPa) was obtained for 13 vol.% dual ( $\text{Al}_2\text{O}_3/\text{SiC}$ ) particle reinforced aluminum composites. The infiltration temperature and pressure both increased the relative density, which increases the bending strength of the composites.

AZ91 (Mg-9%Al-1%Zn) and ZE41 (Mg-4%Zn-1%Nd) matrix composites reinforced with short  $\delta$ -alumina fibers (Saffil®) were manufactured by the squeeze casting technology (Trojanová 2004). The structure of composite materials consisted of short  $\delta$ -alumina fibers (approximately 20 vol.%) distributed within the matrix. Compression tests on cylindrical composite samples were carried out at temperatures between 20 and 300 °C. Results revealed that the flow stresses of the composites are substantially higher than those of unreinforced alloy at lower temperatures up to 200-250°C, while at higher temperatures the influence of fibers is not significant.

As it concerns fracture mechanics, model composites made of pure Al reinforced with a high volume fraction (around 50%) of alumina particles were produced by infiltration and tested in tension (CT specimens) (Miserez 2004). Depending on the initial quality of the reinforcement and the particle size, the composites exhibited a large spectrum of fracture response, ranging

from fully stable crack propagation with marked R-curve behavior to unstable fracture and little R-curve behavior. The micromechanism of crack propagation depends on the ceramic type, shape and size. The local work of fracture is estimated using detailed fractographic examinations and simple micromechanical models. The composite fracture energy is proportional to the estimated local fracture energy by a factor between 5 and 10. This proportionality proves that, although the main contribution to the fracture energy is from crack tip plastic dissipation, toughness is governed by the local work of fracture. This study thus provides experimental evidence that microscopic plastic deformation around the crack tip amplifies the local work of fracture. It was also found that Al-Cu matrix composites free of coarse  $\text{Al}_2\text{Cu}$  matrix intermetallics and reinforced with 60 vol.% high-strength polygonal alumina particles exhibit strength/toughness combinations that are in the same range as unreinforced high strength aluminum alloys. The strength of the composites can be increased without decreasing their toughness.

A simple model for describing the competition between interface decohesion and particle cracking as the elementary damage nucleation mechanisms in heterogeneous materials was proposed by Babut et al. (Babout 2004). It allows rationalizing the influence of the plastic behavior of the ductile matrix and of the interfacial strength. The model was applied to analyze the dominant damage mechanisms in model composites with aluminum alloys matrix and spherical zirconia/silica reinforcement. In the case of pure aluminum (low yield stress and medium work hardening rate) decohesion prevails, whereas in Al-Mg-Si alloy matrix with higher yield stress and work hardening rate, particle fracture is the dominant failure mechanism. In addition, it was sometimes observed that the two mechanisms can coexist in the same sample.

Another theoretical approach of the interface was achieved in a three dimensional finite element micro mechanical model developed for studying the effects of various parameters such as thermal residual stress, fiber coating and interface bonding on transverse behavior of a unidirectional SiC/Ti-6Al-4V metal matrix composites (Aghdam 2004). Three different phases, i.e. fiber, coating and matrix together with two distinct interfaces, one between the fiber and coating and the other between coating and matrix were considered in the model. The predicted stress-strain curve for damaged interface demonstrated a good agreement with experimental results.

A shear-lag stress analysis methodology was developed by Mahesh (Mahesh 2004), which accounts for both matrix strain hardening plasticity and interfacial slip in a single fiber metal matrix composite subjected to uniaxial tensile loading and unloading along the fiber direction. The model estimates that two material parameters are crucial: the frictional threshold of the interface and the yield point of the matrix. With these parameters, the elastic strain evolution with load is in excellent agreement with the experimental data. The classical shear lag model was modified to study the elastic-plastic stress transfer in short fiber reinforced metal matrix composites (Jiang 2004). The effect of the matrix plastic deformation on the stress transfer in the elastic range was analyzed by introducing a plastic strain. The modified model was then used to study the effects of thermal residual stresses on the tensile and compressive stress-strain responses of the composite. It was demonstrated that the stress transfer efficiency in the elastic range is reduced due to the matrix local plastic deformation. The model prediction exhibited a very good agreement with the experimental results in a SiCw/Al-Li composite.

The damping properties of the 6061Al/SiCp/Gr hybrid MMC, which was fabricated by spray atomization and deposition, were studied (Gu 2004). The results show that the internal friction spectra of the samples exhibit an internal friction peak as a function of temperature at about 150°C. Furthermore, the peak temperature increases with increasing frequencies, and the activation energy of the internal friction peak was calculated being 1.17 eV according to Arrhenius equation. The internal friction peak is due to dislocation-induced damping, which results from dragging of defects under the double action of heat and stress.

In the MMC Al-Li 8090/SiC, an internal friction peak was observed, which is associated with the relaxation of thermal stresses around the reinforcements by micro plastic deformation (Gutiérrez 2004). The strength of the observed internal friction peak is strongly decreased by precipitation, which decreases the mobility of the dislocations generated by the thermal stress.

A new model to calculate the damping capacity of particle reinforced metal matrix composites (PMMCs) was proposed based on the assumption that the energy loss mainly results from the anelasticity of the particulate and matrix and the micro-plasticity of the matrix under small strain amplitude (Gu 2004). A finite element method with a multi particle model has been used. The results show that the energy loss in the loading direction represent

the total energy consumed in the composites. Moreover, the results calculated with the new model show a good agreement with the Granato-Lücke theory, which demonstrated the feasibility of damping calculation with this method.

Internal friction measurements as a function of constant strain amplitude shows that damage accumulation produced in the AlCu-20%Saffil composite by mechanical fatigue comes with a decrease in the elastic modulus and an increase in internal friction peak (Parrini 1995). The fracture of the specimen occurs after about 90000 cycles.

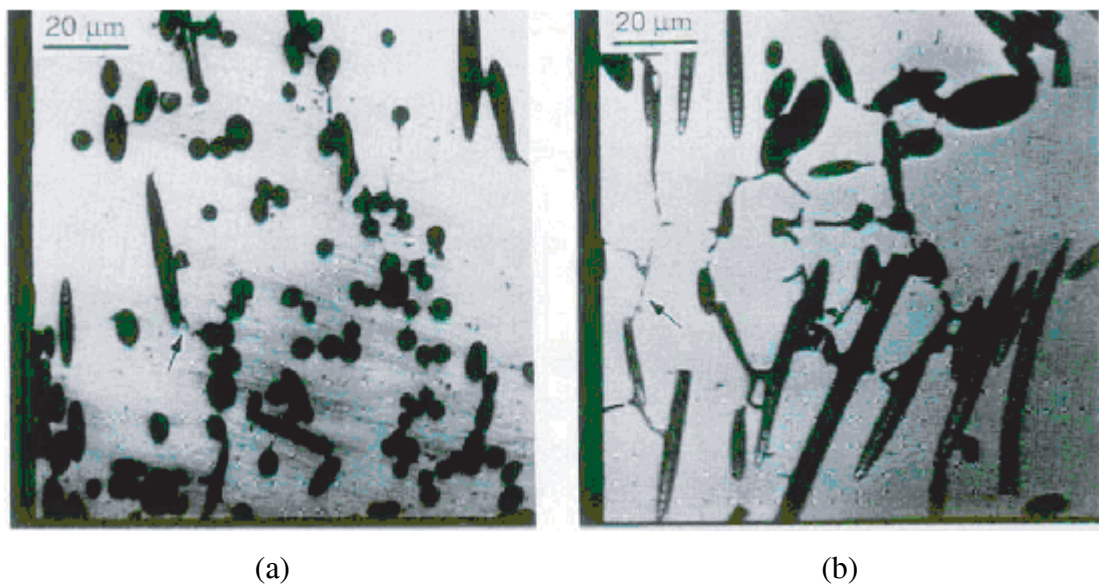


Fig. 1.8: AlCu-20%Saffil microstructure in the as quenched state (a) and after mechanical cycling in the internal friction pendulum (Parrini 1995).

#### ***1.4.1 Work with magnesium matrix composites***

Pure magnesium has a very high damping capacity (Reihani 81) which is due to the vibration of dislocation loops (Sugimoto 1977), but its mechanical strength is low (Mayencourt 1997). Magnesium can be hardened by adding a second phase precipitates, which can pin the dislocations and block the plastic deformation. This will increase the yield strength but the large damping capacity will be lost. Thus if magnesium matrix is engineered with reinforcements such as high strength fibers, which keeps the dislocation loops free to vibrate, a good high damping composite can be fabricated. Since few years, the study of composite with magnesium matrix has increased significantly (Wren 1995, Schäff 1999, Xianong 1997, Ashbee 1993, Luo 1995, Levitt 1972, Kiehn 1997). In this context, molten magnesium was pressurelessly infiltrated into TiC performs (56 vol.%) under flowing Ar at temperatures of

850, 900 and 950°C, where the mechanical strength of the composites was increased from 172 to 233 MPa for processing temperatures of 850 and 900°C (Contreras 2004).

The mechanical properties in the temperature range of 25 to 300°C of a Mg-10(vol.%)Ti composites were studied by tensile and jump strain rate tests (Pérez 2004). The composite was processed by powder metallurgy route by mixing pure titanium and magnesium powders followed by hot extrusion. Although the magnesium matrix shows a relatively large grain size, the composite shows a high strength (160 MPa), with a high elongation at room temperature (8%), higher than most of ceramic reinforced magnesium composites. The stress exponent calculated in the 100-300°C temperature range indicates that the deformation is dominated by dislocation slip. Titanium particle strengthen the matrix by load transfer that is manifested by fracture of titanium particles. The good mechanical properties were due to a sound microstructure of the Mg-10(vol.%)Ti composite obtained by powder mixing and extrusion at 400°C. Neither phases resulting from reaction between titanium reinforcement and magnesium matrix nor cavities were found at the Mg/Ti interfaces.

Magnesium based composites reinforced respectively with four types of particulates at different volume fraction were synthesized through a powder metallurgy route (Lu 2004). All reinforcement particles were observed to be homogenously distributed in their matrix. Structural characterization demonstrates almost no interfacial reaction between reinforcements and Mg matrix except for SiC reinforced composites. Mechanical properties show that the incorporation of TiB<sub>2</sub> particulates leads to a reduction of the yield stress of the composites, while use of ZrB<sub>2</sub> and SiC reinforcements enhances mechanical properties. TiC shows less effect on the yield stress of the composite. The strength of the four composites increases with increasing the volume fraction of particulates at the initial stage while decreases at high volume fraction. The optimal volume fraction was found to be about 8%.

As it concerns the thermal behavior, MMCs were tested under thermal cycling conditions, which are the most severe environmental conditions for composites. Hysteresis and residual strains as exhibited by thermal cycling curves of QE22 (Mg-2%Ag) based Mg alloy reinforced with Maftech, Saffil or Supertech short fibers were analyzed (Kumar 2004). It was found that the real permanent dimensional change in the material is imparted by plastic deformation of the matrix above 250-260°C in the longitudinal direction and by release of residual compressive strain arising from the squeeze casting process above 195-205°C in the



transverse direction. No microstructural change was observed on thermal cycling of metal matrix composites.

Fiber/matrix interfacial chemistry is a fundamental point, which has been studied in alumina fiber (Saffil) reinforced Mg and MgLi matrix composites by means of SEM, XPS, AES and XRD. It was concluded that lithium is a dominant reaction agent while the role of magnesium is marginal (Kúdela 2004). The reaction pathway of lithium includes (i) formation of  $\text{Li}_2\text{O}$  by the displacement redox reaction and (ii) formation of spinel-like phase  $\delta$  (Li) in the reaction couple  $\text{Li}_2\text{O}/\delta - \text{Al}_2\text{O}_3$  via topotactic insertion of  $\text{Li}^+$  into  $\delta - \text{Al}_2\text{O}_3$  lattice (presumably by the ion exchange). This reaction sequence contributes to the reactive wetting thus promoting fiber/matrix interfacial strength in MgLi composites.

An investigation reported the effect of the addition of hard ceramic particles on the mechanical properties at high temperature of pure magnesium (Gracés 2007). Because of the rapid loss of strength above room temperature and poor creep resistance at elevated temperature, magnesium alloys are rarely used above  $200^\circ\text{C}$ . The addition of ceramic particles into magnesium alloys improves the creep resistance at high temperature and also leads to an increase in tensile strength, Young's modulus and wear resistance. During extrusion process magnesium alloys develop a strong fiber texture with the basal plane parallel to the extrusion direction. This texture results in an additional reinforcement effect when the stress axis is parallel to the basal plane because of the inhibition of the basal slip system. It is shown that the reinforcement effect due to texture is effective up to  $300^\circ\text{C}$ . Under this temperature the extruded magnesium exhibits higher flow stress compared with composite. Above  $300^\circ\text{C}$ , the flow stress of the composite is higher than in the unreinforced magnesium.

The damping behavior of magnesium matrix composites reinforced with Cu-coated and uncoated SiC particulates fabricated by a powder metallurgy and hot extrusion process was investigated (Gu 2005). The results showed that, pure Mg excels the composite in the damping capacity at low temperature. When temperature increases to about  $75^\circ\text{C}$ , the damping of the composite with uncoated particles will exceed that of pure Mg; a further increase of  $250^\circ\text{C}$  will also cause a superior damping for the coated composite to that of pure Mg.

Another work investigated the in situ synthesis method and damping characterization of magnesium matrix composites reinforced with 8 wt% TiC using a remelting and dilution technique (Xiuqing 2007). The results revealed that damping capacity of materials is independent of frequency, but dependent on strain and temperature. Two damping peaks were observed at temperature 130°C and 240°C. The first peak is due to dislocation motion and the second one is due to interface and grain boundary sliding.

The internal thermal stresses and the related structural changes and matrix plastic deformation induced in magnesium based AZ91-saffil composites were monitored by acoustic emission (AE) and dilatometry (Chmelík 2002). The results are plotted in fig. 1.9, which demonstrates that there is no residual strain up to a temperature of 200°C, between 220 and 280°C there is a residual elongation, and for temperatures above 280°C there is a residual contraction that increases in magnitude with increasing values of  $T_{top}$ . The AE response also depends critically on the value of  $T_{top}$ . It increases significantly above a temperature of 320°C with intense AE bursts appearing above 360°C.

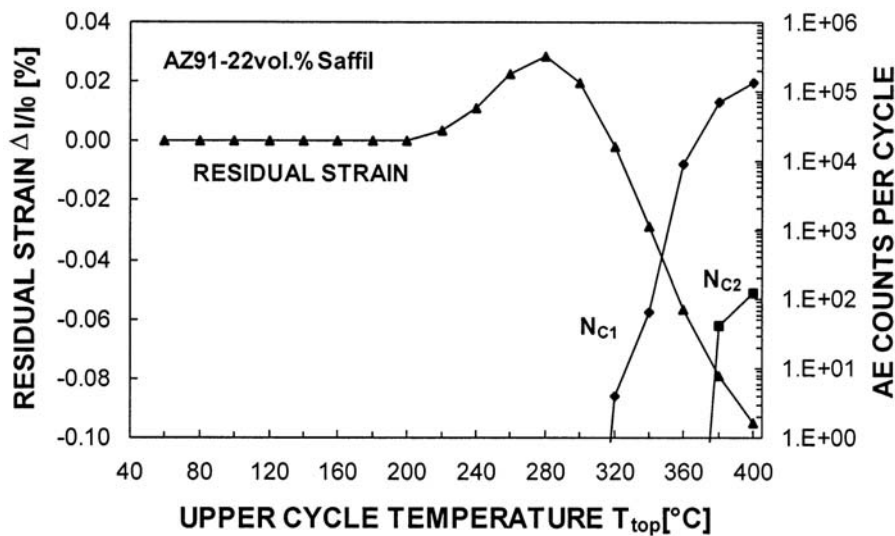


Fig.1.9: Residual strain,  $\Delta l/l_0$ , and AE counts for two different detection levels,  $N_{C1}$  and  $N_{C2}$  vs. the upper cycling temperature,  $T_{top}$ : the residual strain was estimated with reference to a temperature of 30°C and the AE counts were evaluated for the entire cooling period of each cycle (Chmelík 2002).

A model has been developed for the thermal stress relaxation due to the motion of existing dislocations (Mayencourt 1998). The model allows one to distinguish between the case where the dislocation motion is controlled by a viscous force such as dragging of solute atoms, and the case where the motion is controlled by a solid friction mechanism such as the breakaway from pinning points. In the case of magnesium based composites, the model indicates that the

dominant mechanism of thermal stress relaxation is the motion of existing dislocations, which is controlled by a solid friction mechanism.

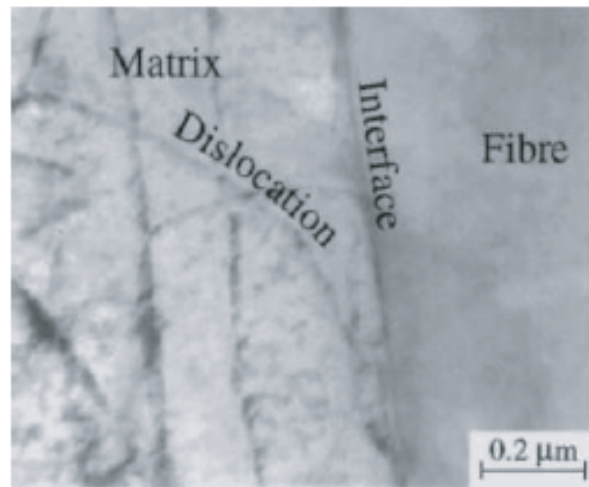


Fig. 1.10: TEM micrograph of an interface between fiber and matrix. One observes a large curvature of dislocations at the interface (Mayencourt 1998).

Mechanical spectroscopy was used in order to investigate the effect of the fiber orientation on the transient damping in magnesium and aluminum based metal matrix composites processed by gas pressure infiltration (Couteau 2004). The orientation of the fiber with respect to the matrix changes the coupling between the applied stress and the thermal stress, which in turns dominates the magnitude of the damping.

## 1.5 Aim of the research

As shown in the literature review, the mechanical properties of the composites depend on numerous parameters, such as the intrinsic properties of the constituting elements, the contact between the matrix and the reinforcement, the geometry of the interface of the constituent. However, it is known that these parameters are very important but their influence has not been completely understood. The results shown in the literature survey underline the importance of the interface properties on the composite behavior. However, most of the characterization techniques are dealing with microscopic properties, but few works present a link between the global behavior and the local mechanism of interface stress relaxation. The thermal and the mechanical stress can be relaxed by different mechanisms such as the breaking of the fiber, debonding at the interface and/or by the plastic deformation. The final

mechanical properties of the composite depend on these relaxation mechanisms. In the presence research, we want to use mechanical spectroscopy to further study the mechanisms of interface stress relaxation in order to better understand the behavior of MMCs like creep resistance, toughness or fatigue.

The objective of this work is to develop a material with a high damping capacity and good mechanical properties, by a combination of magnesium matrix reinforced by fibers of high modulus fabricated by gas pressure infiltration method. In order to exploit the model of interface stress relaxation by dislocation motion quantitatively, the metallic matrix will be oriented with respect to the interface from the crystallographic viewpoint.

The experimental results will be interpreted by a theoretical model, in order to quantify the coefficient of stress transfer across the interface. The interpretation of the mechanical loss spectra by the model, which predicts the evolution of mobile dislocation density and interfacial strength with respect to temperature, will be very useful to compare the damping, toughness and creep resistance of different composites.

The comparison of the global and local properties of the composites and the thermal and mechanical stress relaxation model allows a better understanding of the influence of the quality of the interface on the microscopic properties and the influence of the relaxation mechanism on fatigue.

## Chapter 2: Mechanical Spectroscopy

### 2.1 Anelasticity

When a stress lower than the yield stress of the specimen is applied, the response of the material is characterized by a deformation completely recoverable upon release of the applied stress and is composed of an anelastic part and an elastic part (Nowick 1972). The elastic part is linearly proportional to the applied stress and instantaneous, while the anelastic part depends on time i.e. the equilibrium response is achieved after sufficient time and its magnitude is much lower than the elastic part.

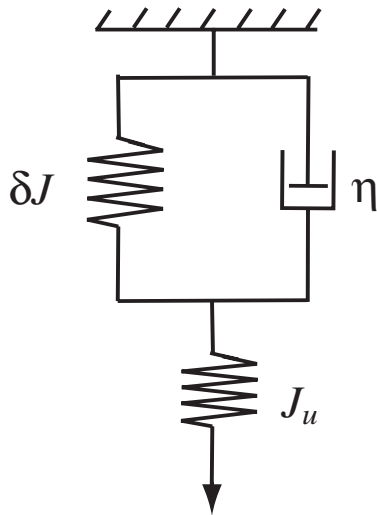


Fig. 2.1a: Schematic diagram of the rheological model of standard anelastic solid.

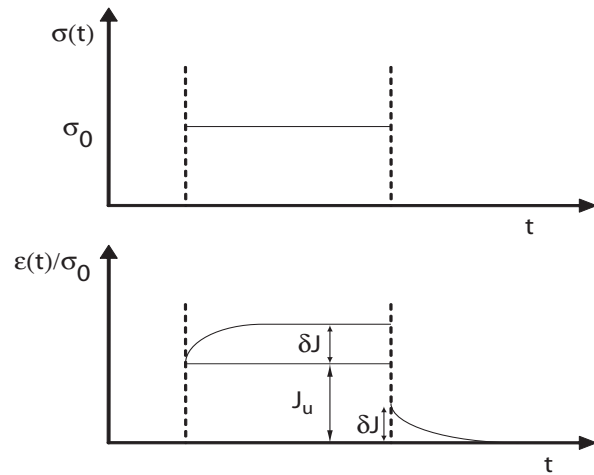


Fig. 2.1b: Stress and normalized strain response in an anelastic solid as a function of time.

The anelastic behavior can be described conveniently by using a rheological model for a standard anelastic solid as shown in fig. 2.1a. The elastic part of the response  $\varepsilon_{el}$  is controlled by the elastic spring with compliance  $J_u$  and the anelastic part of the response  $\varepsilon_{anel}$  is controlled by a spring with compliance  $\delta J$  and a dashpot with a coefficient of viscosity  $\eta = \frac{\tau}{\delta J}$ , where  $\tau$  is the relaxation time. Following the rheological model, the total strain can be calculated by

$$\varepsilon(t) = \varepsilon_{el} + \varepsilon_{anel}(t) \quad (2.1)$$

a general stress strain equation describing the anelastic behavior can be written as

$$J_r \sigma + J_u \tau \dot{\sigma} = \varepsilon + \tau \dot{\varepsilon} \quad (2.2)$$

If the applied stress is periodic and has the form

$$\sigma = \sigma_0 \exp(i\omega t) \quad (2.3)$$

for the conservation of linearity of the stress-strain relation, the anelastic strain is also periodic and is expressed as

$$\varepsilon = \varepsilon_0 \exp(i\omega t - \phi) \quad (2.4)$$

where  $\varepsilon_0$  is the strain amplitude and  $\phi$  is the angle by which strain lags behind the stress. This angle  $\phi$  is often called the loss angle. For ideal elasticity  $\phi = 0$  and the corresponding strain will be

$$\varepsilon = \varepsilon_{el} = J \cdot \sigma \quad (2.5)$$

where

$$J = J_1 - iJ_2 \quad (2.6)$$

$J_1$  is the real part of the compliance  $J$  and is called the storage compliance.  $J_2$  is the imaginary part of the compliance  $J$  and is called the loss compliance. The energy  $\Delta W$  dissipated in a full cycle per unit volume is obtained by

$$\Delta W = \oint \sigma d\varepsilon = \pi J_2 \sigma_0^2 \quad (2.7)$$

and the maximum stored energy  $W$  per unit volume is

$$W = \int_0^{\pi/2} \sigma \cdot d\varepsilon = \frac{1}{2} J_1 \sigma_0^2 \quad (2.8)$$

The specific damping capacity is the ratio of the energy dissipated to the maximum stored elastic energy per unit volume and is expressed as

$$\frac{\Delta W}{W} = 2\pi \left( \frac{J_2}{J_1} \right) = 2\pi \tan \phi \quad (2.9)$$

which gives

$$\tan \phi = \frac{1}{2\pi} \frac{\Delta W}{W} \quad (2.10)$$

As  $\tan \phi$  gives a measure of the fractional energy loss per cycle due to anelastic behavior, the quantity  $\tan \phi$  is commonly known as internal friction or the mechanical loss of the material. The internal friction is directly related to the number and the kind of mobile micro structural units inside the solid as well as to the characteristic motion they undergo. Therefore, the measurement of the internal friction can be used to obtain information about the microstructure of the material. Since the deformation is anelastic, the method is non destructive. Mechanical spectroscopy consists in applying a mechanical oscillating stress of frequency  $\omega$  to a solid sample. The response of the solid involves the absorption of mechanical energy that one measures as a function of frequency or temperature, giving an internal friction spectrum.

In the usual case where  $\delta J \equiv J_r - J_u \ll J_r$  is assumed to hold, the introduction of eqs. (2.3) and (2.4) into (2.2) leads to a mechanical loss peak together with the variation of compliance, which are of the following form:

$$\tan \phi(\omega) = \Delta \frac{\omega \tau}{1 + \omega^2 \tau^2} \quad (2.11)$$

$$\frac{\delta J}{J_u}(\omega) = \Delta \frac{1}{1 + \omega^2 \tau^2} \quad (2.12)$$

with

$$\Delta \equiv \frac{\delta J}{J_u} \quad (2.13)$$

where  $\Delta$  is the relaxation strength. Eqs. 2.11 and 2.12 are referred to as Debye equations. When equation 2.11 is plotted as a function of  $\log \omega\tau$ , the mechanical loss  $\tan \phi$  has a peak symmetrical around  $\omega\tau = 1$  (Debye peak). The height of the peak is  $\frac{\Delta}{2}$ , where  $\Delta$  is the relaxation strength.

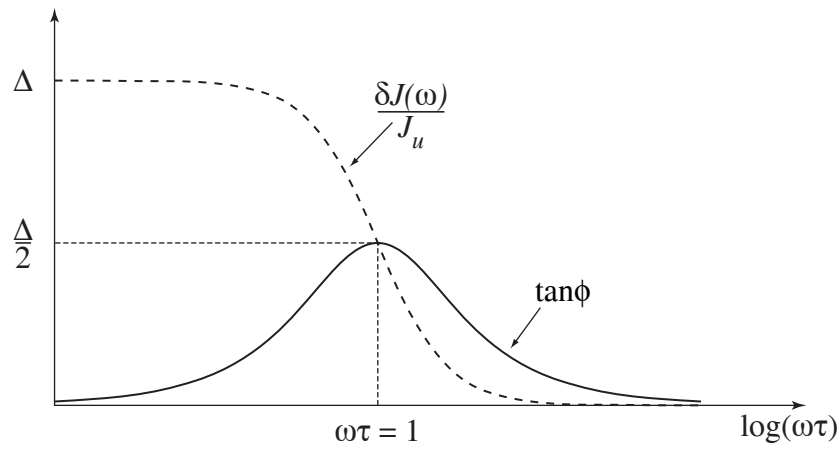


Fig.2.2: Mechanical loss  $\tan \phi$  and the relative variation of the compliance  $\frac{\delta J}{J_u}(\omega)$  as a function of  $\log \omega\tau$ .

## 2.2 Thermal activation

Most of the relaxation mechanisms are thermally activated. The successful transition rate of an atom from one position of local minimum to the neighboring local minimum is calculated by the following statistical rate

$$\nu = \nu_0 \exp\left(-\frac{\Delta G_{act}}{kT}\right) \quad (2.14)$$



where  $\nu$  and  $\nu_0$  is the attempt frequency and the limit attempt frequency respectively.  $\Delta G_{act}$  is the free activation energy of system. From eq. 2.15 one can obtain the Arrhenius equation

$$\tau = \tau_0 \exp\left(\frac{\Delta G_{act}}{kT}\right) \quad (2.15)$$

with  $\nu = \tau^{-1}$  and  $\nu_0 = \tau_0^{-1}$ , where  $\tau$  and  $\tau_0$  are the relaxation and the limit relaxation time respectively.

## 2.3 Measurement of internal friction/mechanical loss in a pendulum

Since the magnitude of the anelastic deformation is very low, it is impossible to detect the deformation by a tensile test. A technique is required with more sensitivity to deformation. For this reason, dynamic methods are usually used (Schaller 2001). In a torsion pendulum the specimen is the elastic component of the pendulum.

If there is no dissipation of energy, the equation of motion can be written as (Rao 1990)

$$I\ddot{\theta} + C\theta = \sigma_{ext} \quad (2.16)$$

This is the equation of motion of a harmonic oscillator, where  $\theta$  is the torsion angle of the specimen,  $I$  is the moment of inertia of the oscillator,  $C$  is the restoring coefficient and  $\sigma_{ext}$  is the applied external stress. If dissipation of energy occurs then eq. 2.16 becomes

$$I\ddot{\theta} + C(1 + i \tan \phi)\theta = \sigma_{ext} \quad (2.17)$$

Experimentally  $\tan \phi$  can be determined by two methods: in case of a free oscillation ( $\sigma_{ext} = 0$ ), it can be calculated by the logarithmic decrement and in case of a forced pendulum ( $\sigma_{ext} = \sigma_0 \exp(i\omega t)$ ),  $\tan \phi$  can be measured directly.

### 2.3.1 Free pendulum: (resonant system)

In case of free oscillation, the oscillator is excited by a pulse and then it oscillates around its equilibrium position. The eq. 2.18 can be written as

$$I\ddot{\theta} + C(1 + i \tan \phi)\theta = 0 \quad (2.18)$$

The general solution of eq. 2.18 is

$$\theta(t) = \theta_0 \exp\left(\frac{-\omega_0 \tan \phi}{2}\right) \exp(i\omega_0 t) \quad (2.19)$$

In case of very low damping, for instance smaller than 0.1 (Zener 1947, Parke 1966)  $\tan \phi$  can be calculated by the logarithmic decrement, representing the natural logarithm of the ratio of the amplitudes of two successive vibrations.

$$\tan \phi = \frac{1}{n\pi} \ln\left(\frac{\theta_i}{\theta_{i+n}}\right) \quad (2.20)$$

where  $\theta_i$  and  $\theta_{i+n}$  are the amplitudes of the  $i^{th}$  and  $(i+n)^{th}$  oscillations, respectively.

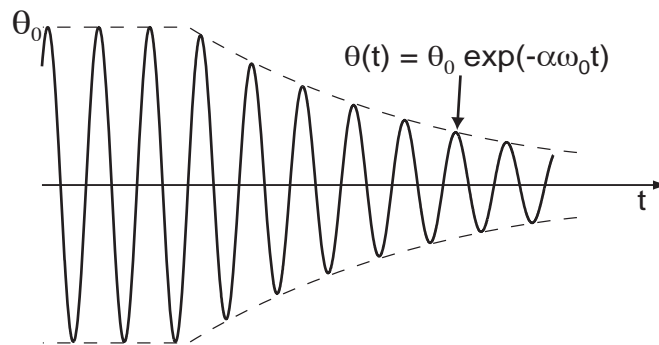


Fig. 2.3: The free decay of natural vibrations at resonant frequency with a logarithmic decrement  $\alpha$ .

### 2.3.2 Forced oscillations: (sub resonant mode)

If the applied oscillation is cyclic of the form  $\sigma_0 \exp(i\omega t)$ , then eq. 2.17 can be re written as

$$I\ddot{\theta} + C(1 + i \tan \phi)\theta = \sigma_0 \exp(i\omega t) \quad (2.21)$$

Which has a solution of the form

$$\theta(t) = \theta_0 \exp(i(\omega t - \phi)) \quad (2.22)$$

where  $\phi$  is the phase lag between the applied stress and the corresponding strain of the sample. From eqs. (2.21) and (2.22) it is possible to obtain

$$\tan \phi = \frac{\omega_r^2}{\omega_r^2 - \omega^2} \tan \phi \quad (2.23)$$

When  $\omega \ll \omega_r$ , one can write

$$\tan \phi \approx \tan \phi \quad (2.24)$$

Thus the mechanical loss can be measured directly from the phase lag for a sub resonant system.

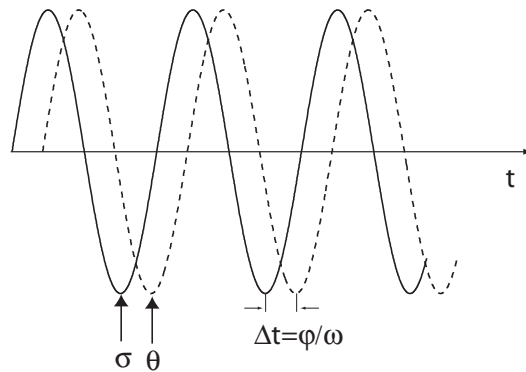


Fig. 2.4: Stress and strain as a function of time in case of forced oscillations. The mechanical loss can be calculated from the phase lag  $\phi$ .

## 2.4 Relaxation phenomenon in metal matrix composites

Mechanical spectroscopy has proved to be an efficient non destructive method to investigate interfaces in MMCs (Parrini 1995). The relaxation of the thermal stresses contributes an additional component, which is superimposed to the isothermal intrinsic damping  $\tan \phi_{in}$  of the composites.

$$\tan \phi = \tan \phi_{in} + \tan \phi_{Tr} \quad (2.25)$$

$\tan \phi_{Tr}$  is the transient damping due to the relaxation of thermal stresses accumulated at the interface. The thermal stress can be relaxed either by crack propagation, which leads to damage accumulation at the interface and results in a degradation of the mechanical properties of the composites or by the motion of dislocations, which conserves the good mechanical properties. Different models exist for the relaxation of thermal stresses by the motion of dislocations.

### 2.4.1 Relaxation due to the dragging of solute atoms by dislocations

When thermal stresses are relaxed by the movement of dislocations dragging solute atoms, the rheological model shown in fig. 2.1a can be exploited. Fig. 2.5 shows the schematic diagram of the forces acting on a single dislocation segment of length  $L$ .

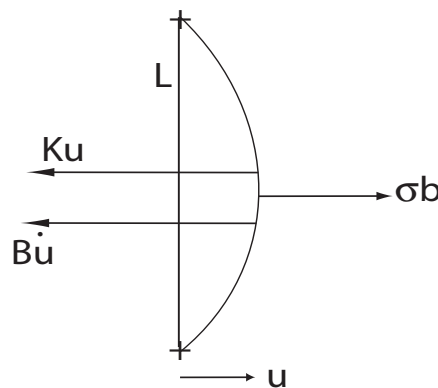


Fig. 2.5: Schematic diagram of the forces acting on a dislocation segment of length  $L$ .

Under the effect of an external stress  $\sigma$ , a dislocation segment will bow between its pinning points. If the dislocation motion is controlled by a viscous friction type mechanism due to the interaction with point defects, the equation of motion can be written as

$$B\dot{u} + Ku = \sigma b \quad (2.26)$$

$\sigma b$  is the Peach and Koehler force with  $b$  as the Burger's vector,  $Ku$  is the restoring force of the dislocation with  $K$  as the restoring coefficient and  $B\dot{u}$  is the dragging force with  $B$  as the dragging coefficient.  $u$  is the mean displacement of the dislocation segment under the applied stress  $\sigma$ . From eq. 2.26 the mechanical loss can be calculated as

$$\tan \phi = \Delta \frac{\omega \tau}{1 + (\omega \tau)^2} \quad (2.27)$$

Where

$$\Delta = \frac{\Lambda b^2}{J_{el} K} \text{ and } \tau = \frac{b}{K} \quad (2.28)$$

$\Delta$  and  $\tau$  are the relaxation strength and the relaxation time, respectively (Schaller 2001).

### ***2.4.2 Relaxation due to hysteretic damping and Granato-Lücke model***

If the pinning point defects separated by an average distance  $\bar{l}$  are immobile and segregated on the dislocation segment of average length  $\bar{L}$  between the hard pinning points (fig. 2.6), then under a stress  $\sigma_0 > \sigma_{0cr}$ , the dislocation segments can break away from the line of segregated point defects.

The critical stress amplitude  $\sigma_{0cr}$  is related to the critical force  $f_{0cr}$  required for depinning and to the Burger's vector  $b$ .

$$\sigma_{0cr} = \frac{f_{0cr}}{b\bar{l}} \quad (2.29)$$

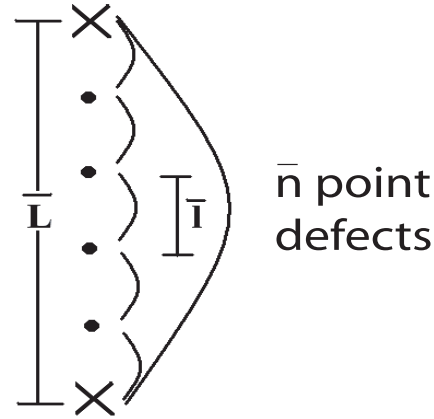


Fig. 2.6: Schematic representation of the breakaway mechanism of a dislocation segments from immobile point defects.

The relaxation phenomenon can be well explained by the following rheological model in fig. 2.7.

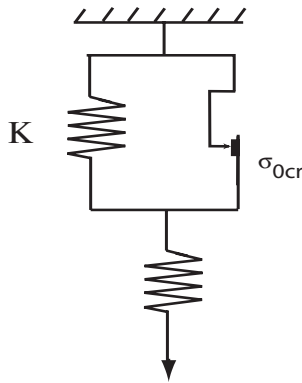


Fig. 2.7a: The rheological model for the localized solid friction device.

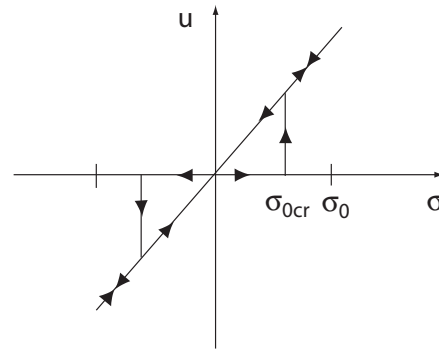


Fig. 2.7b: Dislocation mean displacement as a function of stress amplitude.

The anelastic response of this solid friction model shows a hysteresis between loading and unloading. When the magnitude of the applied stress reaches the critical stress  $\sigma_0 = \sigma_{0cr}$ , the dislocation segment breakaway from the pinning points and shows a sudden increase of displacement  $u$ . The anelastic strain can be calculated as

$$\varepsilon_{an} = \Lambda b \bar{u} = \frac{\Lambda b^2 \bar{L}^2}{12\gamma} \sigma \quad (2.30)$$

$\Lambda$  is the dislocation density and  $\gamma$  is the line tension of the dislocation segment. Finally, one obtains the mechanical loss

$$\tan \phi = \begin{cases} 0 & (\sigma_0 < \sigma_{0cr}) \\ \Delta \frac{1}{\pi} \left( \frac{\sigma_{0cr}}{\sigma_0} \right)^2 & (\sigma_0 > \sigma_{0cr}) \end{cases} \quad (2.31)$$

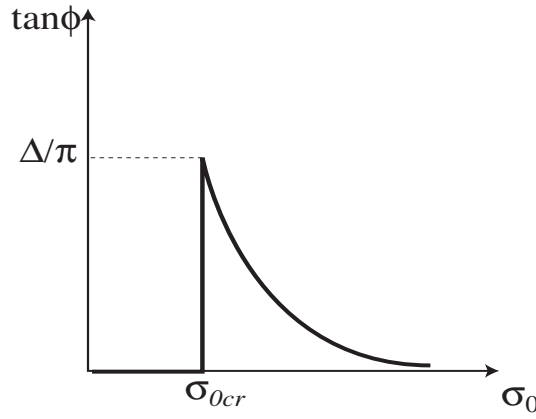


Fig. 2.8: Mechanical loss spectrum as a function of  $\sigma_0$  (eq.2.31).

If the number of point defects  $n$  segregated on the dislocation segment of length  $\bar{L}$  follows a statistical exponential distribution (Granato 1956), one can calculate the mechanical loss, which is represented in fig. 2.9.

$$\tan \phi = \Delta \frac{1}{\pi} \left( \frac{\sigma_{0cr}}{\sigma_0} \right) \exp \left( - \frac{\sigma_{0cr}}{\sigma_0} \right) \quad (2.32)$$

and the average critical stress has the form

$$\sigma_{0cr} = \frac{\bar{n} f_{0cr}}{bL} = \frac{f_{0cr}}{bl} \quad (2.33)$$

For purely random segregation of point defects, eq. 2.32 can be rewritten as

$$\ln(\tan \phi \cdot \sigma_0) = K - \frac{\sigma_{0cr}}{\sigma_0} \quad (2.34)$$

The plot of  $\ln(\sigma_0 \cdot \tan \phi)$  as a function of  $1/\sigma_0$  gives a straight line and from the slope one can calculate the critical stress for breakaway. Such a plot is called a Granato-Lücke plot (fig.2.9b) (Gremaud 1987).

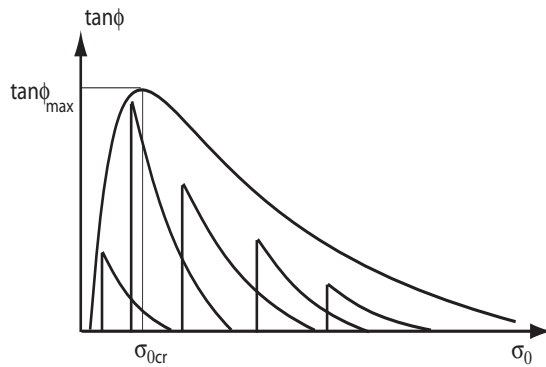


Fig. 2.9a: Schematic illustration of the mechanical loss as a function of  $\sigma_0$ , when the point defects segregated along the dislocation line follow a statistical distribution.

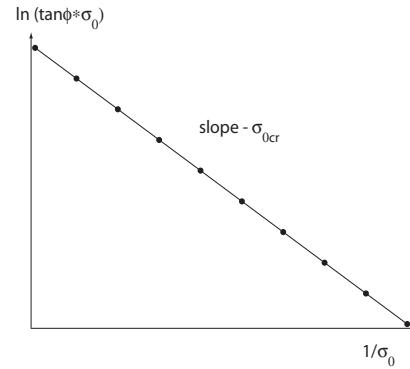


Fig. 2.9b: The Granato-Lücke plot.

### 2.4.3 Crack propagation and thermal fatigue

Thermal stresses can be relaxed either by interface debonding or by crack propagation, which leads to degradation of the mechanical properties of the composites. They are also relaxed by the creation and motion of dislocations, which instead preserves the interfacial bonding. Mechanical or thermal stresses can generate fatigue in MMCs. Parrini and Schaller (Parrini 1995) have observed such a phenomenon in an Al-based composite reinforced with  $\text{Al}_2\text{O}_3$  (SAFFIL). Mechanical spectroscopy measurements reveal a sharp peak as a function of stress amplitude. This peak is very similar to the amplitude dependent damping behavior of the localized solid friction device (fig. 2.7). The authors identified the matrix-reinforcement debonding as the relaxation mechanism.

Thermal stress relaxation by the motion of dislocation adds a transient additional response to the mechanical loss spectra. This response depends on the change of the temperature rate and on the frequency of oscillation. The anelastic response due to the motion of dislocation has been found to be proportional to the rate of change of temperature  $\dot{T}$  and to the difference of thermal expansion coefficient between the matrix and the fiber  $\Delta\alpha$ .



$$\dot{\epsilon} \sim \Delta\alpha\dot{T} \quad (2.35)$$

The mechanical loss  $\tan\phi$  is proportional to  $\dot{T}/\omega$ . This reflects the results obtained in the aluminum matrix-composites (Carenno-Morelli 1999).

## 2.5 Model of Mayencourt and Schaller

Mayencourt and Schaller have developed a model based on the motion of existing dislocations pushed away from the fiber-matrix interface (Mayencourt 1998). The model is developed for two different cases based on the mechanism that controls the dislocation motion. In the first case, the dislocation motion is controlled by a viscous force such as dragging of solute atoms. In the second case, the dislocation motion is assumed to be controlled by a hysteretic solid friction mechanism.

Due to the mismatch of thermal expansion coefficient between the matrix ( $\alpha_m$ ) and the fiber ( $\alpha_f$ ), thermal stresses ( $\sigma_{th}$ ) arise at the matrix-fiber interface. During the measurements, a cyclic mechanical stress ( $\sigma_m$ ) is added to these thermal stresses. Because of the motion of dislocation a part of the stress is relaxed ( $\sigma_R$ ).

$$\sigma_{th} = CE\Delta\alpha\dot{T}t \quad (2.36)$$

$$\sigma_m = \sigma_0 \sin \omega t \quad (2.37)$$

$$b\sigma_R = Ku(t) \quad (2.38)$$

here  $b$  is the Burger's vector,  $K$  is a restoring coefficient,  $C$  is a geometrical structure factor that takes into account the stress profile at the interface and the concentration of the fibers,  $\Delta\alpha$  is the difference of thermal expansion coefficient between the matrix and the fiber and  $\sigma_0$  is the maximum stress amplitude.  $\dot{T}$  is the heating or cooling rate,  $\omega$  is the excitation frequency, and  $u$  is the dislocation mean displacement. The mechanical loss is expressed as:

$$\tan\phi = \frac{1}{2\pi} \frac{W_{diss}}{W_{el}} = \frac{1}{\pi J_{el} \sigma_0^2} \oint \sigma_m \cdot d\epsilon_{an} \quad (2.39)$$

$J_{el}$  is the elastic compliance of the composite and  $d\varepsilon_{an}$  is the anelastic strain during one cycle of vibration. Due to the relaxation of thermal stresses, a transient damping  $\tan\phi_{Tr}$ , which depends on the temperature variation rate  $\dot{T}$  and the excitation frequency  $\omega$ , is superimposed on the isothermal equilibrium damping. It does not correspond to a micro-structural modification. The transient mechanical loss due to change of temperature can be extracted separately from the intrinsic damping and the above equation can be rewritten as

$$\tan\phi_{Tr} = \frac{1}{2\pi J_{el} \sigma_0^2} \int_0^{\pi/\omega} \sigma_m d\varepsilon_{Tr} \quad (2.40)$$

The dislocations move only during the half cycle where the applied and the thermal stresses are in the same direction.  $d\varepsilon_{Tr}$  is the additional deformation due to the transient damping.

### 2.5.1 Viscous friction mechanism

If the dislocation motion is controlled by the dragging of solute atoms, the mechanism is of a viscous type. The rheological model for such a mechanism is shown in fig. 2.1a

The equation of motion of a dislocation is given by

$$\sigma bl = F_{\text{friction}} + F_{\text{restoring}} \quad (2.41)$$

where  $\sigma bl$  is the Peach and Koehler force acting on a dislocation segment of length  $l$ ,  $F_{\text{restoring}}$  is the restoring force, which is generally associated with the line tension  $\gamma$  of pinned dislocation segments of length  $l$ . Per unit length of dislocation this force is given by

$$F_{\text{restoring}} = K\bar{u} \quad \text{with} \quad K = \frac{12\gamma}{l^2}$$

Introducing the Orowan equation  $\varepsilon = \Lambda bu$  in eq. 2.27 one obtains the equation of motion of the dislocation segment

$$\frac{B}{K} \dot{\epsilon} + \epsilon = \frac{\Lambda b^2 C E \Delta \alpha \dot{T} t}{K} \quad (2.42)$$

Where  $\Lambda$  is the mobile dislocation density. By solving this first order differential equation, the transient mechanical loss can be calculated, which is of the form

$$\tan \phi_{tr} = \frac{\Lambda b^2 C E \Delta \alpha}{\pi J_u K} \frac{\dot{T}}{\omega \sigma_0} \left[ 1 - \frac{1 + \exp\left(-\frac{\pi}{\omega \tau}\right)}{2} \right] \left( 1 + \frac{\pi}{\omega \tau} \right) \left( \frac{\omega^2 \tau^2}{1 + \omega^2 \tau^2} \right) \quad (2.43)$$

Where  $\tau = \frac{B}{K}$  is the relaxation time. Eq. 2.43 shows a linear relationship between the transient mechanical loss and  $\frac{\dot{T}}{\sigma_0}$ . The dependence is more complex with  $\frac{1}{\omega}$ , where for a low value of  $\omega$ , the dependence is linear and for the higher value it is exponential.

Fig. 2.10 shows the behavior of the transient mechanical loss controlled by a viscous friction mechanism as a function of the inverse of the frequency of oscillations.

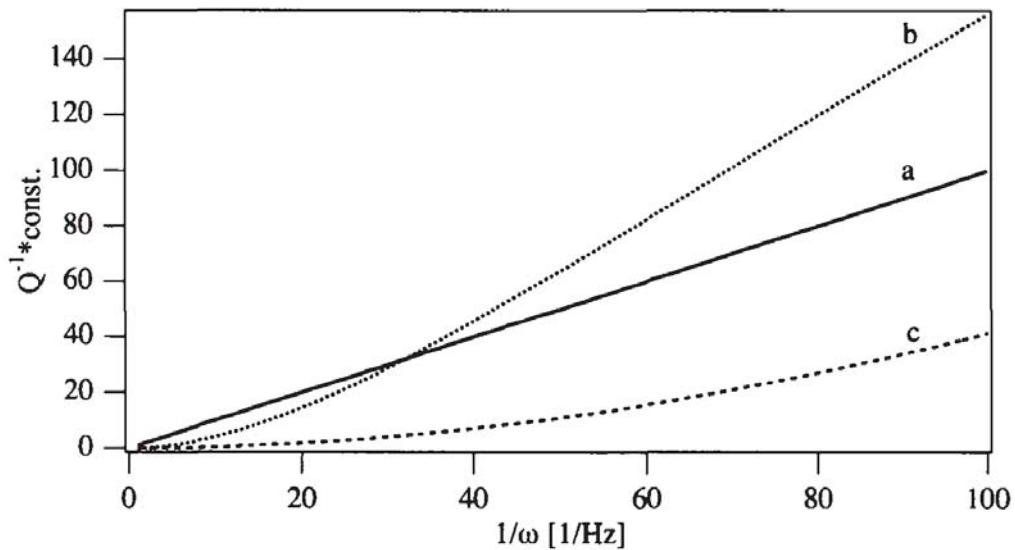


Fig: 2.10: Transient mechanical loss as a function of the inverse of the frequency in the case of viscous gliding of dislocations. Curves (a)-(c) are calculated with different values of  $B$ , i.e. either at different temperatures for a small activation energy or for different activation energies at a given temperature.  $B(a) < B(b) < B(c)$  (Mayencourt 1999).

### 2.5.2 Solid friction mechanism

The hysteretic damping observed in composites is due to a solid friction mechanism and the rheological model for such a mechanism is shown in fig. 2.7. The total stress acting on the dislocation segment is

$$\sigma_{\text{tot}} = \sigma_m + \sigma_{\text{th}} \quad (2.44)$$

where  $\sigma_{\text{tot}}$ ,  $\sigma_{\text{th}}$  and  $\sigma_m$  are the total stress, the thermal stress and the mechanical stress, respectively.

When the applied stress and the thermal stress are in the same direction, these stresses are coupled, which is intense enough to induce breakaway of dislocation segments from immobile point defects and the dislocation can glide. Thus, a dislocation can glide only during half cycle where the applied stress is in phase with the thermal stress. Due to the hysteretic motion, the dislocation will not move back when the total stress is lower than the critical stress. Therefore the dislocation stops. Thus, the dislocation motion takes place only between a part of the period, i.e. between  $t_1$  and  $t_2$  as shown in fig. 2.11.

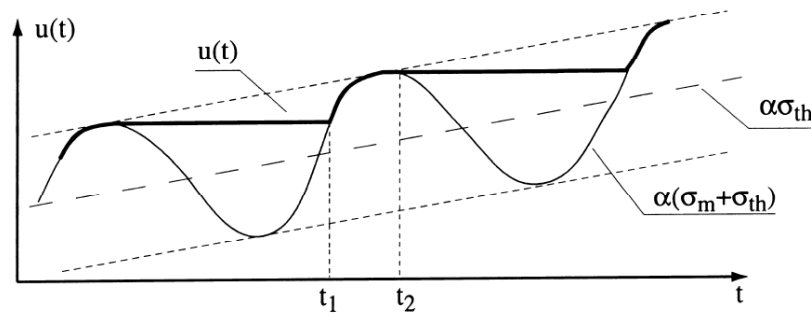


Fig: 2.11: Dislocation displacement as a function of time for the case of solid friction. A periodic stress is superimposed to an increasing thermal stress that is obtained by temperature scan. The dislocation can move only between  $t_1$  and  $t_2$  where the stress acting on the dislocation is higher than the critical stress necessary for the breakaway of the dislocation segment.

The mean displacement of the dislocation  $u$ , leads to a relaxation that balances exactly the thermal and the mechanical stresses

$$u = \frac{b}{K} (CE\Delta\alpha\dot{T}t + \sigma_0 \sin \omega t) \quad (2.45)$$

Applying the Orowan equation one obtains

$$\varepsilon = \frac{\Lambda b^2}{K} (CE\Delta\alpha\dot{T}t + \sigma_0 \sin \omega t) \quad (2.46)$$

Where  $\Lambda$  is the mobile dislocation density. The transient mechanical loss can be calculated as

$$\tan \phi_{Tr} = \frac{1}{\pi J_{el} \sigma_0^2} \oint \sigma d\varepsilon_{an}$$

This equation cannot be solved analytically. By taking as an approximation a triangular excitation instead of the sinusoidal one, one obtains a nonlinear relationship between the transient mechanical loss and  $\dot{T}/\omega$

$$\tan \phi_{Tr} = 2C_1 C_2 \frac{\dot{T}}{\omega} \frac{1 - \frac{\pi}{2} C_2 \frac{\dot{T}}{\omega}}{1 + \frac{\pi}{2} C_2 \frac{\dot{T}}{\omega}} \quad \text{for} \quad \frac{\dot{T}}{\omega} < \frac{2}{3\pi} \cdot \frac{1}{C_2} \quad (2.47)$$

With

$$C_1 = \frac{\Lambda b^2}{J_{el} K} \quad \text{and} \quad C_2 = \frac{CE\Delta\alpha}{\sigma_0} \quad (2.48)$$

Where  $C_1$  and  $C_2$  are fitting parameters. From eq. 2.48 it is observed that  $C_1$  is proportional to the mobile dislocation density  $\Lambda$  and the inverse of the relaxation compliance  $K$ , while  $C_2$  is proportional to the geometrical structure factor  $C$ .

For higher values of  $\dot{T}/\omega$  one obtains

$$\tan \phi_{Tr} = \frac{1}{4} C_1 \left( C_2 \frac{\dot{T}}{\omega} + \frac{2}{\pi} \right) \quad \text{for} \quad \frac{2}{3\pi} \cdot \frac{1}{C_2} < \frac{\dot{T}}{\omega} < \frac{2}{\pi} \frac{1}{C_2} \quad (2.49)$$

$$\tan \phi_{Tr} = \frac{1}{2} C_1 C_2 \frac{\dot{T}}{\omega} \quad \text{for} \quad \frac{2}{\pi} \frac{1}{C_2} < \frac{\dot{T}}{\omega} \quad (2.50)$$

Fig. 2.12 shows the behavior of the transient mechanical loss as a function of  $\frac{\dot{T}}{\omega\sigma_0}$ . It is

observed that the transient mechanical loss is nonlinear only for values  $\frac{\dot{T}}{\omega} < \frac{2}{3\pi} \cdot \frac{1}{C_2}$ .

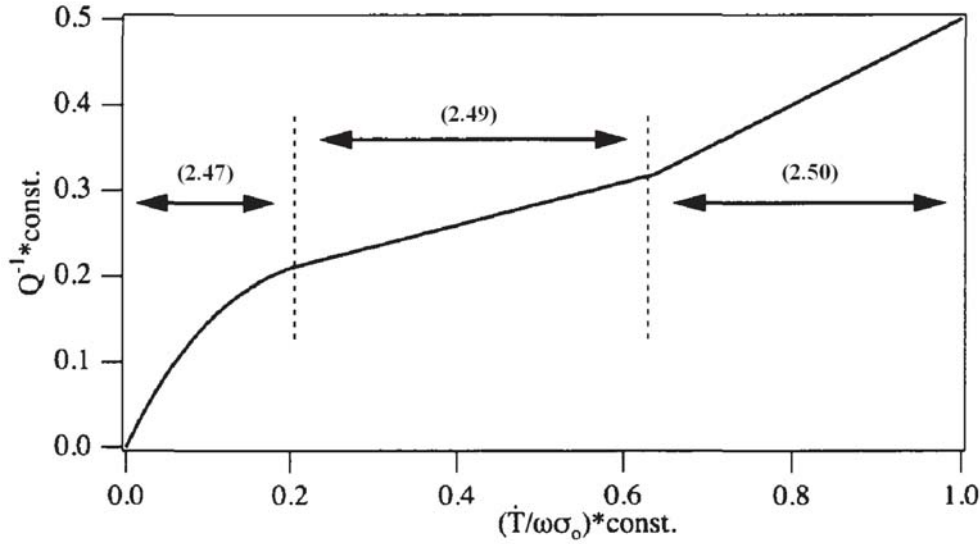


Fig. 2.12: Transient mechanical loss as a function of the inverse of  $\frac{\dot{T}}{\omega\sigma_0}$  for the case of solid friction of dislocations. The three parts of the curves correspond to eqs. 2.47-2.50 (Mayencourt 1999).

## 2.6 Mechanical spectroscopy with magnesium and its composites

The mechanical loss in pure magnesium is related to the interaction of the dislocations with the Peierls valleys. In high purity magnesium two sharp peaks were observed and are related to Bordoni relaxations. Between 40K and 240 K, a broad maximum has been observed at high frequency (40kHz) and at low amplitude ( $<10^{-7}$ ) due to the motion of dislocation in the basal plane (Fantozzi 1984, Reihani 1979, Reihani 1981).

In magnesium of commercial purity, the mechanical loss was mainly studied as a function of stress amplitude, which fits with the Granato-Lücke model (Trojanová 1998). The mechanical loss depends on the concentration of the impurity atoms (Trojanová 1997) and their solubility (Mayencourt 1999). The mechanical loss also depends on the grain size (Sugimoto 1977). A hysteresis between ascending and descending amplitude has been observed (El-Al 1998).

Mayencourt (Mayencourt 1999) and Couteau (Couteau 2004) have investigated the thermal stress relaxation in several magnesium matrix composites. They have observed a hysteretic damping behavior of the composite, where the transient mechanical loss is non-linearly related to the measurement parameter  $\dot{T}/\omega$ . Fig. 2.13 shows mechanical loss spectra of magnesium matrix composites with different reinforcements. The spectra show hysteresis between heating and cooling. Fig. 2.14 shows spectra for the mechanical loss as a function of  $\dot{T}/\omega$ . The solid curves are obtained by fitting the experimental points with a solid friction model according to eq. 2.43.

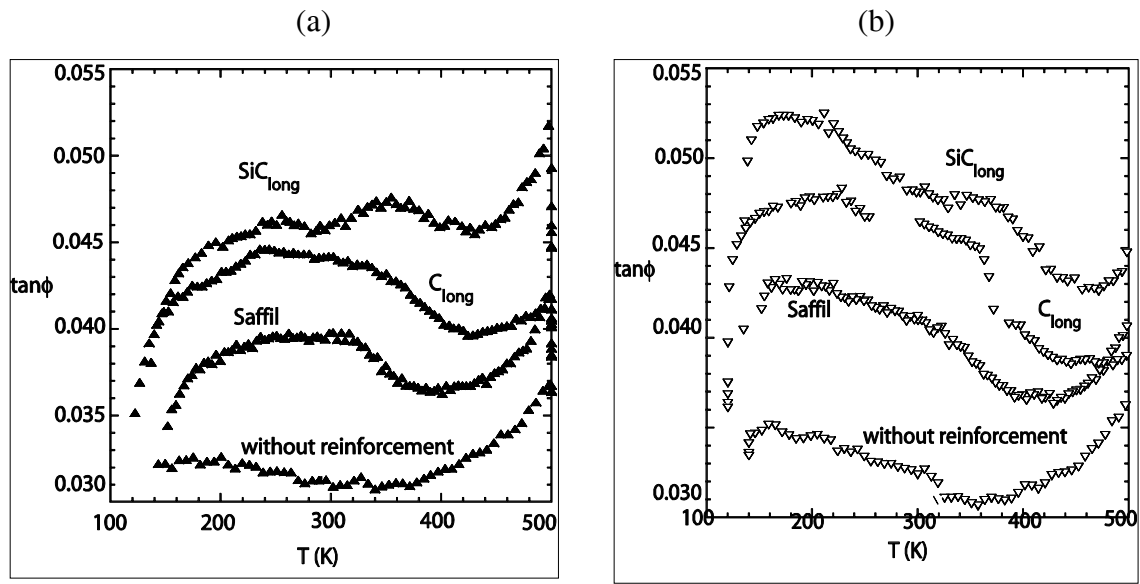


Fig. 2.13: Mechanical loss  $\tan\phi$  as a function of temperature for Mg-2%Si without reinforcement and reinforced with Saffil ( $\text{Al}_2\text{O}_3$ ), long SiC and C fibers (a) heating (b) cooling (Couteau 2004).

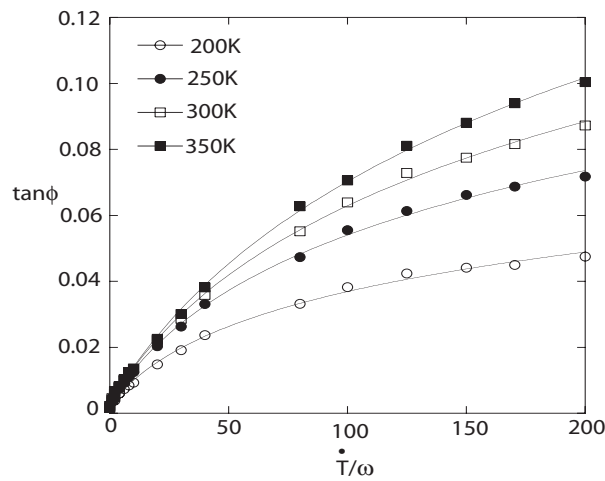


Fig. 2.14: Mechanical loss  $\tan\phi$  as a function of  $\dot{T}/\omega$  for Mg-2%Si reinforced long SiC fibers (Couteau 2004).

Mechanical spectroscopy has been proven to be a very efficient method to investigate the dynamics of the crystalline defects. It is very sensitive to the motion of dislocations, which is the main relaxation mechanism in the magnesium matrix composites. Moreover, the evolution of the elastic modulus as a function of temperature and frequency can be obtained. In the case of temperature cycling, such a measurement may be useful in monitoring fatigue and more generally the life time of the composite.



## **Chapter 3: Sample preparation and experimental techniques**

In this work pure magnesium (99.98 wt %) has been used as the metallic matrix and long carbon fibers, long stainless steel (AISI 304) fibers and SiC particles have been used as reinforcement. The specimens were produced by using a gas pressure infiltration technique and mainly characterized by mechanical spectroscopy. Some of the specimens were unidirectionally solidified and oriented crystallographically.

### **3.1 Specimen processing by gas pressure infiltration**

Metal matrix composites are obtained by the infiltration of a preform (arrangement of reinforcing elements such as ceramic fibers or particles) by a molten metallic alloy. One way to achieve infiltration is squeeze casting. However, the air entrapment involved in conventional squeeze casting produces voids at the metal ceramic interfaces, which may decrease the mechanical properties. Moreover, the high pressure needed to push the molten metal into the preform may damage the fibers or induce inhomogeneous fiber distribution along the infiltration direction (Clyne 1987).

In order to avoid these problems, low pressure infiltration method has been used in this work. In this case, the infiltration pressure is strongly reduced, because the air in the preform has been evacuated by pumping before infiltration. Fig. 3.1 shows the schematic diagram of the infiltration apparatus and the related description. The infiltration procedure is given below.

The gas pressure infiltration apparatus has three major parts. (a). The melting chamber, (b) the injection chamber inside the vacuum chamber and (c) the high pressure valve that isolates the melting and the injection chamber.

Vacuum is first achieved in each chamber. Then, the preform is heated by a heating element, which surrounds the injection chamber. An induction furnace is used to melt the metal in a graphite crucible inside the melting chamber. The molten metal is then poured on the preheated preform (fig. 3.2). A graphite guide is placed in order to protect the valve and to guide

the metal into the mould. After closing the high pressure valve, which separates the injection chamber from the melting chamber, an argon pressure up to 3 MPa applied to push the metal into the gas evacuated preform.

After infiltration, the preform is rapidly cooled down by a forced cold air stream, which flows around the injection chamber. This allows one to minimize the contact time between the molten metal and the ceramic reinforcement, in order to reduce the interfacial reactions, which may degrade the composite properties.



Fig. 3.1a: Photo of the infiltration apparatus used in this research.

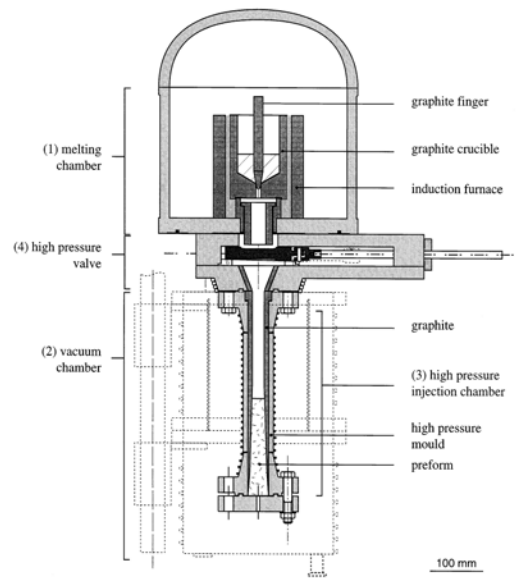


Fig. 3.1b: Schematic representation of the infiltration apparatus.

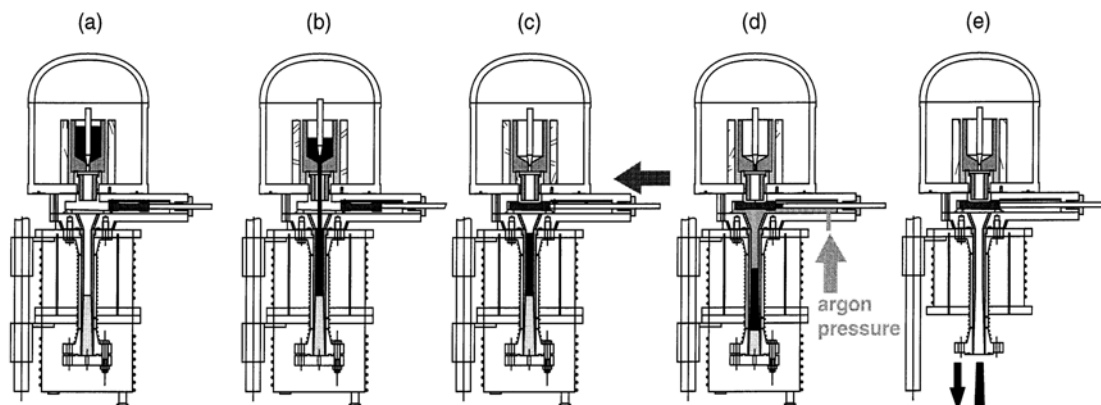


Fig. 3.2: Successive operation stages in the gas pressure infiltration method. (a) Melting, (b) casting, (c) gate valve closing, (d) injection, (e) de-moulding.

The operational stage of the infiltration apparatus is summarized in fig. 3.2.

Fig. 3.2 (a): Vacuum is made in both the melting and the injection chambers. The metal (magnesium) is melted in the melting chamber while the preform inside the injection chamber is preheated.

Fig. 3.2 (b): When the desired temperature for melting the metal (in this case it was 750°C) is reached in both in the melting chamber as well as in the injection chamber, the graphite guide is opened, which allows flow of molten metal from the upper to the lower chamber.

Fig. 3.2 (c): The gate valve is closed.

Fig. 3.2 (d): The argon with a pressure of 3 MPa is rapidly introduced in order to push the metal into the preform.

Fig. 3.2 (e): Immediately after the mould is cooled by forced cold air stream. After solidification the gas pressure is released by opening a pressure valve and when the room temperature is reached, the specimen is extracted by opening the bottom part of both the vacuum and injection chamber.

A brief description of the infiltration procedure can be obtained elsewhere (Carenno-Morelli 1998).

## 3.2 The preforms

We used a porous ceramic mould in order to keep the fibers in place. This mould is a  $\text{Al}_2\text{O}_3$  (SAFFIL) preform generally used for infiltration of MMC. The fibers were arranged inside a cavity of the mould in the desired orientation and then infiltrated. We machined the obtained specimen in order to keep just the fiber-matrix composite free from the alumina. Fig. 3.3 shows the orientation of the fibers in the preforms. In the present work, different kind of reinforcements (long C fibers, long stainless steel fibers, SiC particles) were incorporated in the magnesium matrix.

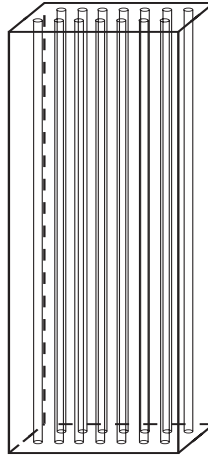


Fig. 3.3: Fibers parallel to the length of the composite axis.

### 3.3 Crystallographic orientation of the matrix

#### 3.3.1 Directional solidification

Some of the specimens were uni-directionally solidified by using a Bridgman technique (Kurz 1984) in order to have the matrix in a certain crystallographic orientation. The apparatus has three major parts as shown in fig. 3.4.

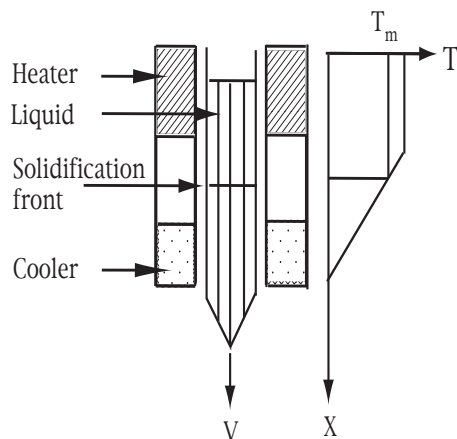


Fig.3.4a: Bridgman directional solidification method.

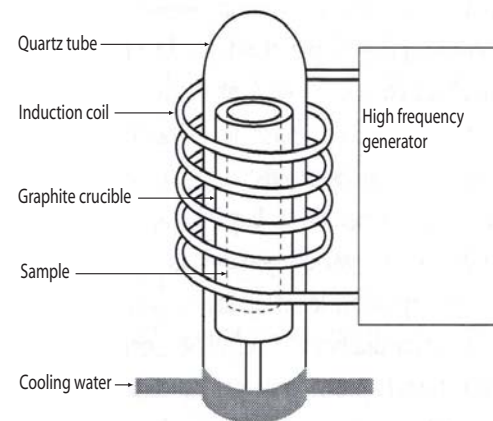


Fig. 3.4b: Schematic diagram of the directional solidification installation.

(a) An induction furnace consisting of an induction coil and a high frequency generator, (b) a graphite crucible in a quartz tube inside which the specimen is melted and (c) the bottom part connected to a running cold water. The sample was mounted in the graphite crucible and then re-melted in the induction furnace under a pressure of  $7 \times 10^4$  Pa argon gas. The crucible was

then pulled down through the temperature gradient at a controlled velocity of about 1 mm/min, so that the solidification front can move along the fiber-matrix interfaces (fig. 3.4 a).

### 3.3.2 Bragg-Brentano X-ray analysis

Bragg-Brentano XRD was performed to investigate the matrix crystallographic orientation of the specimens, which were uni-directionally solidified by the Bridgman technique. Fig. 3.5 shows a unit cell of hcp magnesium with 3 axes for indication of the crystallographic planes and a powder diffraction spectrum for pure magnesium. Two Mg/C composites were directionally solidified. Typical spectra resulting from X-ray diffraction on the cross section of the specimen (see fig. 3.7), i.e., perpendicular to the matrix-fiber interface are shown in fig. 3.6. The first spectrum consists of several peaks among which the ones corresponding to the (100) and (110) planes have the highest intensity. This suggests that, although the magnesium matrix has not been perfectly oriented, the surface perpendicular to the matrix-fiber interface is mainly composed of (100) and (110) planes. In other words, this means that the basal plane (001) is parallel to the interface. The second spectrum shows that the plane (002), which is parallel to the basal plane, has the highest intensity. This means that the orientation of the basal plane is perpendicular to the interface.

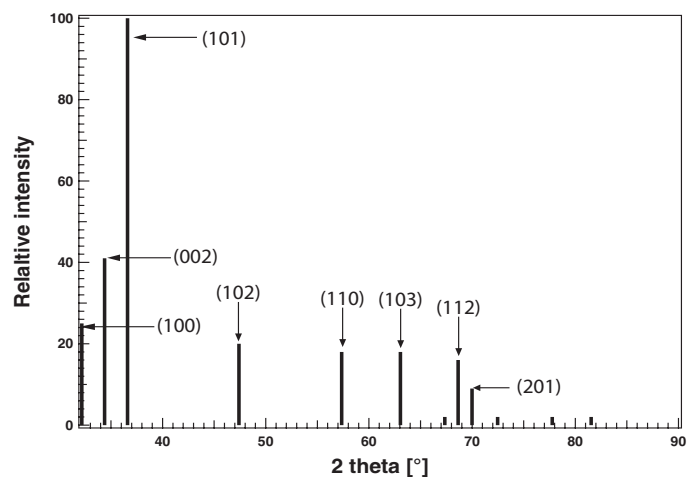
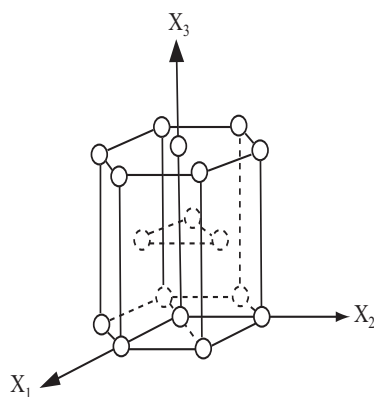


Fig. 3.5a: Unit cell of magnesium, with the 3 axes used for crystallographic plan indexation.

Fig. 3.5b: Powder diffraction spectrum of pure magnesium obtained from PDF (Powder Diffraction File).

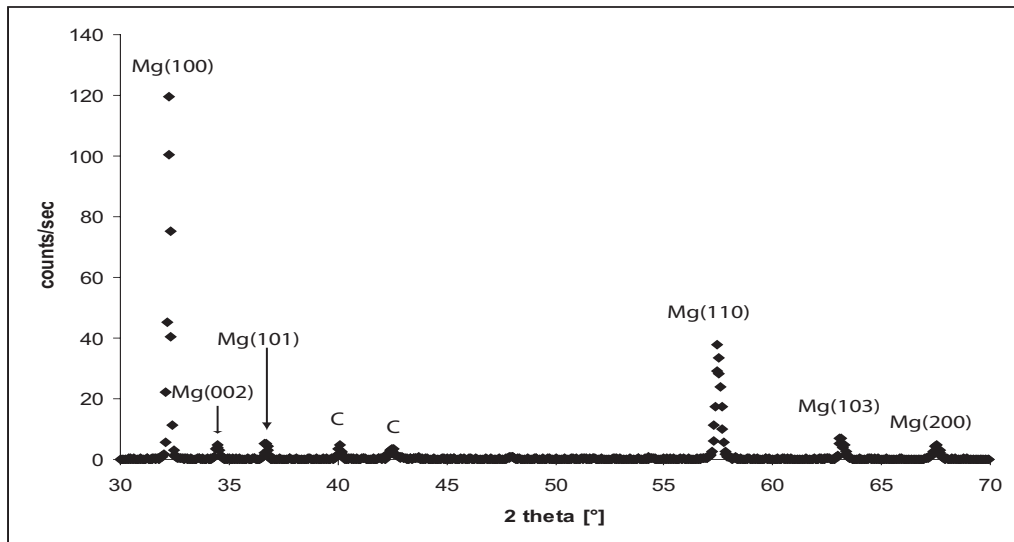


Fig. 3.6a: X-ray diffraction spectrum of the Mg/C sample where the basal plane is parallel to the interface.

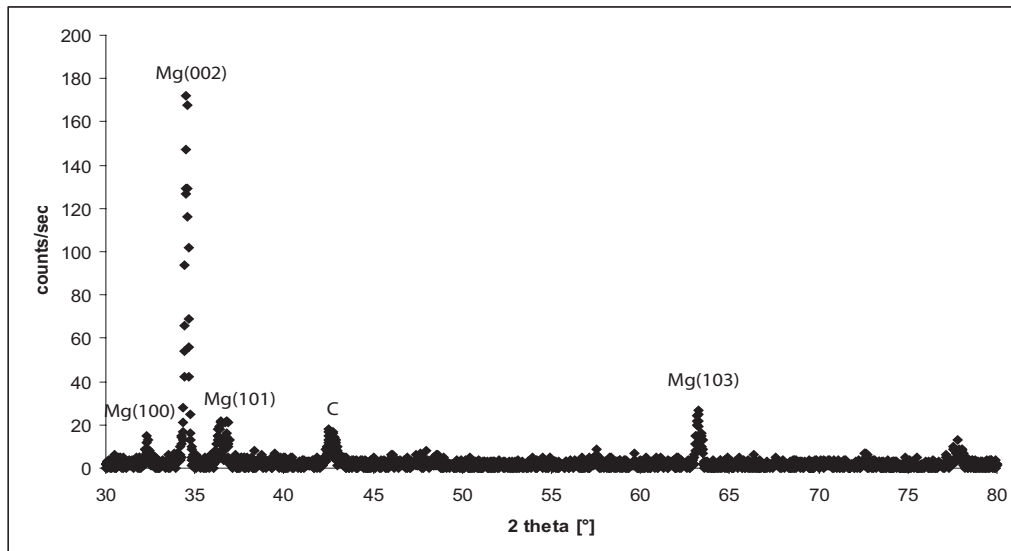


Fig. 3.6b: X-ray diffraction spectrum of the sample Mg/C where the basal plane is perpendicular to the interface.

Samples were also investigated in the as infiltrated condition. In a polycrystalline sample, the crystallographic planes are randomly oriented and one can assume that the basal plane makes an average angle of  $45^\circ$  with respect to the interface. Thus, three different orientations of the basal plane in the case of Mg/C composites were obtained.

- Basal plane at an angle of  $90^\circ$  with respect to the interface
- Basal plane at an angle of  $45^\circ$  with respect to the interface
- Basal plane at an angle of  $0^\circ$  with respect to the interface.

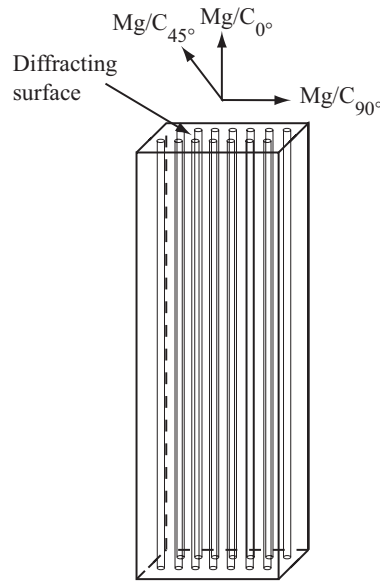


Fig. 3.7: Schematic diagram with the indication of the C-axis for the specimens.

### 3.4 Nomenclature of the processed samples

Due to the large number of samples with different orientations of the fibers and of the matrix, it is convenient to describe the samples with a particular name. The nomenclatures of the samples are based on the reinforcement type and on the orientation of the basal plane.

- $\text{Mg/C}_{90^\circ}$ : Pure magnesium reinforced with long carbon fibers along the composite axis. The basal plane normal makes an angle of  $90^\circ$  with respect to the fiber axis.
- $\text{Mg/C}_{45^\circ}$ : Pure magnesium reinforced with long carbon fibers along the composite axis. The basal plane normal makes an angle of  $45^\circ$  with respect to the fiber axis.
- $\text{Mg/C}_{0^\circ}$ : Pure magnesium reinforced with long carbon fibers along the composite axis. The basal plane normal makes an angle of  $0^\circ$  with respect to the fiber axis.
- $\text{Mg/steel}$ : Pure magnesium reinforced with long stainless steel fibers along the composite axis whereas the basal plane normal makes an angle of  $45^\circ$  with respect to the fiber axis.
- $\text{Mg/SiC}_{\text{particles}}$ : Pure magnesium reinforced with SiC particles and randomly oriented.
- $\text{Mg}_{\text{pure}}$ : Pure magnesium unreinforced and randomly oriented.
- $\text{Mg-Ni/CNT}$ : Mg-23wt% Ni alloy reinforced with 2wt% carbon nanotubes and randomly oriented.

### 3.5 Characterization by microscopy

Fig. 3.8 shows micrographs of the cross section of some of the samples. Scanning electron microscopy was performed on the samples Mg/C<sub>90°</sub>, Mg/steel and Mg/SiC<sub>particles</sub>, while the rest of the samples were investigated by means of optical microscopy. The micrographs show that the fibers are almost homogeneously distributed in the matrix. In some cases, fiber breakout and the presence of porosity were observed. The interfacial contact between the matrix and the fibers were good in most cases.

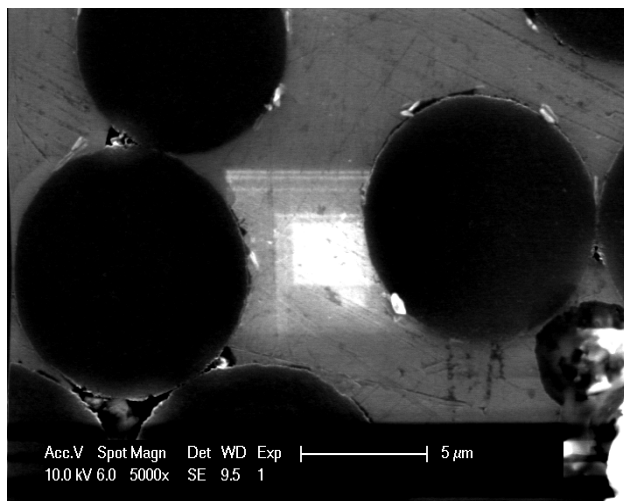


Fig. 3.8a: SEM micrograph of a cross section of the sample Mg/C<sub>90°</sub>.

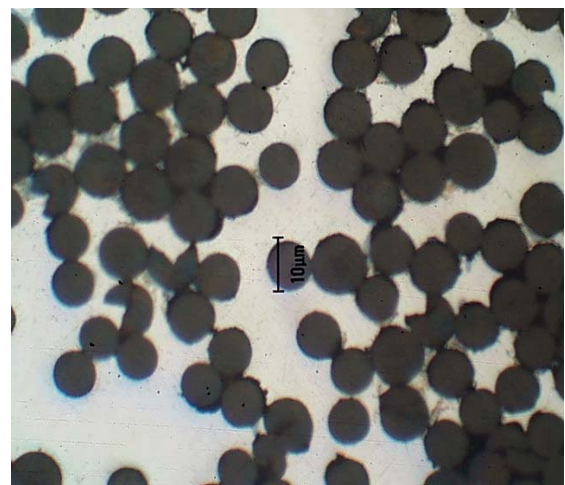


Fig. 3.8b: Optical micrograph of a cross section of the sample Mg/C<sub>45°</sub>.

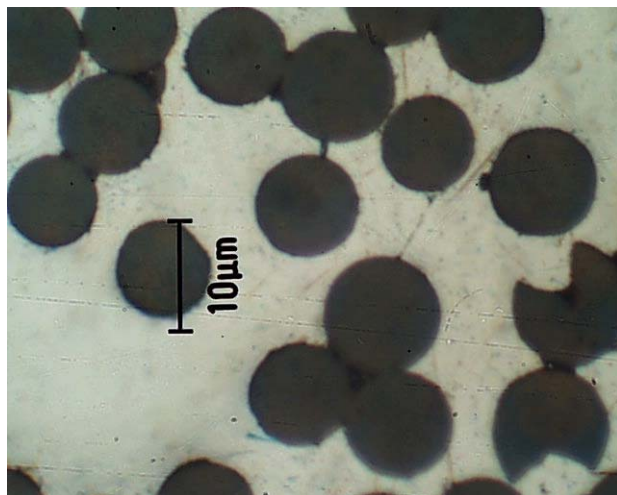


Fig. 3.8c: Optical micrograph of a cross section of the sample Mg/C<sub>0°</sub>.

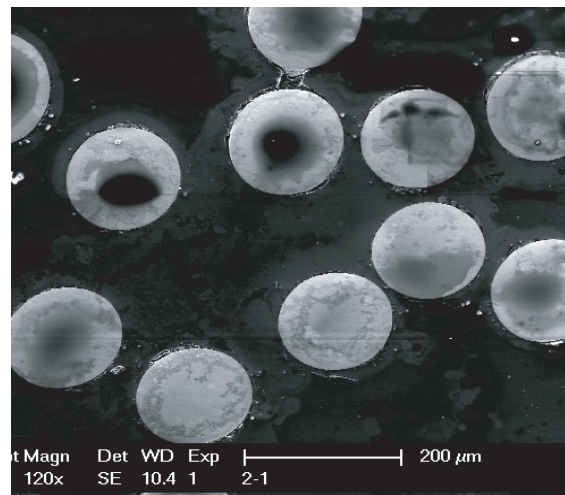


Fig. 3.8d: SEM micrograph of a cross section of the sample Mg/steel.



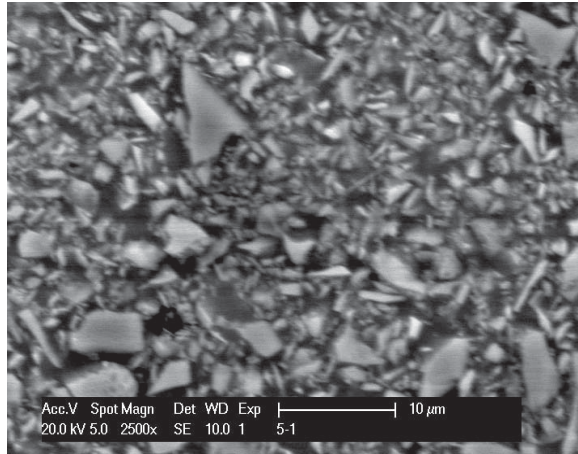


Fig. 3.8e: SEM micrograph of a cross section of the sample Mg/SiC<sub>particles</sub>.

## 3.6 Mechanical spectroscopy

Mechanical spectroscopy measurements of the samples were performed in an inverted torsional pendulum either in free mode or in forced mode. For measuring the elastic modulus, a free-free bar apparatus was also used. A short description of all the different apparatus is given below.

### 3.6.1 Free decay torsion pendulum: (resonant system)

In a free pendulum, the specimen is excited at the resonant frequency. When the excitation is stopped, the free decay of the oscillations is observed and the mechanical loss is obtained from the logarithmic decrement (eq. 2.20). The resolution of the measurements was about  $0.3 \times 10^{-3}$ . The shear modulus ( $G$ ) was determined from the vibration frequency with a period of  $T$ , using the relation

$$G = (128\pi LI)/T^2 d^2 \quad (3.1)$$

where  $L$  and  $d$  are the sample length and diameter respectively, and  $I$  is the moment of inertia of the pendulum. Fig. 3.9 shows a schematic diagram of a free decay pendulum, where the different parts are labeled.

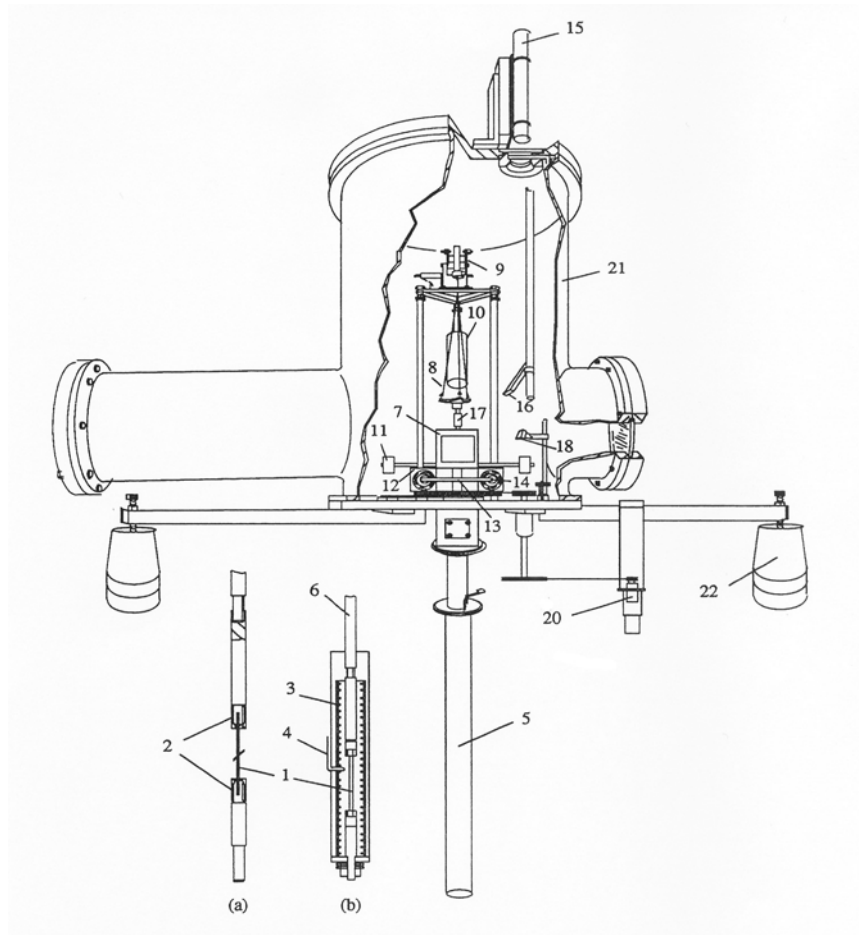


Fig. 3.9: Schematic diagram of a free decay pendulum (Parrini 1995). (a) Specimen holder, (b) pendulum interior part inside the furnace. (1) specimen, (2) grips, (3) furnace, (4) thermocouple, (5) steel protection, (6) rigid transmission rod, (7) inertia balancing-pole, (8) three-wire system, (9) balance, (10) counterweight to avoid axial stress on the specimen, (11) inertia masses to control the vibration frequency, (12) two toroidal coils for vibration excitation, (13) S-shaped balancing pole, (14) permanent magnet, (15) laser, (17) & (18) mirrors, (19) invisible linear photodetector on the left of Fig. 3.10, (20) servo-motor to contract decentering and for cold working, (21) vacuum vessel, (22) anti-vibratory suspensions.

### 3.6.2 Forced pendulum: (sub resonant mode)

Eq. 2.24 shows that for the case of forced oscillations, the mechanical loss can be calculated directly from the phase lag between the applied stress and the corresponding strain in the sample.

A specimen is set into forced vibration at a frequency  $\omega$ , far below the resonant frequency. Measurements are then performed both as a function of frequency and temperature. Fig. 3.10 shows the schematic diagram of a forced pendulum.

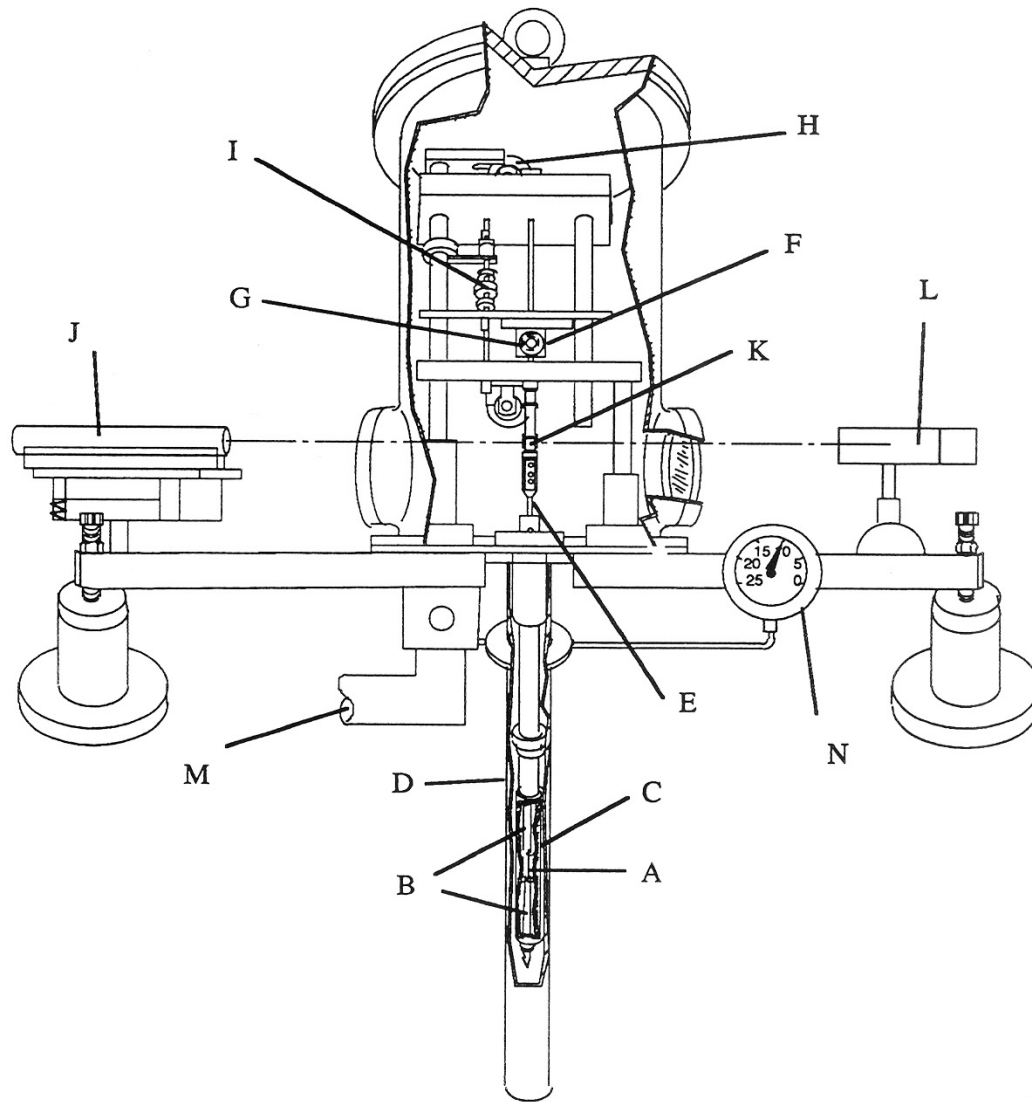


Fig. 3.10: Schematic diagram of a forced vibration pendulum (Parrini 1995). (A) Specimen, (B) Grips, (C) Furnace, (D) Cryostat, (E) Extension rod, (F) Helmholtz coils, (G) Permanent magnet, (H) Suspension system, (I) Counter weight, (J) Laser generator, (K) Mirror, (L) Photodetector, (M) Vacuum system, (N) Vacuum gauge.

The specimen (A) is held by two grips (B). The bottom is fixed, while the top is freely suspended by a suspension system (H) through an extension rod (E). The suspension (H) suppresses the transverse vibrations. A metal weight (I) was used to counter balance the rod weight. The torsion stress  $\sigma$  is applied to the sample by passing a current through the Helmholtz coils (F), which exerts a magnetic force on the permanent (G) magnet on the extension rod (E). The response of the specimen  $\varepsilon$  is measured by the displacement of a laser beam, which is reflected by the small mirror (K) onto the photo detector (L). Moreover, the specimen (A) is surrounded by a furnace (C) and a cryostat, which allow one to control the temperature. Vacuum is achieved by a turbo pump attached to the system. An electrical

generator incorporated in a commercial frequency response analyzer (Schlumberger 1250 FRA) produces an electric signal. The frequency response analyzer measures the phase lag and amplitude ratio between the two signals (phase resolution of  $10^{-4}$  rad for a frequency range from  $10^{-5}$  Hz to  $10^{-4}$  Hz) (Parrini 1995).

### 3.6.3 Free-free vibrating rod installation

The free-free vibrating rod installation (fig. 3.11) works in resonance mode. The principle is to excite the sample at its resonant frequency by means of an excitation-detection electrode. A rectangular sample suspended between two pairs of thin wires is placed at nodal lines of the first flexural vibration mode. The electrode positioned above the center of the sample, forms with it a capacitor (Vittoz 1963).

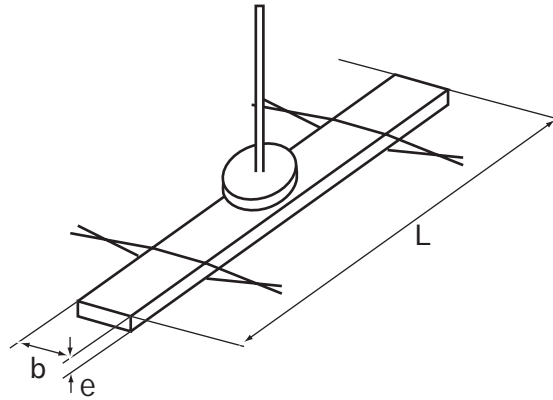


Fig. 3.11: schematic diagram of free-free vibrating rod installation.

The resonant frequency of the bar is given by:

$$f = 1.03 \frac{e}{L^2} \sqrt{\frac{E}{\rho}} \quad (3.2)$$

Where  $E$  is the Young's modulus,  $L$  is the length of the sample,  $\rho$  is the density and  $e$  is the thickness of the sample. From eq. 3.2 one can calculate the Young's modulus:

$$E = 0.943 \frac{\rho L^4}{e^2} f^2 \quad (3.3)$$

After stopping the excitation, the mechanical loss can be calculated from the logarithmic decrement of the free decay of the oscillations:

$$\tan \phi = \frac{1}{n\pi} \ln \frac{A_i}{A_{i+n}} \quad (3.4)$$

where  $A_i$  and  $A_{i+n}$  are the  $i^{\text{th}}$  and the  $(i+n)^{\text{th}}$  amplitudes in the free decay.



## Chapter 4: Experimental results and analysis

In this chapter, the characteristic mechanical loss spectra of the different composites are presented. For all of the specimens, the mechanical loss was first measured as a function of temperature for cooling and heating between 100 K and 500 K at a temperature rate  $\dot{T} = 2\text{K/min}$  and frequency of 1 Hz. Moreover, detailed analysis was based on systematic measurements varying the heating/cooling rates  $\dot{T}$  from 1 to 3 K/min, the excitation frequency from 0.01 to 1 Hz, the stress amplitude from 0.018 to 1.8 MPa and the strain amplitude varied from  $1 \times 10^{-5}$  to  $9 \times 10^{-5}$ , respectively. The samples were also annealed at different temperatures for 1 hour.

### 4.1 Characteristic mechanical loss and corresponding shear modulus spectra

Fig. 4.1 shows the mechanical loss spectrum of a Mg/C<sub>45°</sub> specimen (see fiber arrangement and microstructure in figs. 3.7 and 3.8b) measured during a heating and cooling cycle at  $\dot{T} = 2\text{K/min}$ . A pronounced thermal hysteresis between the curves obtained upon heating and upon cooling is observed. During heating, the mechanical loss increases as a function of temperature from 100 to 350 K, then it saturates. During annealing at 500 K for 10 minutes, the mechanical loss decreases markedly. Upon cooling, the mechanical loss increases first continuously from 500 to 200 K and then decreases. Fig. 4.1 also shows the temperature evolution of the normalized elastic shear modulus, i.e., the variations of the shear modulus with respect to its value at 300 K. The shear modulus increases during cooling and decreases during heating. In other words, the elastic shear modulus exhibits a normal trend as it decreases when temperature increases. However, an anomalous behavior appears between 350 and 425 K, where a variation of the curve slope is observed both upon heating and upon cooling.

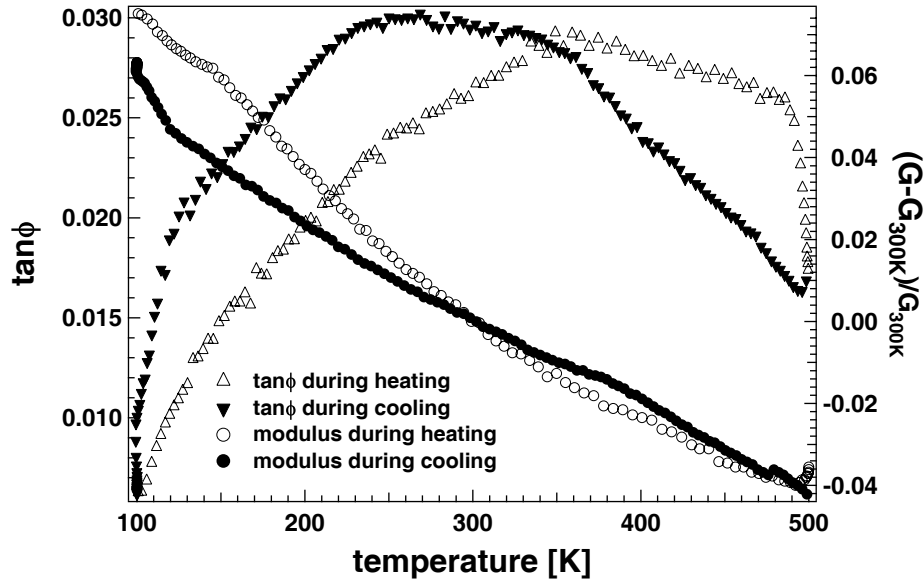


Fig. 4.1: Mechanical loss  $\tan\phi$  and the relative elastic shear modulus as a function of temperature for cooling and heating at a temperature rate of  $\dot{T} = 2$  K/min in Mg/C<sub>45°</sub> and  $\omega = 0.2$  Hz.

Even if the microstructure of Mg/steel composite (fig 3.8d) differs from the one of Mg/C by the size of the reinforcements, the mechanical loss spectra are similar (fig 4.2). The mechanical loss exhibits a thermal hysteresis between the curves obtained upon heating and cooling. During heating, the damping increases with temperature from 100 to 370 K, and then a drop is observed with a local minimum at 420 K. Again the mechanical loss decreases during a 500 K annealing. Upon subsequent cooling, it starts to increase again only from 400 K to 300 K, then it is almost constant until 150 K and decreases rapidly at the end of the cooling cycle. The thermal hysteresis is particularly important for the shear modulus. From 150 to 500 K, the modulus is lower upon heating than upon cooling. Moreover the modulus anomaly is more pronounced. Indeed, upon heating, the shear modulus exhibits an anomalous increase with temperature between 350 and 420 K, and an anomalous decrease during cooling in the same temperature range.



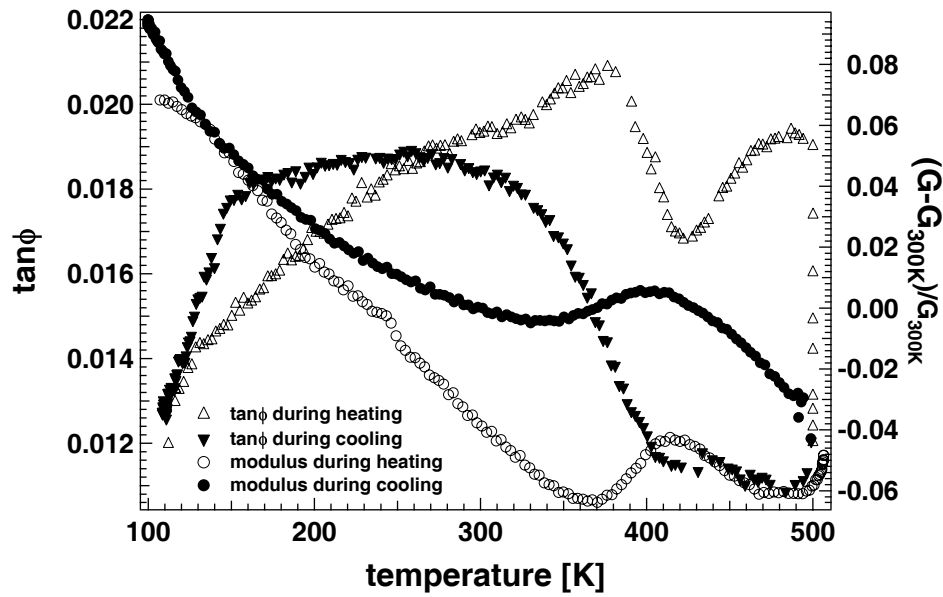
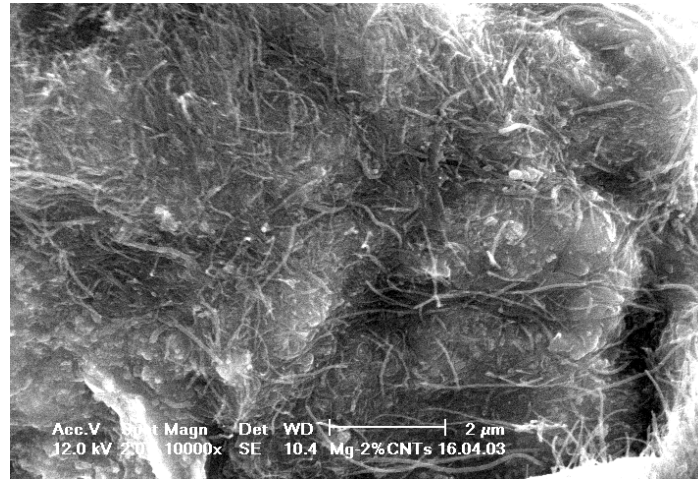
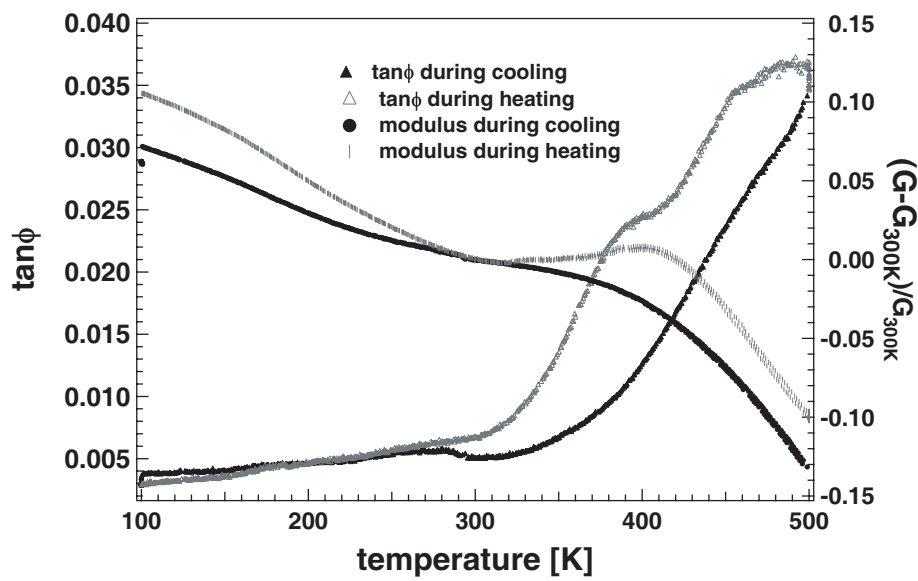


Fig. 4.2: Mechanical loss  $\tan\phi$  and relative shear modulus as a function of temperature for the Mg/steel composite during cooling and heating at a temperature rate  $\dot{T} = 2$  K/min and  $\omega = 0.5$  Hz.

With respect to the Mg/C composites with micro-sized reinforcements (carbon fibers have a diameter of 5 to 10  $\mu\text{m}$ ), the Mg/steel composites contain reinforcements with a diameter 10 times larger (about 0.1 millimeter). However, the mechanical loss and shear modulus spectra are rather similar, with thermal hysteresis and modulus anomaly. It is then interesting to compare these spectra with the one of composites containing nano-sized reinforcements. Consequently, an alloy of Mg-23%Ni reinforced with carbon nanotubes (Mg-Ni/CNT), which was processed by powder metallurgy, has also been measured. Fig. 4.3a presents the microstructure of such composites and fig. 4.3b their mechanical loss and relative shear modulus spectra obtained during a thermal cycle. The thermal hysteresis between heating and cooling is less pronounced than in the case of long fiber reinforced composites. However, a thermal hysteresis in the modulus curves and a pronounced anomaly between 300 and 400 K are observed.



a)



b)

Fig. 4.3 a): Microstructure of a Mg-Ni/2 wt% CNT as observed by scanning electron microscopy. b) Mechanical loss  $\tan\phi$  and relative shear modulus as a function of temperature for the Mg-Ni/2 wt% CNT composite during cooling and heating measured in a free pendulum.

On the other hand, in the case of composites, where the reinforcement is constituted by almost spherical particles, such as in Mg/SiC<sub>particles</sub> (see fig. 3.8e), the mechanical loss shows a small hysteresis between heating and cooling mainly at temperatures lower than the room temperature. Moreover, no modulus anomaly is observed (fig. 4.4).

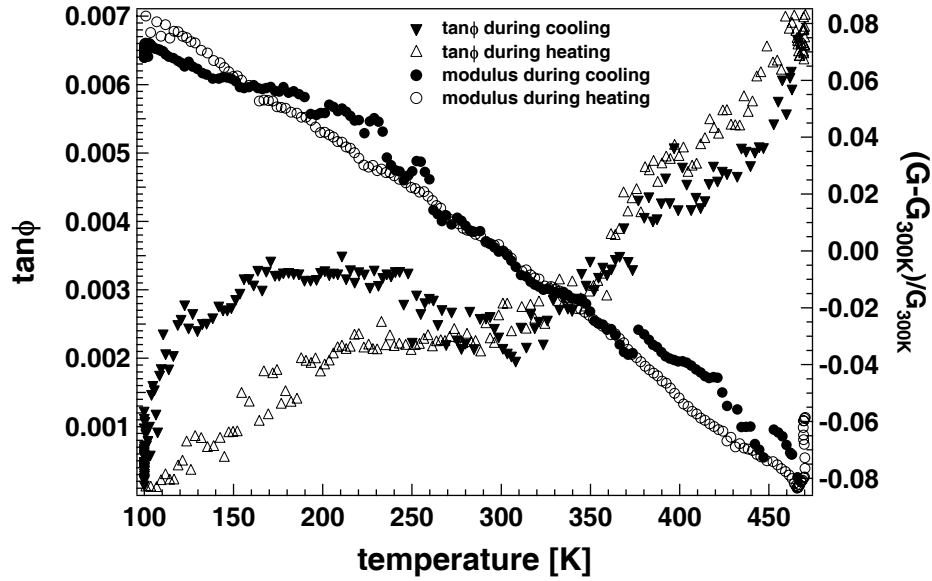


Fig. 4.4: Mechanical loss  $\tan\phi$  and relative shear modulus as a function of temperature for the Mg/SiC<sub>particles</sub> composite during cooling and heating at a temperature rate  $\dot{T} = 2$  K/min and  $\omega = 0.5$  Hz.

In order to look for the origin of damping in a composite, it is interesting to compare the mechanical loss spectra of the constituents with the one of the composite. As it is very difficult to measure the mechanical loss of a carbon fiber, the magnesium matrix has been measured.

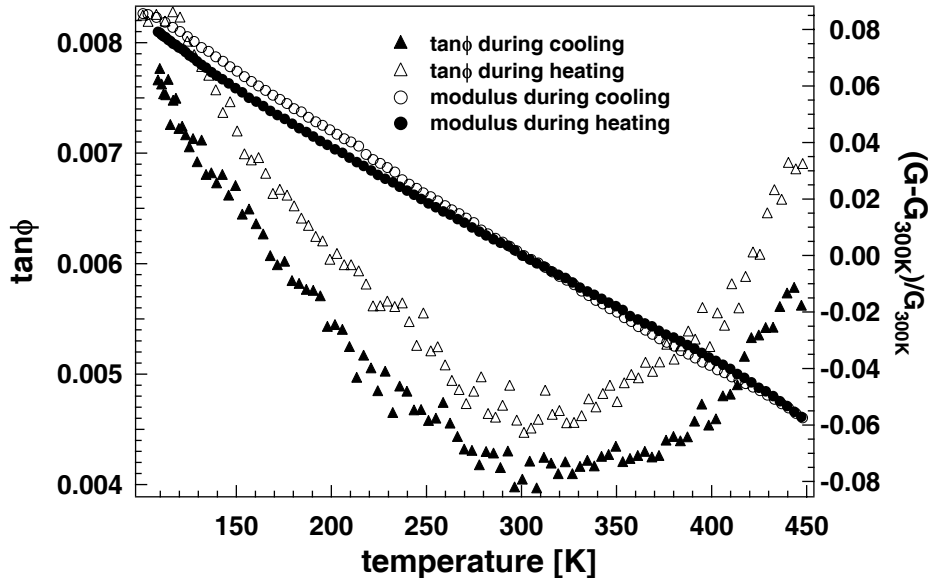


Fig. 4.5: Mechanical loss  $\tan\phi$  and relative shear modulus as a function of temperature for pure Mg during cooling and heating at a temperature rate  $\dot{T} = 2$  K/min and  $\omega = 0.5$  Hz.

Fig. 4.5 shows the mechanical loss and elastic shear modulus spectrum of unreinforced magnesium of commercial purity (99.98 wt % Mg) obtained during a thermal cycle between

100 and 500 K at a rate of  $\dot{T} = 3$  K/min. The mechanical loss does not exhibit any significant thermal hysteresis, but rather an irreversible decrease after annealing at 500 K.

As a function of temperature, the mechanical loss decreases upon heating up to 300 K then increases. In very pure magnesium, it was found that dislocation motion gives rise to two Bordoni relaxation peaks (Reihani 1979, N6 1990). The mechanical loss decrease at low temperatures would be the high temperature part of a broad low temperature peak. This broad damping maximum observed in magnesium of commercial purity can be interpreted as due to dislocation damping. The broad maximum would result from the broadening of the Bordoni peaks because of the impurity effects. At 500 K, the mechanical loss decreases during annealing, due to dislocation re-arrangement or dislocation pinning. The damping shows a similar temperature spectrum upon cooling but of lower amplitude.

The shear modulus shows a normal trend of continuous decrease as a function of temperature, without any anomaly in the curves (fig. 4.5).

## **4.2 Effects of the heating and cooling rate $\dot{T}$ and of the vibration frequency $\omega$**

It has been observed that in composite materials the mechanical loss depends on the heating or cooling rate and the excitation frequency (Chowdhury 2008, 2009). Fig. 4.6 shows that the damping in Mg/C composite increases strongly with the heating rate  $\dot{T}$ . On the other hand, it decreases by increasing the excitation frequency  $\omega$ , as shown in fig. 4.7.

Moreover, no temperature shift of the mechanical loss spectrum is observed when the frequency is changed even by a factor of 10. This indicates that the internal friction mechanism is not thermally activated. The observed dependence of the mechanical loss on frequency and temperature rate has been interpreted as due to transient dissipation phenomena, which disappears in isothermal measurements. These effects are referred to as transient damping.

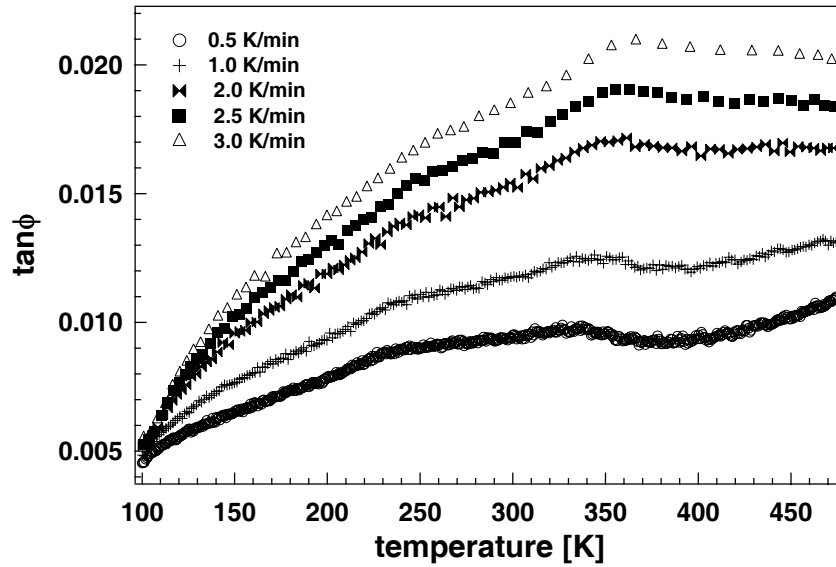


Fig. 4.6: Mechanical loss  $\tan\phi$  as a function of temperature for different temperature rate  $\dot{T}$  at a constant excitation frequency 0.5 Hz during heating in the composite Mg/C<sub>45°</sub>.

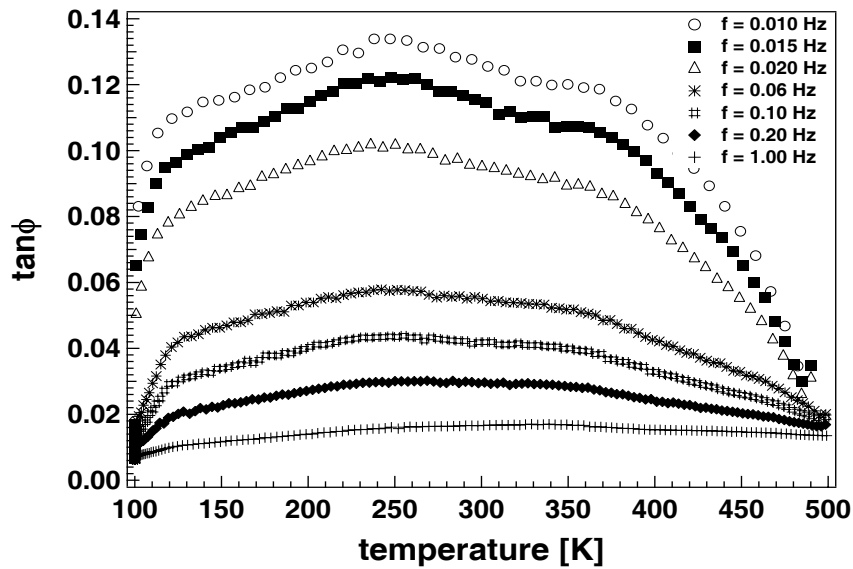


Fig. 4.7: Mechanical loss  $\tan\phi$  as a function of temperature for different excitation frequencies at a constant temperature rate  $\dot{T} = 2$  K/min during cooling in the composite Mg/C<sub>45°</sub>.

In order to highlight the transient damping component, the mechanical loss of the composites has been measured during heating and cooling cycles interrupted by annealing of 60 minutes at 25 K temperature interval. Fig. 4.8 shows the results obtained in Mg/C<sub>45°</sub>.

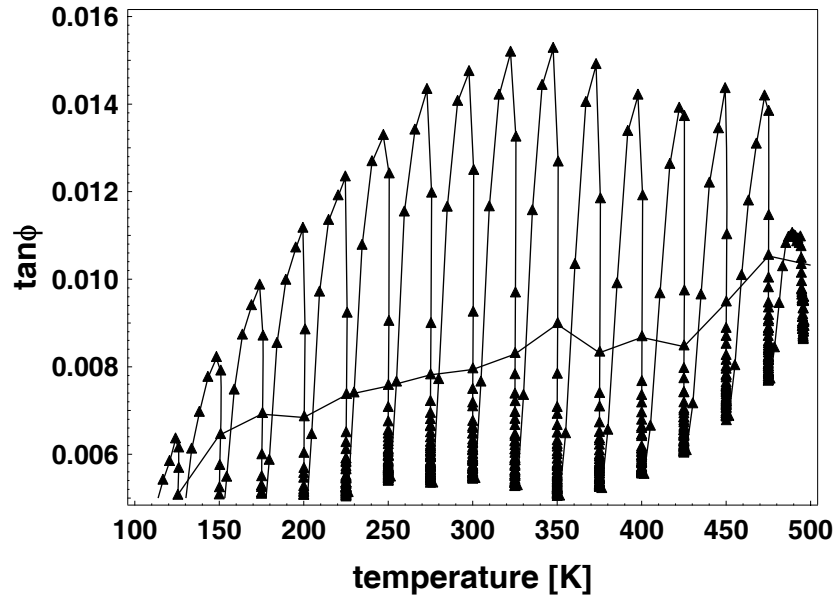


Fig. 4.8: Mechanical loss  $\tan\phi$  as a function of temperature in Mg/C<sub>45</sub>°. The solid line shows the point of transition between the transient damping and the microstructure evolution damping.

During annealing, the mechanical loss decreases until it reaches a lower equilibrium value. This may be interpreted by the fact that when  $\dot{T} = 0$  the transient damping disappears. At the end of each annealing, switching on heating or cooling gives rise to a rapid increase of the mechanical loss until it reaches the value characteristic of the set temperature rate. The difference in damping between the values obtained upon heating (or cooling) for a given temperature rate and the values reached at the end of the isothermal annealing can be considered as the transient damping. In the case of diffusionless martensitic transformation (San Juan 2001), the transient damping was obtained by a simple subtraction of the two curves: the curve obtained for  $\dot{T} \neq 0$  and the curve for  $\dot{T} = 0$ . However, in the case of present metal matrix composites, we have noticed that subtracting the mechanical loss values obtained at the end of isothermal annealing (lowest damping level in fig. 4.8) gives too high values for the transient damping. Indeed, this simple operation yields a value of the transient damping, which does not reach zero for  $\dot{T} = 0$ . This is in contradiction with the definition of transient damping (see eq. 2.47).

By considering more carefully the measured points of the mechanical loss in fig. 4.8, which were taken at regular time intervals, one notes that the decrease of damping as a function of time would not be a linear function.

Also, the evolution of the mechanical loss during isothermal annealing has been plotted as a function of time. For instance such a time dependence of the mechanical loss is shown in fig. 4.9 for a 300 K isothermal annealing in Mg/C<sub>45</sub>. The time dependence of the transient damping exhibits two regimes: a fast, almost linear, evolution, which may be interpreted as the true transient damping and a slower evolution of exponential form, which may be associated with a time dependent microstructure evolution.

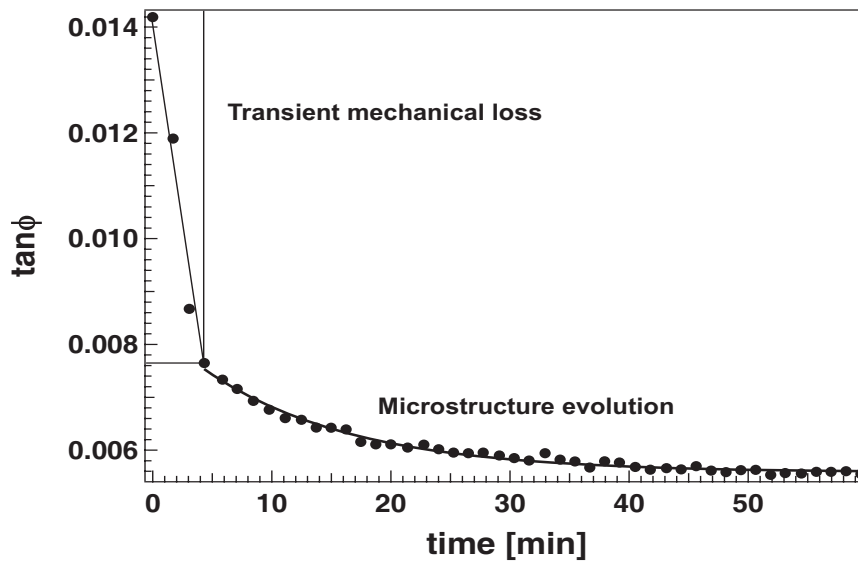


Fig. 4.9: Mechanical loss  $\tan\phi$  as a function of time at 300 K at a constant frequency of 0.5 Hz in Mg/C<sub>45</sub>.

When the heating/cooling rate is set to zero, the transient damping should go to zero instantly, but  $\dot{T} = 0$  is not instantaneous in all the volume of the specimen. A fast linear trend is observed, which corresponds to the relaxation of thermal stress when the temperature variation is stopped. On the other hand, during annealing, thermal stresses are also relaxed by the microstructure evolution, which can lead to a slow decrease of damping.

In the plot of the mechanical loss as a function of time (fig. 4.9), the transition between the two regimes is very clear. As a consequence, such plots have been considered for each isothermal annealing in order to extract the true transient damping from the complete evolution of the mechanical loss with time.

In fig. 4.8, the solid line shows the points of transition between the transient damping and the microstructure evolution damping. Taking into account this way to discriminate the transient

component from the total damping, it was possible to plot the transient damping as a function of  $\dot{T}/\omega$  (fig. 4.10).

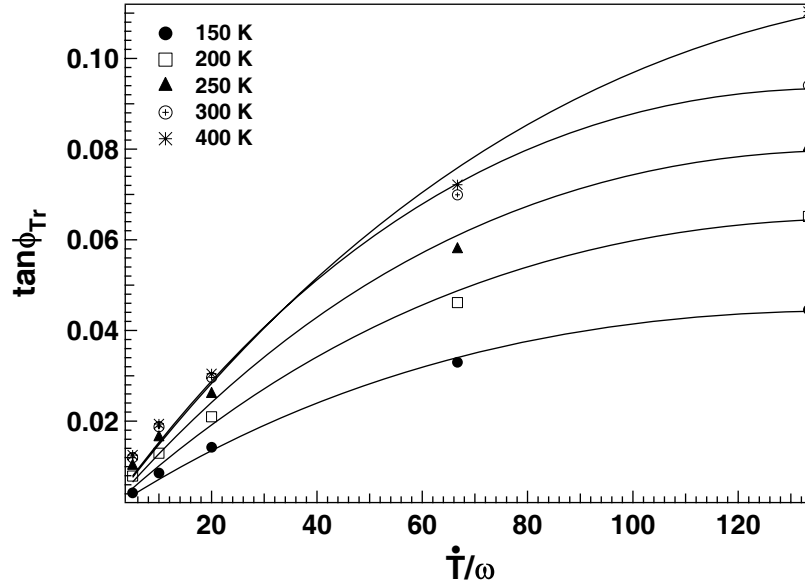


Fig. 4.10: Transient mechanical loss  $\tan\phi_{Tr}$  as a function of  $\dot{T}/\omega$  for different temperatures during heating in the composite Mg/C45°. Solid lines correspond to fitting curves at different temperatures.

One observes in fig. 4.10, that the dependence of the transient mechanical loss on  $\dot{T}/\omega$  is non linear and that the transient damping component is zero for  $\dot{T}/\omega = 0$ .

### 4.3 Analysis of the transient damping by the model of Mayencourt

In situ TEM observations have shown that the thermal stresses, which are built at the reinforcement-matrix interfaces, are relaxed by dislocation motion in the case of magnesium matrix (Mayencourt 1999). Moreover, this dislocation motion was found to be of hysteretic type. As a consequence, Mayencourt developed a theoretical model (Mayencourt 1998), which accounts for the transient mechanical loss as due to dislocation motion controlled by solid friction forces. In this case, the theoretical model yields the equations 2.47-2.48, which account for the transient damping and are re-written here below:



$$\tan \phi = 2C_1 C_2 \frac{\dot{T}}{\omega} \frac{1 - \frac{\pi}{2} C_2 \frac{\dot{T}}{\omega}}{1 + \frac{\pi}{2} C_2 \frac{\dot{T}}{\omega}} \quad (2.47)$$

With

$$C_1 = \frac{\Lambda b^2}{J_{el} K} \quad \text{and} \quad C_2 = \frac{CE\Delta\alpha}{\sigma_0} \quad (2.48)$$

The dependence of  $\tan \phi$  on  $\frac{\dot{T}}{\omega}$  is non linear, and accounts well for the results in fig. 4.10, where the solid lines have been calculated from the above equation with  $C_1$  and  $C_2$  as fitting parameters. It was also shown that the non linear dependence accounts for dislocation movement controlled by solid friction forces, the motion of which is hysteretic. In the case of viscous friction, the dependence of the transient damping on  $\dot{T}$  should be linear (Mayencourt 1999). This is obviously not the case here.

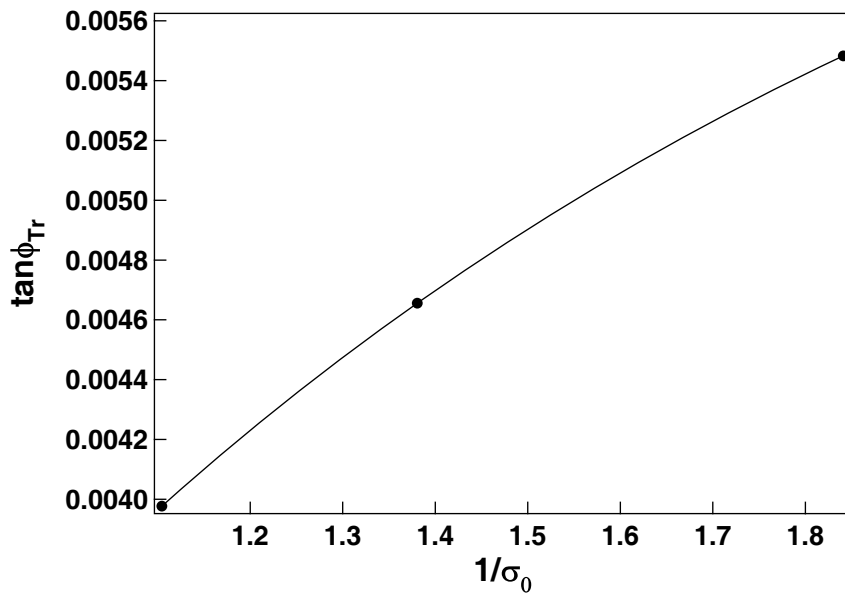


Fig. 4.11: Transient Mechanical loss  $\tan \phi_{tr}$  as a function of  $1/\sigma_0$  in Mg/C45°.

Moreover, the model predicts that the transient damping depends on the vibration amplitude ( $\sigma_0$ ) via the  $C_2$  parameter. Fig. 4.11 shows that the dependence of the transient damping obeys the above equations (eqs. 2.47 and 2.48), which allowed one to calculate the solid line in fig. 4.11, which fits well the experimental points.

These results confirm that the theoretical model of Mayencourt is very well suited for analyzing the transient mechanical loss in magnesium matrix composites. This transient damping reveals the interface thermal stress relaxation by dislocation motion in the magnesium matrix.

Result exploitation can be achieved by using the model. Indeed, the fits obtained using Eq. 2.47 give the two fitting parameters  $C_1$  and  $C_2$ , which evolve with respect to the temperature (figs. 4.12 and 4.13).

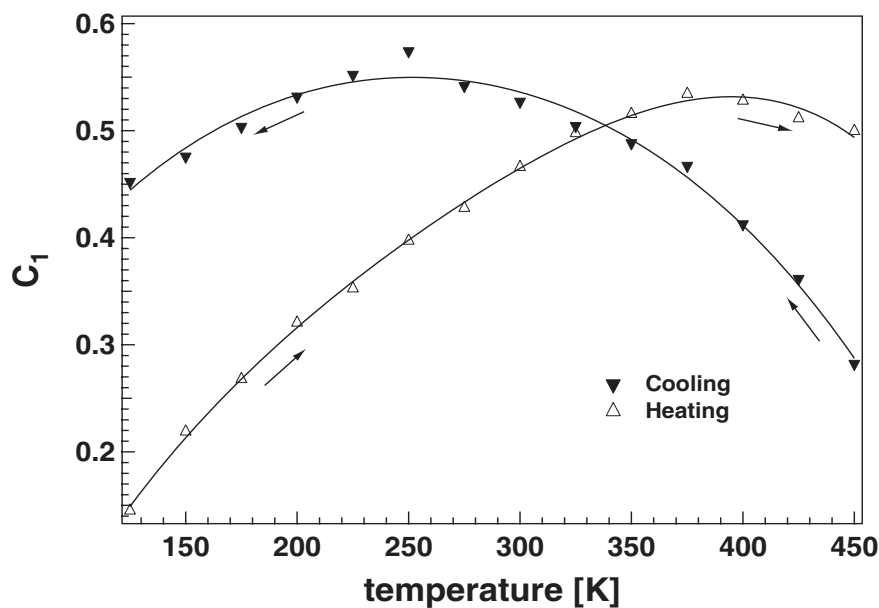


Fig. 4.12:  $C_1$  as a function of temperature for the composite Mg/C45°.

Fig. 4.12 shows the evolution of the fitting parameter  $C_1$  with respect to the temperature during cooling and heating. A marked hysteresis is observed between the values obtained upon heating and cooling.  $C_1$  is sensitive to the mobile dislocation density  $\Lambda$  (eq. 2.48). When the temperature is varied, dislocations are emitted towards or away from the interface in order to relax the thermal stresses. During heating, as the matrix is expanding more than the fiber, the thermal stress is relaxed by moving dislocations towards the interface. The mobility of the dislocations also increases upon heating, which contributes to an increase of  $C_1$ . During cooling, the matrix contracts more than the fiber and is under tensile stress. The mismatch in the thermal expansion coefficient between the matrix and the fiber is relieved by emitting dislocations away from the interface. Below 200 K,  $C_1$  decreases during cooling. This occurs because at very low temperatures the mobility of the dislocation is reduced.

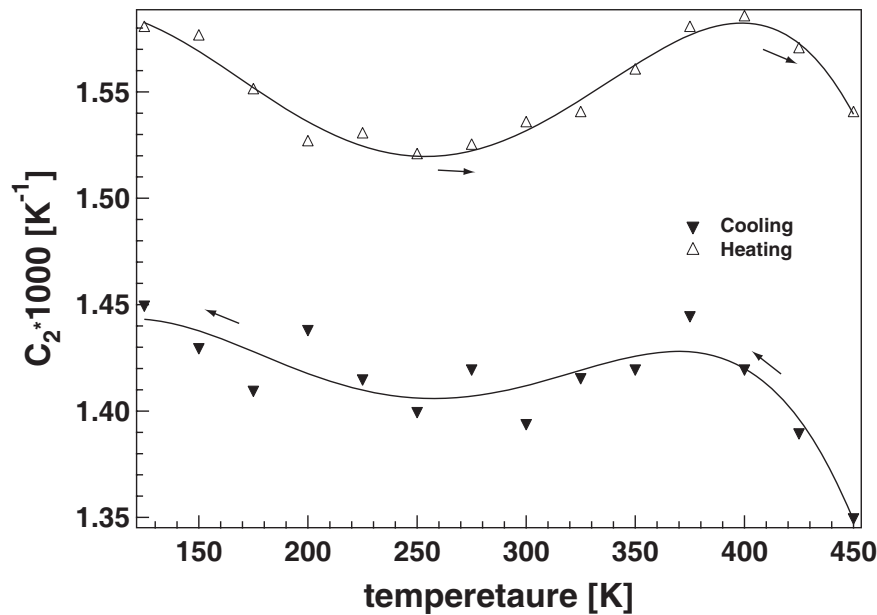


Fig. 4.13:  $C_2$  as a function of temperature for the composite Mg/C45°.

Fig. 4.13 shows the evolution of the fitting parameter  $C_2$  with respect to the temperature during cooling and heating.  $C_2$  represents the interfacial bonding between the matrix and the reinforcement.  $C_2$  follows almost the same trend as the shear modulus of the composite. It is observed that  $C_2$  decreases first with increasing the temperature then it increases around 400K and then decreases again. It is interesting to notice that even if  $C_2$  is extracted from the mechanical loss data, it shows in all cases a trend very close to that of the elastic modulus, which is measured independently. In fact, eq. 2.48 shows that  $C_2$  is indeed proportional to the elastic modulus  $E$  and the geometrical structure factor  $C$ , which is closely dependent on the bonding between fibers and the matrix. As discussed before, the overall modulus of the composite depends on the bonding strength. The contribution of these two parameters ( $E$  and  $C$ ) to  $C_2$  cannot be distinguished but apparently they act jointly.

#### 4.4 Thermal hysteresis

The thermal hysteresis observed in figs. 4.1, 4.2, 4.3 is typical for magnesium matrix composites and may be attributed to the inversion of the thermal stresses at the end of heating and cooling cycles. The mechanical loss increases upon heating up to about 350 K and then it is almost saturated. Upon cooling, one can observe a curve similar to that obtained upon heating but shifted to lower temperatures. Upon heating from 100 K, the thermal stresses increase linearly. As mentioned above, the movement of dislocations induces the relaxation of these thermal stresses and the mechanical loss increases almost instantaneously due to the

coupling of the mechanical with the thermal stress field. The hysteresis in the curves is enhanced by annealing at 500 K. During the 10 min dwell time, the mechanical loss decreases due to the disappearance of transient damping and the microstructure evolution. Upon cooling, the thermal stresses, which are built up, have an opposite sign and as a consequence a temperature gap is needed to reach a stress level sufficient for moving the dislocations in the opposite direction and the mechanical loss starts to increase again. Upon cooling the mechanical loss decreases below 200 K, because the dislocation mobility decreases (Parrini 1995).

## 4.5 Modulus anomaly

The comparison of the different materials studied here shows that all samples containing long fibers present an anomaly in the shear modulus behavior, i.e. a change of slope in the temperature variation of the shear modulus or in some cases a modulus increase upon heating are observed between 300 and 400 K.

This modulus anomaly has been observed only in magnesium composites reinforced with fibers. It does not appear in unreinforced magnesium (fig. 4.5) or in magnesium reinforced with spherical particles (fig. 4.4). As reinforcing a metal with ceramic fibers increases the elastic modulus, one way to have a decrease of the modulus upon cooling would be a tension decrease in the fibers by matrix thermal contraction. However, calculations show that this effect is negligible in the case of internal friction measurements in a torsion pendulum.

In effect, the modulus anomaly can be interpreted as due to a dislocation effect. The mismatch of the thermal expansion coefficient between the matrix and the fibers gives rise to thermal stresses at the interface. In aluminum and magnesium matrix these thermal stresses are relaxed by dislocation motion. However, a modulus anomaly was never observed in aluminum matrix composites. The difference between aluminum and magnesium is the number of slip systems for dislocations. Magnesium has only three slip systems (the basal slip plane in the three  $\langle 110 \rangle$  directions) with respect to the 12 slip systems in aluminum. As a consequence, the ability of magnesium to relax the thermal stresses without cracks or interface de-cohesion is lower than the one of aluminum.

For modeling, let us consider the schematic drawing in fig. 4.14, where the primary slip plane of the hcp structure of magnesium (basal plane (001)) makes an angle  $\gamma$  with respect to the interface normal.

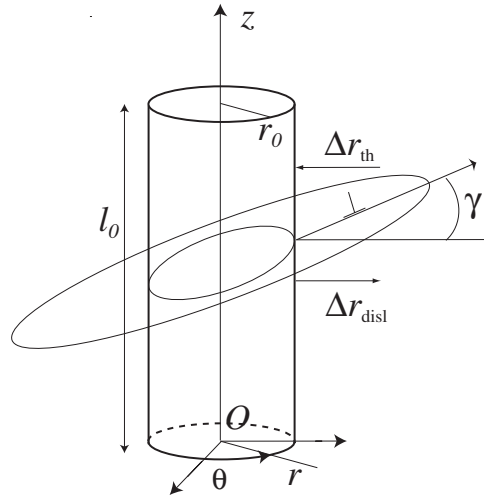


Fig. 4.14: Schematic drawing of a carbon fiber with indication of the dislocation slip plane, which makes an angle  $\gamma$  with the normal to the fiber matrix interface.

Due to a temperature change by an amount  $\Delta T$ , the difference of elongation in the longitudinal ( $z$ ) and in the radial ( $r$ ) direction with respect to a fiber will be respectively

$$\Delta z_{th} = \Delta \alpha \Delta T l_0 \quad (4.1)$$

$$\Delta r_{th} = \Delta \alpha \Delta T r_0 \quad (4.2)$$

where  $l_0$  and  $r_0$  are the length and radius of a reinforcing fiber, respectively, and  $\Delta \alpha$  is the difference in the thermal expansion coefficients. In the present model, we do not consider the anisotropy of thermal expansion of Mg.

Since the matrix has a higher thermal expansion coefficient than the fiber, the matrix contracts more than the fiber during cooling and is then under tensile stress along the  $z$  direction. The thermal misfit in the  $z$ -direction can be relieved by the emission of  $N_{disl}$  dislocations per length  $l_0$  of fiber. These dislocations glide on the basal plane of the magnesium matrix and one can write

$$\Delta z_{th} = \Delta \alpha \Delta T l_0 = N_{disl} b \sin \gamma \quad (4.3)$$

where  $b$  is the Burgers vector.

These  $N_{\text{disl}}$  dislocations will also produce a radial displacement of the matrix  $\Delta r_{\text{disl}}$

$$\Delta r_{\text{disl}} = N_{\text{disl}} b \cos \gamma \quad (4.4)$$

On the other hand, the thermal contraction of the matrix upon cooling also produces a radial displacement component  $\Delta r_{\text{th}}$  acting in the direction towards the interface, which in turns increases the bonding. This displacement due to thermal contraction is in the opposite direction with respect to the radial displacement by dislocation motion.

The interfacial bonding results from the competition between these two radial displacement components, and one can write a radial misfit as:

$$\Delta r_m = |\Delta r_{\text{disl}}| - |\Delta r_{\text{th}}| \quad (4.5)$$

If  $\Delta r_{\text{th}} = \Delta \alpha \Delta T r_0$ , and taking into account eq. (4.3) and (4.4), eq. (4.5) can be written as

$$\Delta r_m = \Delta \alpha |\Delta T| r_0 \left( \frac{l_0}{r_0 \tan \gamma} - 1 \right) \quad (4.6)$$

If upon cooling  $\Delta r_m > 0$  because of dislocation motion, interfacial de-bonding occurs and the shear modulus decreases. The dependence of this effect on the angle  $\gamma$  will be described in chapter 6. For the moment, we can consider that  $\gamma \approx 45^\circ$ , and then the effect occurs only when  $l_0 > r_0$ , i.e. in the case of reinforcements by fibers.

Effectively in fig. 4.4 one can see that the shear modulus of magnesium matrix composites reinforced with SiC particles, does not exhibit the shear modulus anomaly, because the shape factor for a sphere is  $\frac{l_0}{r_0} = 1$  and  $\gamma \approx 45^\circ$  so that  $\Delta r_m = 0$ .

On the other hand, the modulus anomaly is well observed in the Mg-Ni/CNT composite (fig. 4.3) even if the fiber concentration is low and fibers are short. This may be due to the high aspect ratio of the CNTs ( $l_0/r_0 \approx 1000$ ).

## 4.6 Conclusion

The mechanical loss spectra of magnesium matrix composites are characterized by a thermal hysteresis between heating and cooling, which may be interpreted as due to the inversion of the thermal stresses. Thermal stresses can be relaxed either by interface debonding or by crack propagation, which leads to degradation of the mechanical properties of the composites. They are also relaxed by the creation and motion of dislocations, which instead preserves the interfacial bonding. During the first cooling dislocations are created in order to relax the thermal stresses. However, between a fixed temperature interval, it is observed that (Mayencourt 1999) thermal stress is being relaxed by the same existing dislocations during heating and cooling cycles. Thermal stress relaxation in magnesium matrix composites gives rise to a modulus anomaly, which may be explained by interfacial debonding. This interfacial debonding would be due to the competition between a radial displacement away from the interface by dislocation motion under the effect of a stress field parallel to the fibers and the thermal contraction of the matrix.

The transient mechanical loss, which is superimposed on the isothermal equilibrium damping has been interpreted as due to dislocation motion controlled by a solid friction mechanism. In order to better analyze the damping mechanism, a complete study of the effect of the vibration amplitude on the mechanical loss (transient and isothermal damping) has been performed in the Mg/steel composites (Chapter 5).

The theoretical model by Mayencourt, which was developed to interpret the transient damping, justifies the whole mechanical loss behavior in magnesium composites. Two fit parameters  $C_1$  and  $C_2$  have been derived from the model, which account for the evolution of the mobile dislocation density and for the interfacial strength with respect to temperature, respectively. As these parameters qualify the interface, the effect of the matrix crystallographic orientation with respect to the interface on these parameters  $C_1$  and  $C_2$  has been studied in Mg/C composites (Chapter 6).





## Chapter 5: Study of dislocation damping due to solid friction

When dislocations experience solid friction drag, their motion is not thermally activated and the resulting mechanical loss spectrum is not shifted in temperature when the vibration frequency is changed. In the case of magnesium matrix composites, the transient mechanical loss obeys this behavior and can be interpreted as due to dislocation motion controlled by a solid friction mechanism. In the present case, TEM observations (Mayencourt 1999) have shown that dislocation motion was hysteretic. This type of motion of dislocations can be due to the pinning and un-pinning of the dislocations on localized obstacles. In the present chapter, the hysteretic motion of dislocations is studied in Mg/steel composites by using the Granato-Lücke theory.

### 5.1 Hysteretic motion of dislocations

Hysteretic motion can be obtained in the case of breakaway of dislocation segments from randomly segregated point defects under the action of an applied stress above an average critical stress level. This phenomenon has been first described in the model of Granato and Lücke (Granato 1956, Gremaud 2001). The mechanical loss  $\tan \phi$  for the breakaway of the dislocation segments from randomly segregated point defects can be calculated by eq. 2.31 and for point defects segregated following an exponential statistical distribution, the mechanical loss is calculated by eq. 2.32. These equations allow one to draw the Granato-Lücke plot of  $\ln(\tan \phi \cdot \sigma_0)$  as a function of  $1/\sigma_0$  (fig. 2.9b). From the slope and from the intercept of this plot with the stress axis, the critical stress for breakaway  $\sigma_{0cr}$  and the relaxation strength  $\Delta$  can be calculated, respectively.

Fig. 2.9a shows the schematic diagram of the mechanical loss as a function of  $\sigma_0$  (eq. 2.32). The evolution of the mechanical loss with the stress amplitude  $\sigma_0$  is composed of set of localized breakaway mechanisms (eq. 2.31), where the global trend shows first an increase of the damping with  $\sigma_0$ . The damping reaches a maximum for  $\sigma_0 = \sigma_{0cr}$  and then it decreases.

Previously, experimental results have been obtained only for the part where the mechanical loss increases with the stress amplitude  $\sigma_0$  (Schwarz 1983).

In this work, a model composite material constituted of Mg reinforced with unidirectional stainless steel fibers is investigated (fig. 3.7 and 3.8). It is demonstrated that the mechanical loss is controlled by hysteretic motion of dislocations. This mechanism is not thermally activated. Therefore, there is a clear advantage in using these composites since high damping capacity can be maintained over a large range of frequencies.

## 5.2 Analysis of the mechanical loss spectrum of Mg/steel

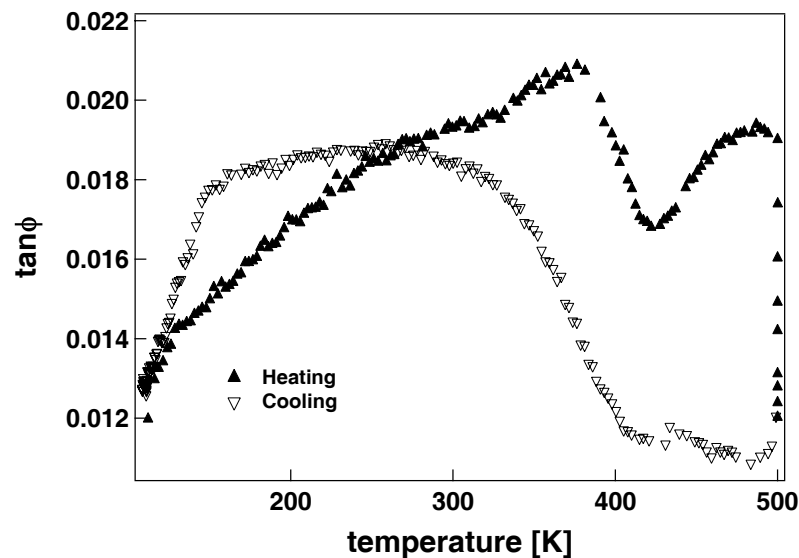


Fig. 5.1: Mechanical loss  $\tan\phi$  as a function of temperature for cooling and heating at a constant heating/cooling rate of  $\dot{T} = 2$  K/min, a stress amplitude  $\sigma_0 = 0.9$  MPa and an excitation frequency of 0.5 Hz.

The mechanical loss spectrum of Mg/steel composites, which was already described in ch. 4, is reported in fig. 5.1. The spectrum is characterized by a marked thermal hysteresis, which accounts for the thermal stress inversion at the cycle ends. Thermal stresses are then responsible for the transient part of the total mechanical loss. Also the method of analysis presented in ch. 4 has been applied in the present case. First, it has been verified that in these model composites, which contain reinforcements of millimeter dimensions, the mechanical loss exhibits also a transient component as in the case of carbon fiber reinforcements. Indeed, the mechanical loss depends strongly on the vibration frequency both upon heating (fig. 5.2a)

and upon cooling (fig. 5.2b). In fact, it decreases with increasing the frequency as in the case of the carbon fibers (ch. 4).

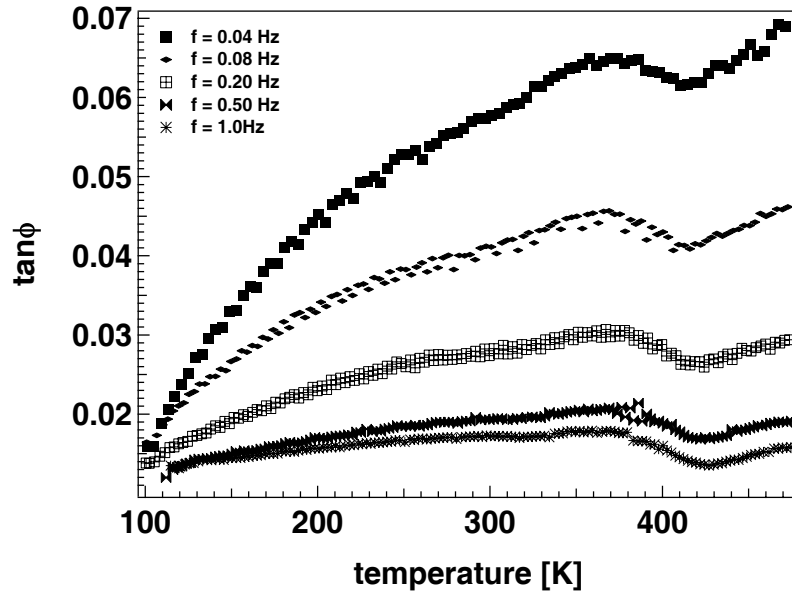


Fig. 5.2a: Mechanical loss  $\tan\phi$  as a function of temperature during heating at  $\dot{T} = 2$  K/min and a stress amplitude of  $\sigma_0 = 0.9$  MPa. The excitation frequency has been varied from 0.04 Hz to 1.0 Hz.

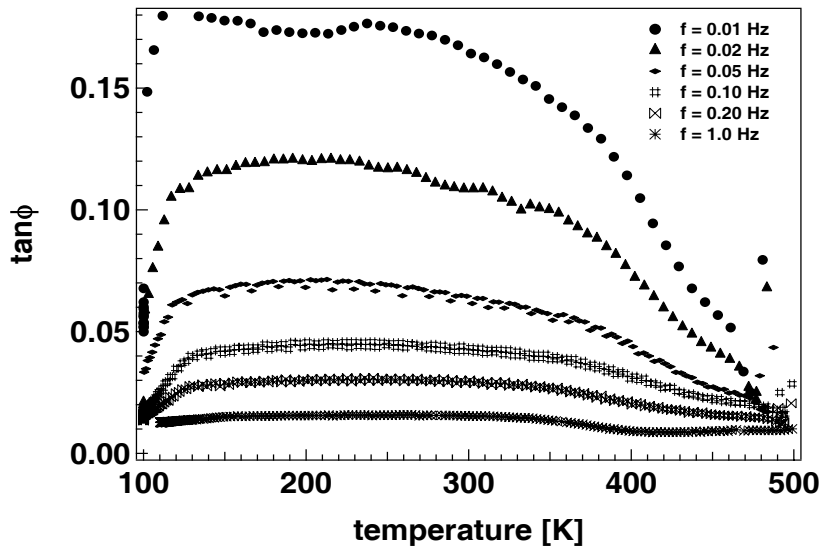


Fig. 5.2b: Mechanical loss  $\tan\phi$  as a function of temperature during cooling at  $\dot{T} = 2$  K/min and a stress amplitude of  $\sigma_0 = 0.9$  MPa. The excitation frequency has been varied from 0.01 Hz to 1.0 Hz.

Moreover, a marked increase of the mechanical loss with increasing  $\dot{T}$  is observed both upon heating (fig. 5.3a) and upon cooling (fig. 5.3b).

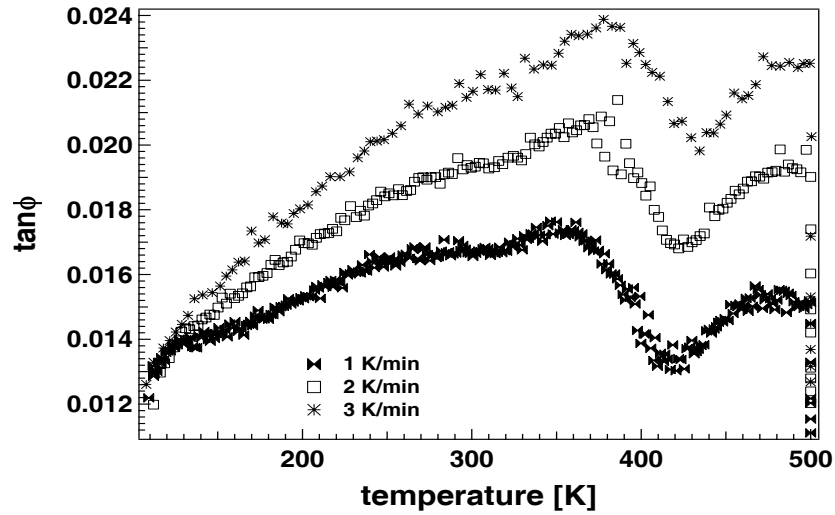


Fig. 5.3a: Mechanical loss  $\tan\phi$  as a function of temperature for different heating/cooling rates  $\dot{T}$  at a constant excitation frequency 0.5 Hz and a stress amplitude  $\sigma_0 = 0.9$  MPa during heating.

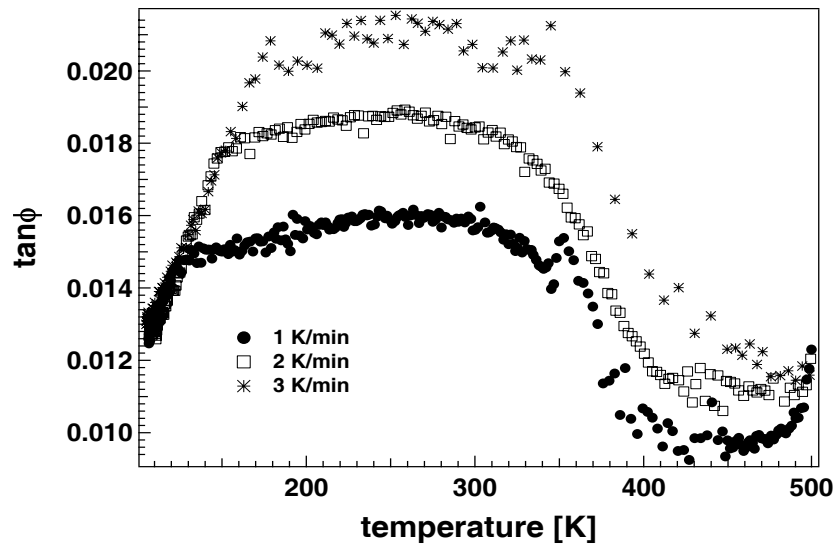


Fig. 5.3b: Mechanical loss  $\tan\phi$  as a function of temperature for different heating/cooling rates  $\dot{T}$  at a constant excitation frequency 0.5 Hz and a stress amplitude  $\sigma_0 = 0.9$  MPa during cooling.

The variations of the mechanical loss spectrum with  $\omega$  and  $\dot{T}$  show that transient damping is important. In order to extract the transient component from the total mechanical loss, measurements were performed as in the case of Mg/C composites (fig. 4.8), both during heating and cooling at a constant rate  $\dot{T} = 3$  K/min and a frequency of 0.5 Hz with annealing of 60 minutes at 25 K temperature intervals. The stress amplitude was kept constant at 0.9 MPa. The results are reported in fig. 5.4. Again, strong decreases of the mechanical loss with increasing time are observed during each isothermal annealing both upon heating (fig. 5.4a) and upon cooling (fig. 5.4b).

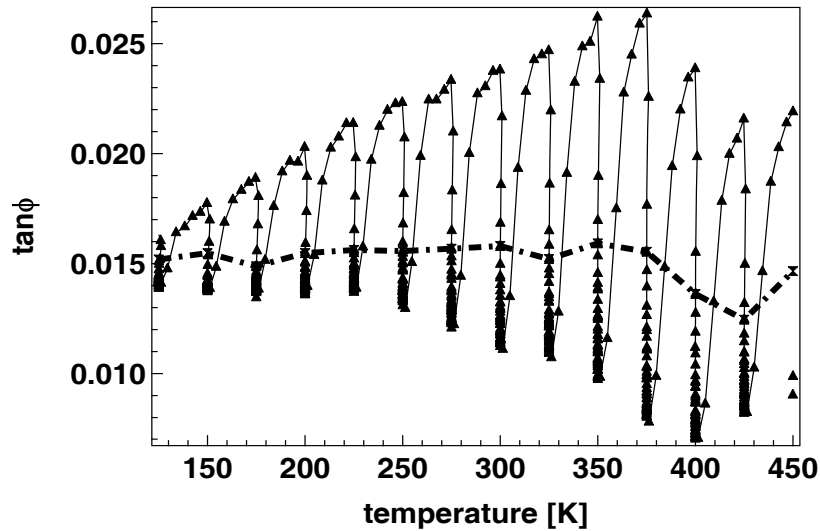


Fig. 5.4a: Mechanical loss spectrum as a function of temperature during heating. The sample is annealed for 60 minutes at 25 K temperature intervals. The dashed line indicates the transition between transient mechanical loss and microstructure evolution.

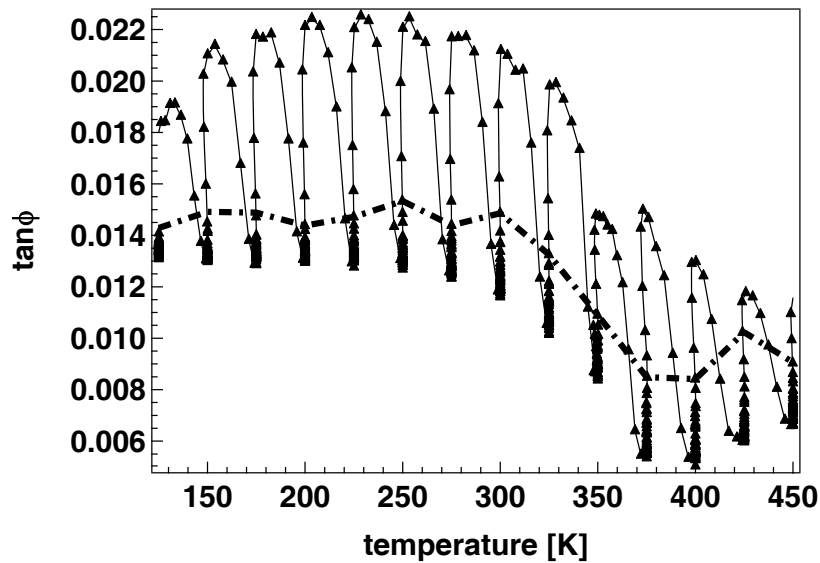


Fig. 5.4b: Mechanical loss spectrum as a function of temperature during cooling. The sample is annealed for 60 minutes at 25 K temperature intervals. The dashed line indicates the transition between transient mechanical loss and microstructure evolution.

By reporting the mechanical loss as a function of time during isothermal annealing, one observes again that the decrease is composed of two regimes (fig. 5.5): a first rapid decrease, almost linear, which can be associated with the disappearance of the transient component when  $\dot{T} = 0$ , and a second stage of exponential decrease, which would be associated to some microstructure relaxation. The transition between the two regimes is well marked and has

been chosen to discriminate the transient component from the total mechanical loss. The transition points are plotted with dashed lines in fig. 5.4a and fig. 5.4b.

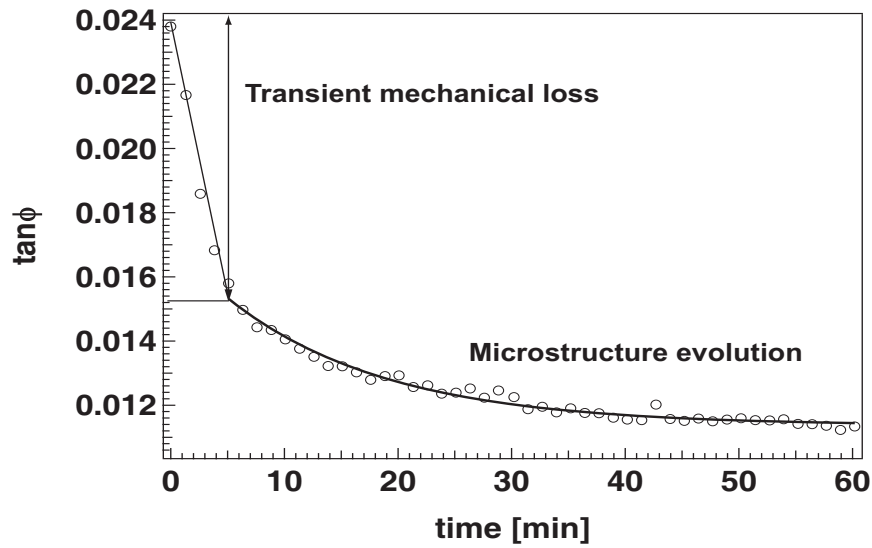


Fig. 5.5: Mechanical loss  $\tan\phi$  as a function of time at 300 K at a constant stress amplitude of 0.9 MPa.

## 5.3 Effects of the vibration amplitude

### 5.3.1 Intrinsic damping

Fig. 5.6 shows the mechanical loss as measured in isothermal condition at 400 K as a function of the stress amplitude  $\sigma_0$ . The results were obtained after stopping the heating for 50 minutes, which corresponds to an isothermal equilibrium condition. We are therefore in the stage of microstructure evolution of fig. 5.5. The mechanical loss increases first with  $\sigma_0$ , showing a maximum at around 0.2 MPa and then it decreases.

The solid curve in fig. 5.6 corresponds to the fitting obtained by using eq. 2.32:

$$\tan\phi = \Delta \frac{1}{\pi} \left( \frac{\sigma_{0cr}}{\sigma_0} \right) \exp \left( - \frac{\sigma_{0cr}}{\sigma_0} \right)$$

We have obtained to the best of our knowledge for the first time, the complete evolution of the mechanical loss as a function of the stress amplitude  $\sigma_0$ . The mechanical loss first

increases with the stress amplitude with a maximum at  $\sigma_0 = \sigma_{0cr} \approx 0.2$  MPa, and then it decreases.

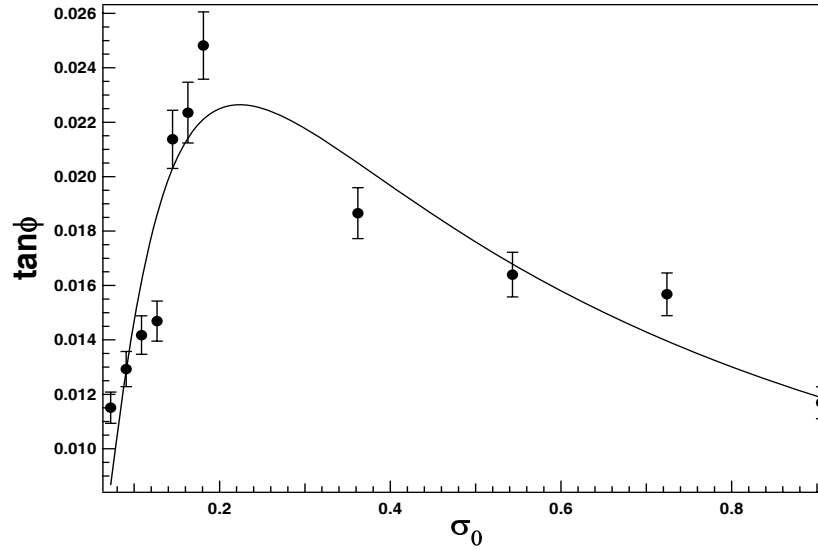


Fig. 5.6: Mechanical loss  $\tan\phi$  measured at 400 K as a function of applied stress amplitude  $\sigma_0$ .

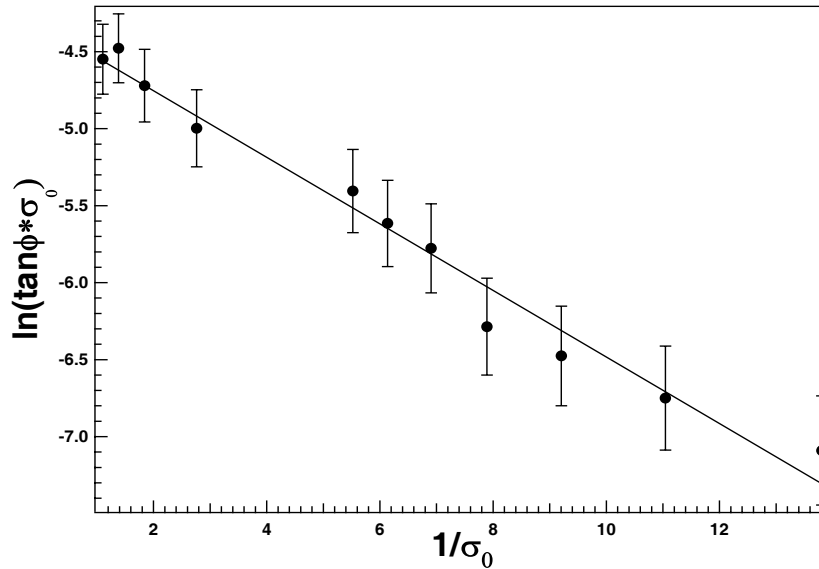


Fig. 5.7: Granato-Lücke plot of amplitude dependent damping measured at 400 K.

Fig. 5.7 shows the experimental points of fig. 5.6, which have been used to draw the so-called Granato-Lücke plot, i.e., the plot of  $\ln(\tan\phi \cdot \sigma_0)$  as a function of  $1/\sigma_0$ . The experimental points show a linear trend, as expected from the Granato-Lücke model. In other words, the results account for a mechanism of dislocation breakaway from segregated point defects.

### 5.3.2 Transient damping

The transient mechanical loss  $\tan\phi_{Tr}$  has been obtained by subtracting the background due to microstructure evolution and intrinsic damping from total damping (fig. 5.4). According to eqs. 2.47-2.48, the transient mechanical loss should depend not only on  $\omega$  and  $\dot{T}$ , but also on the stress amplitude  $\sigma_0$ .

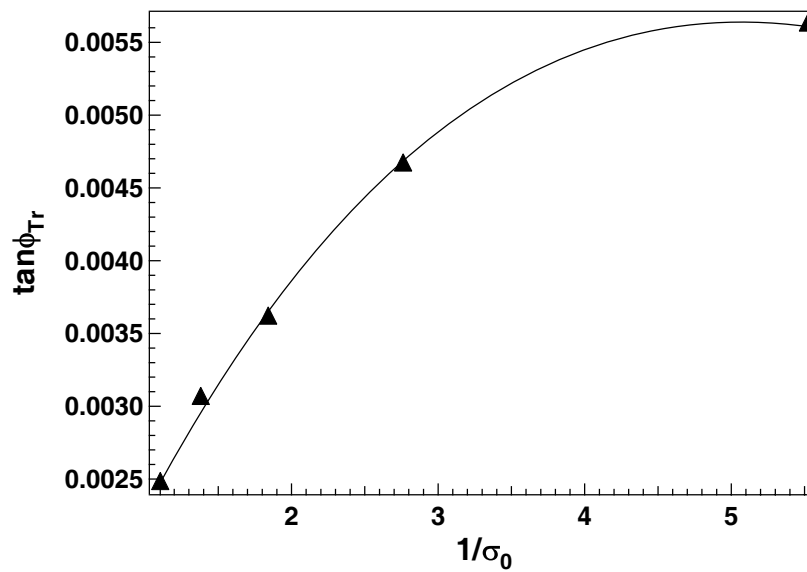


Fig. 5.8: Transient mechanical loss  $\tan\phi_{Tr}$  as a function of  $\frac{1}{\sigma_0}$  measure at 400 K.

The vibration amplitude dependence is shown fig. 5.8, where the experimental points appear to obey well the Mayencourt's model of dislocations that experience a solid friction drag. Indeed, the solid line in fig. 5.8 has been derived from the fit using eq. 2.47.

## 5.4 Discussion

Fig. 5.5 shows that the microstructure is time dependent. However, by reporting the exponential decrease of the mechanical loss, which accounts for the microstructure relaxation, as a function of the annealing temperature, no time shift was observed. As a consequence, the microstructure relaxation is not thermally activated. This is in agreement with the fact that the damping mechanism is due to the dislocation breakaway from segregated atoms. As shown by Granato-Lücke, this mechanism must depend on the excitation amplitude. Fig. 5.6 describes such a behavior. The mechanical loss is obtained



after annealing at 400 K for 50 minutes, which corresponds to an almost stable microstructure (as shown in fig. 5.5). The stress amplitudes were varied from 0.018 to 0.9 MPa. Indeed, a complete evolution of the mechanical loss as a function of stress amplitude  $\sigma_0$  is obtained in agreement with eq. 2.32. As pure magnesium was used as the metallic matrix, a small number of defects are available, and consequently the distribution of the defects on dislocation segments is relatively narrow. For this reason, the mechanical loss increases sharply with the applied stress amplitude  $\sigma_0$ , reaching a maximum around  $\sigma_{0cr} = 0.2$  MPa, and then it decreases. The linear Granato-Lücke plot shown in fig. 5.7 provides a further evidence of this model. The critical stress for breakaway  $\sigma_{0cr}$  in the case of microstructure evolution is obtained from the Granato-Lücke plot, which appears to be 0.216 MPa. The present material provides an efficient damping mechanism with a low threshold stress. As damping is not thermally activated, it can be maintained over wide temperature and frequency ranges.

Previous results concerning the mechanical loss as a function of stress amplitude were obtained for values  $\sigma_0 < \sigma_{0cr}$ , where the mechanical loss increases for increasing the stress amplitude (Schwartz 1983). It might be argued that the threshold stress for hysteretic damping is rather low and that a similar behavior should be observed in pure magnesium. In fact, in some experiments not reported here we have observed that in pure magnesium only an increasing mechanical loss as a function of  $\sigma_0$  was observed. This is the usual behavior observed in the case of hysteretic damping. The stress field is not homogeneous in the composite. The residual stresses around the fibers bias the applied stress. So, even if the stress applied in mechanical spectroscopy experiments is very small, it is sufficient to overcome the critical stress for breakaway  $\sigma_{0cr}$ . This may be the reason for which the complete curve for hysteretic damping is observed only in the composite material.

## 5.5 Conclusion

The transient damping due to thermal stress relaxation may be interpreted by the hysteretic motion of dislocations. The model by Mayencourt justifies the whole mechanical loss behavior. The amplitude dependency of the mechanical loss and the Granato-Lücke plot confirm that the microstructure evolution is controlled by the breakaway of dislocation segments from randomly segregated point defects (hysteretic damping). Hysteretic damping

is very interesting in the development of high damping materials, because in this case the high damping capacity can be maintained over a wide frequency range.

## Chapter 6: Crystallographic orientation of the matrix and interface quality

Magnesium has a hcp structure, where the primary glide plane is the basal plane (001). In the case of magnesium matrix, interface thermal stresses are relaxed by dislocation motion in the basal plane (001) of the hexagonal structure. Dislocations are pinned by impurity atoms and when they experience a stress higher than the pinning stress, dislocations can breakaway and glide in the matrix. Thus, by orienting the glide plane one can have a control on the gliding of dislocations in order to relax these stresses. In this chapter, the influence of the orientation of the basal plane with respect to the matrix-fiber interface on the gliding of the dislocations is described.

### 6.1 Effect of matrix orientation on the mechanical loss spectra

As mentioned in chapter 3, specimen composed of a magnesium matrix reinforced with long carbon fiber composites were uni-directionally solidified by using the Bridgman technique. The crystallographic orientation of the magnesium matrix was evidenced by Bragg Brentano XRD analysis and the different samples were selected according to the orientation of the normal to the basal plane with respect to the matrix-fiber interface (see nomenclature in § 3.6).

Fig. 6.1 shows the typical mechanical loss spectra of three specimens differing from each other by the orientation of the matrix basal plane, measured during a heating and cooling cycle at  $\dot{T} = 2$  K/min. The spectra are characterized by a thermal hysteresis. The mechanical loss spectra for Mg/C<sub>90°</sub> and Mg/C<sub>45°</sub> (fig. 6.1a and 6.1b) are almost identical, while the damping level differs. The composite Mg/C<sub>90°</sub> shows the minimum damping, followed by Mg/C<sub>45°</sub>. The damping level in the composite Mg/C<sub>0°</sub> is almost 3 and 7 times higher than that of the composites Mg/C<sub>45°</sub> and Mg/C<sub>0°</sub>, respectively. During heating, the mechanical loss increases first, and then during the annealing at 500 K (10 minutes), the mechanical loss decreases. Upon cooling, the mechanical loss increases continuously up to 200 K and then it decreases. However, for the sample Mg/C<sub>0°</sub> in fig. 6.1c, upon cooling the mechanical loss

increases up to 400 K and then it almost saturates and starts to decrease below 120 K. The spectrum shows a reversible trend during heating and cooling cycles.

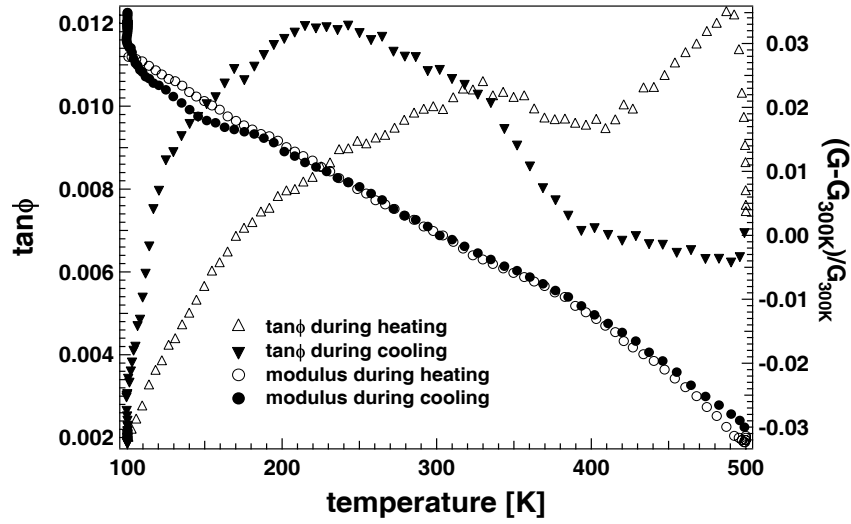


Fig. 6.1a: Mechanical loss  $\tan\phi$  and relative elastic shear modulus as a function of temperature for cooling and heating at a temperature rate  $\dot{T} = 2$  K/min and  $\omega = 0.1$  Hz in Mg/C<sub>90°</sub>.

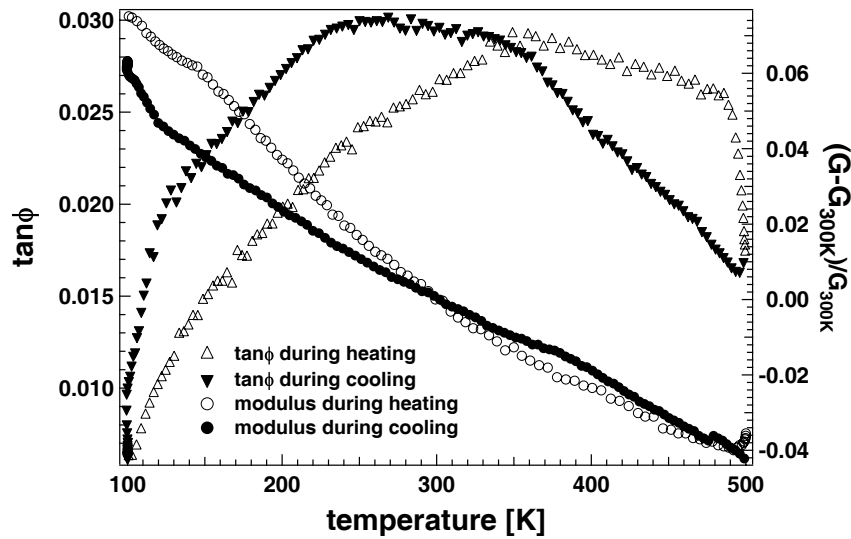


Fig. 6.1b: Mechanical loss  $\tan\phi$  and relative elastic shear modulus as a function of temperature for cooling and heating at a temperature rate  $\dot{T} = 2$  K/min and  $\omega = 0.2$  Hz in Mg/C<sub>45°</sub>.

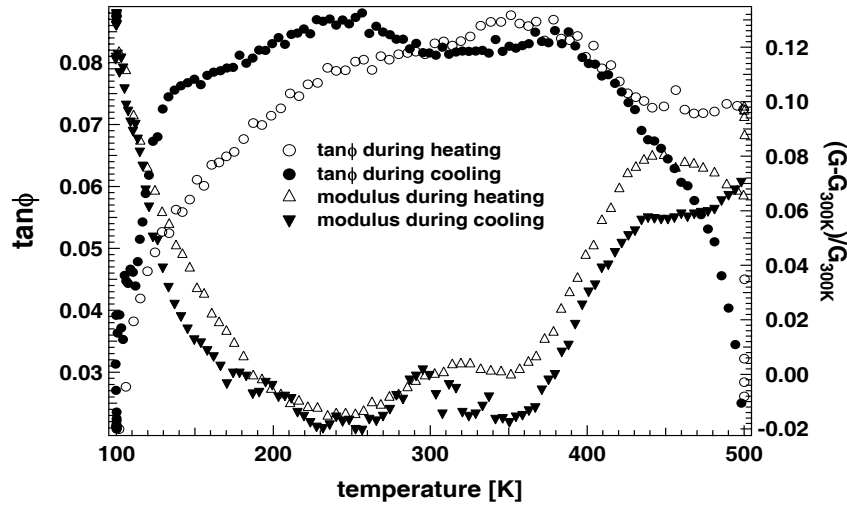


Fig. 6.1c: Mechanical loss  $\tan\phi$  and relative elastic shear modulus as a function of temperature for cooling and heating at a temperature rate  $\dot{T} = 2$  K/min and  $\omega = 0.04$  Hz in Mg/C<sub>0°</sub>.

Fig. 6.1 also shows the normalized shear modulus during a heating and cooling cycle. Fig. 6.1a shows that the shear modulus increases during cooling and decreases during heating. An anomalous behavior of the modulus is observed for the samples Mg/C<sub>45°</sub> (fig.6.1b) between 350 and 425 K, where a variation of the curve slope is observed. In Mg/C<sub>0°</sub> (fig. 6.1c) the modulus behavior is abnormal between 200 and 450 K, where it decreases during cooling and increases during heating.

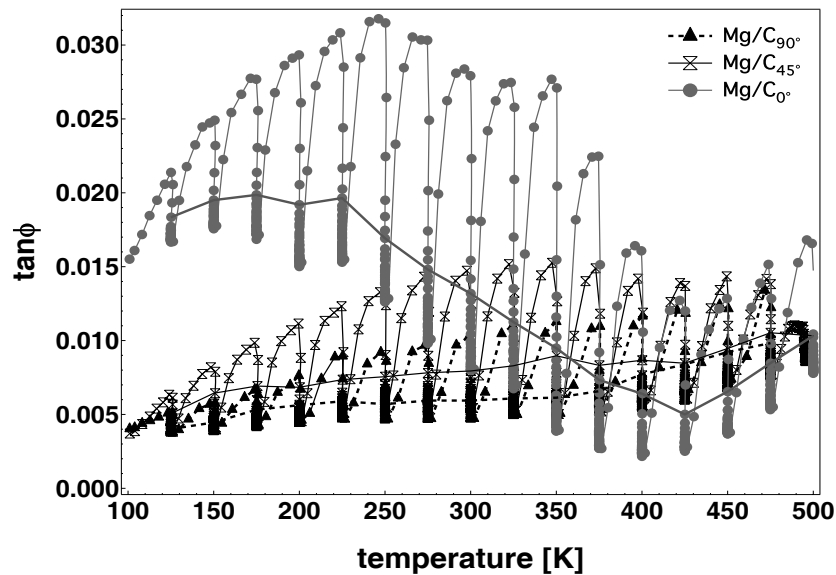


Fig. 6.2: Mechanical loss  $\tan\phi$  as a function of temperature. The solid lines show the point of transition between the transient damping and the microstructure evolution damping.

Fig. 6.2 shows the mechanical loss spectra of the three composites measured during heating and cooling at a constant heating rate of  $\dot{T} = 3$  K/min and a frequency of 0.5 Hz with annealing of 60 minutes at 25 K temperature intervals. It is observed that the damping is the highest in the composite Mg/C<sub>0°</sub>, followed by Mg/C<sub>45°</sub>, while the composite Mg/C<sub>90°</sub> has the lowest value. The solid lines correspond to the limit between the true transient damping and the microstructure evolution. This discrimination procedure has been the same as presented in chapter 4.

The dependency of the transient damping on heating/cooling rate  $\dot{T}$  and on the circular excitation frequency  $\omega$  has been studied for all of the three matrix orientations. Figs. 6.3 and 6.4 give as an example the results obtained for Mg/C<sub>90°</sub>. Damping increases with  $\dot{T}$  increase and decreases with the increase of  $\omega$ .

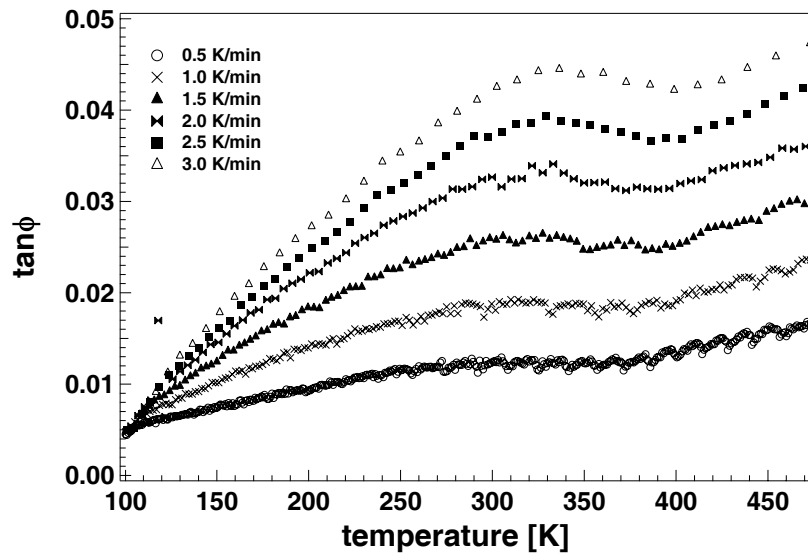


Fig. 6.3a: Mechanical loss  $\tan\phi$  as a function of temperature for different heating rates  $\dot{T}$  at a constant excitation frequency of 0.05 Hz during heating in the composite Mg/C<sub>90°</sub>.

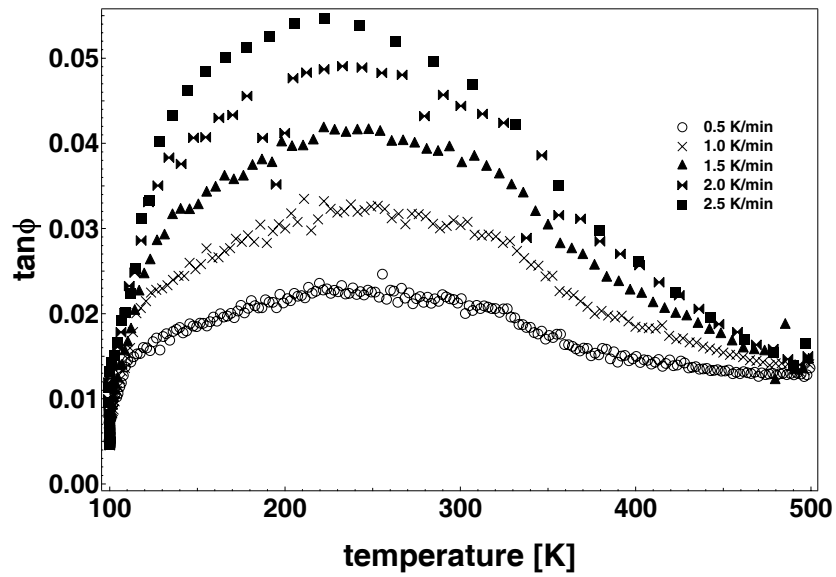


Fig. 6.3b: Mechanical loss  $\tan\phi$  as a function of temperature for different cooling rates  $\dot{T}$  at a constant excitation frequency of 0.05 Hz during cooling in the composite Mg/C<sub>90°</sub>.

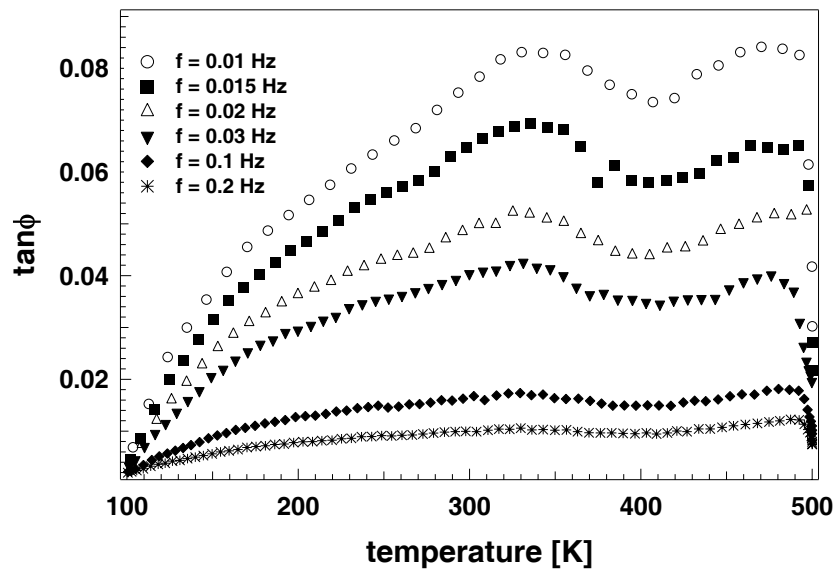


Fig. 6.4a: Mechanical loss  $\tan\phi$  as a function of temperature for different excitation frequencies at a constant temperature rate  $\dot{T} = 2$  K/min during heating in the composite Mg/C<sub>90°</sub>.

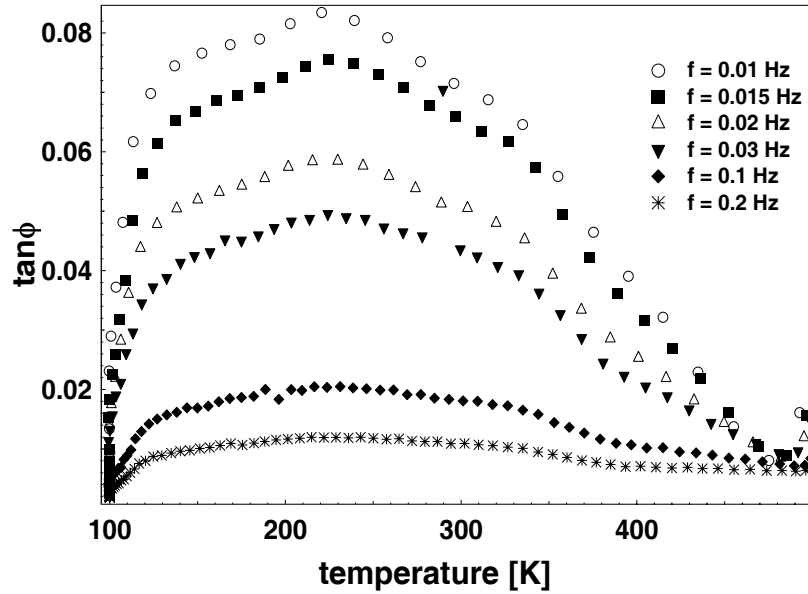


Fig. 6.4b: Mechanical loss  $\tan\phi$  as a function of temperature for different excitation frequencies at a constant temperature rate  $\dot{T} = 2$  K/min during cooling in the composite Mg/C<sub>90°</sub>.

## 6.2 Spectrum analysis

### 6.2.1. Damping level as a function of matrix orientation

It is observed in fig. 6.1 and fig. 6.2 that the damping is the highest in the composite Mg/C<sub>0°</sub> followed by Mg/C<sub>45°</sub> and Mg/C<sub>90°</sub> respectively. This effect can be explained by the model for dislocation glide illustrated in fig. 6.5.

Since the matrix has a higher thermal expansion coefficient than the fiber, during cooling the matrix contracts more than the fibers and is under tensile stress. The thermal misfit in the z-direction can be relieved by the emission of dislocations gliding on the basal plane of the magnesium hcp structure (001). This basal plane makes an angle  $\gamma$  with respect to the interface normal (fig. 6.5). The dislocation loop in fig. 6.5 experiences the stress field, which results from the interface thermal stresses and the applied shear stress in the torsion pendulum. The force  $\vec{F}$ , which acts on one point of the dislocation loop, is calculated by using the so called Peach and Koehler equation:

$$\vec{F} = \vec{b} \cdot \vec{\sigma} \wedge \vec{t} \quad (6.1)$$



where  $\vec{\sigma}$  is the stress tensor,  $\vec{b}$  and  $\vec{t}$  are the Burgers vector and the tangential unit vector of the dislocation, respectively.

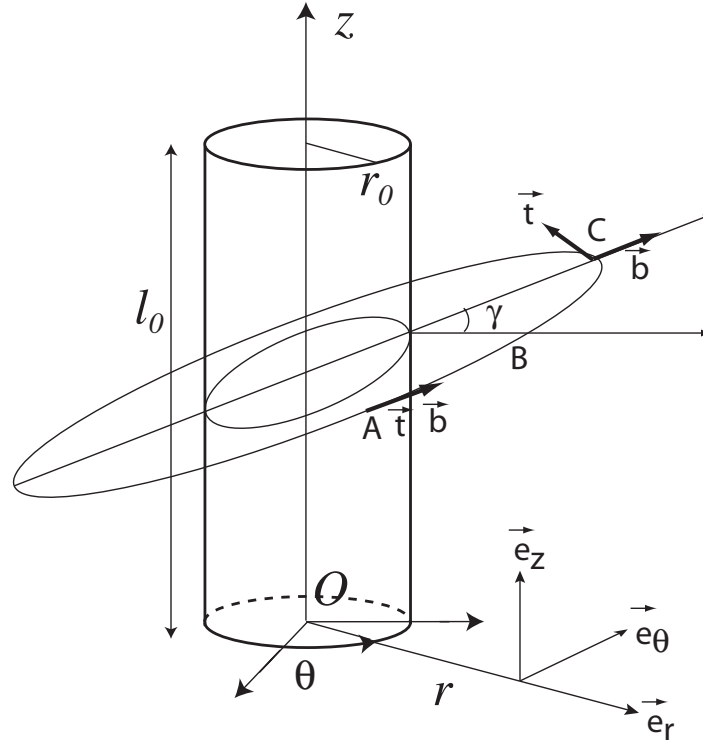


Fig. 6.5: Schematic drawing of a carbon fiber with a dislocation loop gliding on the basal (primary) slip plane of the magnesium matrix. The glide plane makes an angle  $\gamma$  with the normal to the fiber matrix interface.

The Burgers vector  $\vec{b}$ , the tangential unit vector  $\vec{t}$  and the stress tensor  $\vec{\sigma}$  can be expressed in a system of cylindrical coordinates  $(r, \theta, z)$  as

$$\vec{b} = (b \cos \gamma \sin \theta \quad b \cos \gamma \cos \theta \quad b \sin \gamma) \quad (6.2)$$

$$\vec{t} = \begin{pmatrix} 0 & t_\theta & t_z \end{pmatrix} \quad (6.3)$$

Here we suppose that the dislocation loop is almost circular and therefore one can write  $t_r \approx 0$  along the glide plane.

$$\vec{\sigma} = \begin{vmatrix} \sigma_{rr} & 0 & 0 \\ 0 & \sigma_{\theta\theta} & \sigma_{\theta z} \\ 0 & \sigma_{z\theta} & \sigma_{zz} \end{vmatrix} \quad (6.4)$$

The components of the stress tensor are  $\sigma_{rr}, \sigma_{\theta\theta}$  and  $\sigma_{zz}$  for the thermal stresses due to the difference in thermal dilatation between the fiber and the matrix,  $\sigma_{\theta z}$  and  $\sigma_{z\theta}$  are the components of the applied shear stress.

The dislocation loop in fig. 6.7 exhibits a pure screw character at point A, a mixed screw–edge character at point B and a pure edge character at point C

Using eq. 6.2 and eq. 6.3, the Peach and Koehler force (eq. 6.1) can be calculated as

$$\vec{F} = \vec{b} \cdot \vec{\sigma} \wedge \vec{t} = \begin{vmatrix} \vec{e}_r & \vec{e}_\theta & \vec{e}_z \\ b_r \sigma_{rr} & b_\theta \sigma_{\theta\theta} + b_z \sigma_{z\theta} & b_\theta \sigma_{\theta z} + b_z \sigma_{zz} \\ 0 & t_\theta & t_z \end{vmatrix}$$

which gives

$$\vec{F} = [(b_\theta \sigma_{\theta\theta} + b_z \sigma_{z\theta})t_z - (b_\theta \sigma_{\theta z} + b_z \sigma_{zz})t_\theta] \cdot \vec{e}_r - (b_r \sigma_{rr} t_z) \cdot \vec{e}_\theta + (b_r \sigma_{rr} t_\theta) \cdot \vec{e}_z \quad (6.5)$$

At point A ( $\theta = 0^\circ$ ), where the dislocation loop shows a pure screw character, eq. 6.2 and eq. 6.3 can be written as

$$\vec{b} = (0 \quad b \cos \gamma \quad b \sin \gamma) \quad (6.6)$$

$$\vec{t} = (0 \quad \cos \gamma \quad \sin \gamma) \quad (6.7)$$

Then, from eq. 6.5 the Peach and Koehler force at point A can be calculated as

$$\vec{F}_A = [b \cdot (\sigma_{\theta\theta} - \sigma_{zz}) \cdot \cos \gamma \sin \gamma + b \cdot \sigma_{\theta z} \cdot (\sin^2 \gamma - \cos^2 \gamma)] \cdot \vec{e}_r \quad (6.8)$$

The thermal stress contribution is maximum for  $\gamma \approx 45^\circ$ , but the contribution of the applied shear stress is zero. For  $\gamma \approx 0^\circ$  and  $90^\circ$  only the applied stress is present, while the component of thermal stress is zero. However, for  $\gamma \approx 90^\circ$  it is not physically possible for the dislocation to glide.

At point B ( $\theta = 45^\circ$ ), where the dislocation loop shows a mixed character, eq. 6.2 and eq. 6.3 can be written as

$$\vec{b} = \begin{pmatrix} \frac{b}{\sqrt{2}} \cos \gamma & \frac{b}{\sqrt{2}} \cos \gamma & b \sin \gamma \end{pmatrix} \quad (6.9)$$

$$\vec{t} = \begin{pmatrix} 0 & t_\theta & t_z \end{pmatrix} \quad (6.10)$$

We can estimate the force  $\vec{F}$  acting on the dislocation at point B, by using eq. 6.1

$$\begin{aligned} \vec{F}_B = & \left[ \left( \frac{b}{\sqrt{2}} \cdot \sigma_{\theta\theta} \cdot \cos \gamma + b \cdot \sigma_{z\theta} \cdot \sin \gamma \right) \cdot t_z - \left( \frac{b}{\sqrt{2}} \cdot \sigma_{\theta z} \cdot \cos \gamma + b \cdot \sigma_{zz} \cdot \sin \gamma \right) \cdot t_\theta \right] \cdot \vec{e}_r \\ & + \left( \frac{b}{\sqrt{2}} \cdot \sigma_{rr} \cdot \cos \gamma \cdot t_z \right) \cdot \vec{e}_z - \left( \frac{b}{\sqrt{2}} \cdot \sigma_{rr} \cdot \cos \gamma \cdot t_\theta \right) \cdot \vec{e}_\theta \end{aligned}$$

Assuming for simplification that the vector  $\vec{t}$  is almost parallel to  $\vec{e}_\theta$  at this point, i.e.  $t_z \ll t_\theta$ , which gives the Peach and Koehler force in the radial direction:

$$F_{B_r} = - \left( \frac{b}{\sqrt{2}} \cdot \sigma_{\theta z} \cdot \cos \gamma + b \cdot \sigma_{zz} \cdot \sin \gamma \right) \quad (6.11)$$

Coupling between the thermal stresses and applied shear stress arises on the glide plane of the dislocation, which experiences a radial force with respect to the fiber. It appears that the best coupling would be achieved for an angle  $\gamma = 45^\circ$ .

At point C, where the dislocation loop shows a pure edge character, the force  $\vec{F}$  can be estimated as

$$\vec{F}_C = b \cdot \cos \gamma \cdot \sigma_{rr} \cdot \vec{e}_z - b \cdot \sin \gamma \cdot \sigma_{zz} \cdot \vec{e}_r \quad (6.12)$$

For different values of  $\gamma$ , the Peach and Koehler force can be computed as

$$\begin{aligned}
\gamma = 0^\circ &\rightarrow \vec{F}_C = b \cdot \sigma_{rr} \cdot \vec{e}_z \\
\gamma = 45^\circ &\rightarrow \vec{F}_C = \frac{b}{\sqrt{2}} \cdot (\sigma_{rr} \cdot \vec{e}_z - \sigma_{zz} \cdot \vec{e}_r) \\
\gamma = 90^\circ &\rightarrow \vec{F}_C = -b \cdot \sigma_{zz} \cdot \vec{e}_r
\end{aligned} \tag{6.13}$$

Eq. 6.13 shows that at point C, only the thermal stress component is acting on the dislocation loop and then no coupling is active at this point between the applied stress and the thermal stress. For  $\gamma = 90^\circ$ , as only the z-component of the thermal stress is acting, the dislocation cannot glide on the primary glide plane. It has to climb. This would be obviously possible only at high temperatures. For  $\gamma = 0^\circ$ , only the radial component of the thermal stress is acting along  $\vec{e}_z$ . Then the dislocation can only climb out of the glide plane.

Taking into account eqs. 6.8, 6.11 and 6.12, which show that the resolved shear stress in the dislocation glide plane is a function of  $\cos \gamma$ , we can correct eq. 2.47 as follows (the complete analysis of the model is shown in the appendix):

$$\tan \phi_{Tr} = 2C_1 C_2 \cdot \cos \gamma \cdot \left( \frac{\dot{T}}{\omega} \right)^{\frac{1 - \frac{\pi}{2} C_2 \frac{\dot{T}}{\omega \cos \gamma}}{1 + \frac{\pi}{2} C_2 \frac{\dot{T}}{\omega \cos \gamma}}} \tag{6.14}$$

The transient mechanical loss  $\tan \phi_{Tr}$  depends on  $\cos \gamma$ . In a logical way, the mechanical loss is the highest in the composite Mg/C<sub>0°</sub> with a mean value of  $\gamma \approx 0^\circ$ . In the composite Mg/C<sub>45°</sub> where the basal plane is at an angle  $\gamma \cong 45^\circ$  with respect to the matrix-fiber interface, the damping is lower, while the composite Mg/C<sub>90°</sub>, with a mean value of  $\gamma \approx 90^\circ$ , exhibits the lowest damping. It is evident from the X-ray diffraction spectrum that the sample Mg/C<sub>90°</sub> was not perfectly oriented and that the mean value  $\gamma \approx 90^\circ$  for the angle between the basal plane and the matrix-fiber interface may be overestimated. However, damping in Mg/C<sub>90°</sub> is almost 7 times lower than in Mg/C<sub>0°</sub>.

In the composite Mg/C<sub>90°</sub> (fig.6.1a), the shear modulus shows a normal behavior, i.e., it continuously decreases during heating. The composites Mg/C<sub>45°</sub> and Mg/C<sub>0°</sub> instead exhibit an anomalous behavior in the thermal evolution of the shear modulus. Starting at about 350K, the slope of the shear modulus changes both during heating and cooling. During heating, the

matrix is expanding more than the fiber and the shear modulus should decrease. In fig. 6.1b and 6.1c it is observed that the shear modulus decreases first when the temperature is increased up to 350 K, and then there is a small change of slope in the sample Mg/C<sub>45°</sub>, while in Mg/C<sub>0°</sub> the increase in the slope is more dramatic. This trend is reproduced upon cooling.

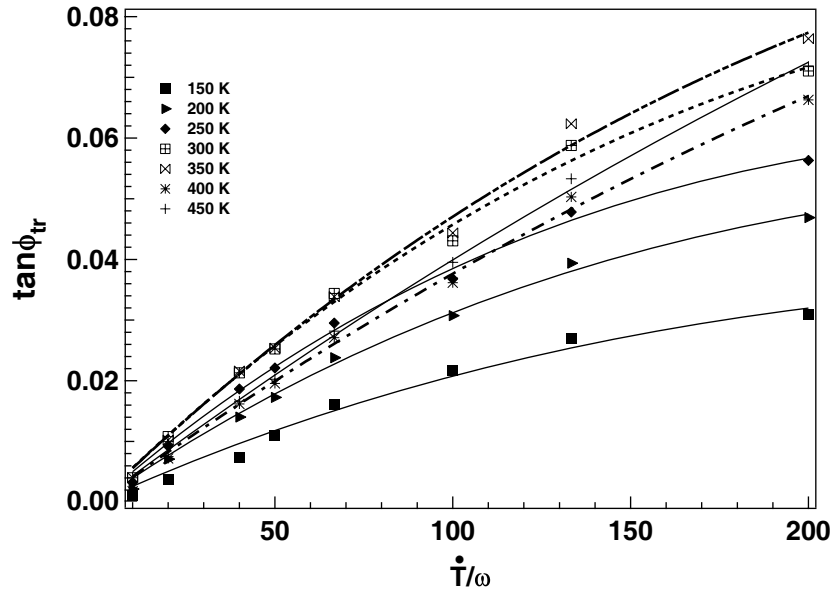


Fig. 6.6: Transient mechanical loss  $\tan\phi_{tr}$  as a function of  $\dot{T}/\omega$  for different temperatures during heating in the composite Mg/C<sub>90°</sub>. Solid lines correspond to fitting curves at different temperatures.

### 6.2.2. $C_1$ and $C_2$ parameters as a function of matrix orientation

Figure 6.6 shows that the transient mechanical loss is a nonlinear function of  $\dot{T}/\omega$ . The good fit between the experimental results and the theoretical model of Mayencourt and Schaller described by eq. 2.47 confirms the validity of the model where the relaxation phenomenon is dominated by dislocation gliding controlled by pinning and depinning from immobile point objects. The parameters  $C_1$  and  $C_2$  are obtained from fitting the experimental data with the theoretical model curve. The evolution of  $C_1$  and  $C_2$  as a function of temperature is shown in fig. 6.7 and fig. 6.8 for all of the three matrix orientations both upon heating and upon cooling.

Fig. 6.7 shows the evolution of the fitting parameter  $C_1$  with respect to the temperature during heating and cooling. Here again a marked hysteresis is observed between the values obtained

upon heating and cooling.  $C_I$  is sensitive to the mobile dislocation density  $\Lambda$ . When the temperature is varied, dislocations are emitted towards or away from the interface in order to relax thermal stresses. During heating, as the matrix is expanding more than the fiber, the thermal stress is relaxed by moving dislocations towards the interface. The mobility of the dislocations also increases upon heating, which contributes to an increase of  $C_I$ . In fig. 6.7a  $C_I$  continuously increases during heating, while in figs. 6.7b and 6.7c there is a decreasing trend above 400 K. In samples Mg/C<sub>45°</sub> and Mg/C<sub>0°</sub>, the modulus anomaly suggests that the radial displacement  $\Delta r_{dist}$  is smaller than the thermal contraction  $\Delta r_{th}$  at around 400 K (see § 4.5). This also means that the number of dislocations relaxing the thermal stresses decreases at this temperature. This is also confirmed in figs. 6.1b and 6.1c by the decrease of the damping, which is due to the motion of dislocations. For the sample Mg/C<sub>90°</sub> the damping increases with increasing temperature (fig. 6.1a) continuously, which is reflected by a continuous increase of  $C_I$  in this composite.

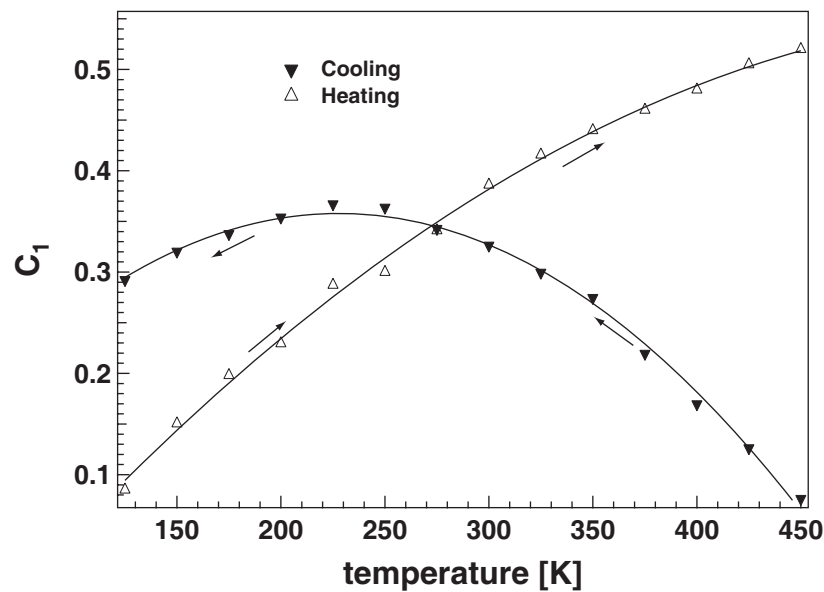


Fig. 6.7a:  $C_I$  as a function of temperature for the composite Mg/C<sub>90°</sub>.

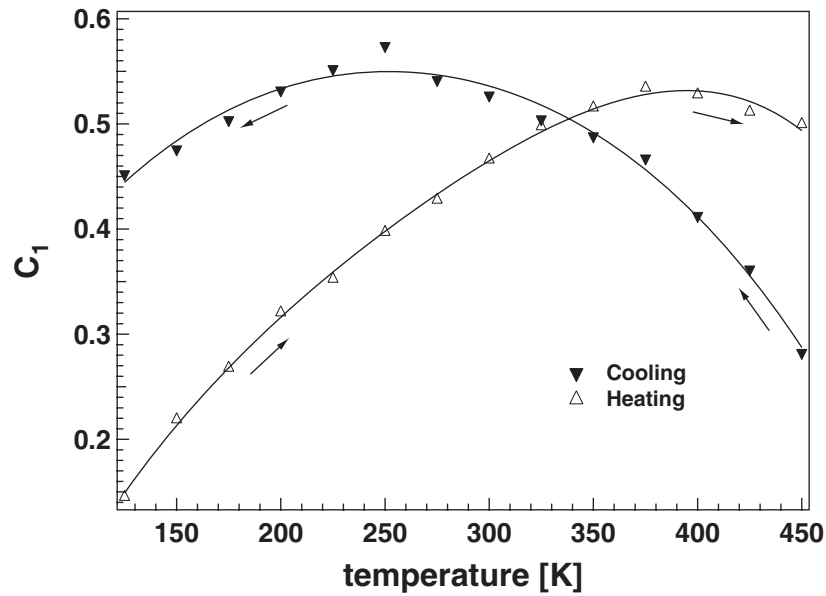


Fig. 6.7b:  $C_I$  as a function of temperature for the composite Mg/C<sub>45°</sub>.

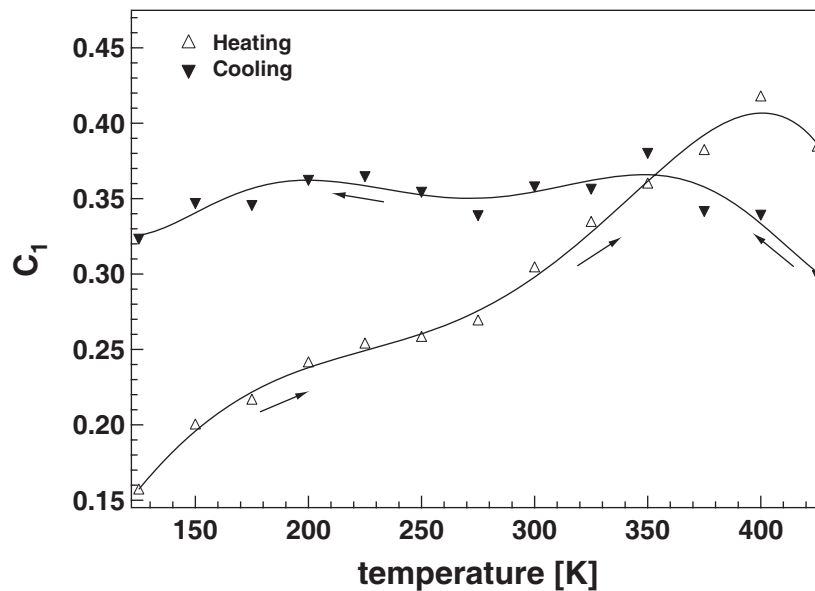


Fig. 6.7c:  $C_I$  as a function of temperature for the composite Mg/C<sub>0°</sub>.

During cooling, the matrix contracts more than the fibers and is under tensile stress. The mismatch in the thermal expansion coefficient between the matrix and the fibers is relieved by emitting dislocations away from the interface. During cooling, in the samples Mg/C<sub>45°</sub> and Mg/C<sub>90°</sub>,  $C_I$  increases, while for the sample Mg/C<sub>0°</sub> (fig.6.9c)  $C_I$  increases first and then it gets almost saturated. The same trend is observed in mechanical loss spectra (fig. 6.1) of these samples. As the gliding of the dislocations is favorable in the sample Mg/C<sub>0°</sub>, during cooling the dislocations come back and the total number of dislocations relaxing the thermal stresses is saturated. For all three samples below 200 K,  $C_I$  decreases during cooling. This occurs because at very low temperature the mobility of the dislocations is reduced.

Fig. 6.8 shows the evolution of the fitting parameter  $C_2$  with respect to the temperature during cooling and heating.  $C_2$  represents the interfacial bonding between the matrix and the reinforcement.  $C_2$  follows almost the same trend as the shear modulus for the three composites (fig. 6.9).

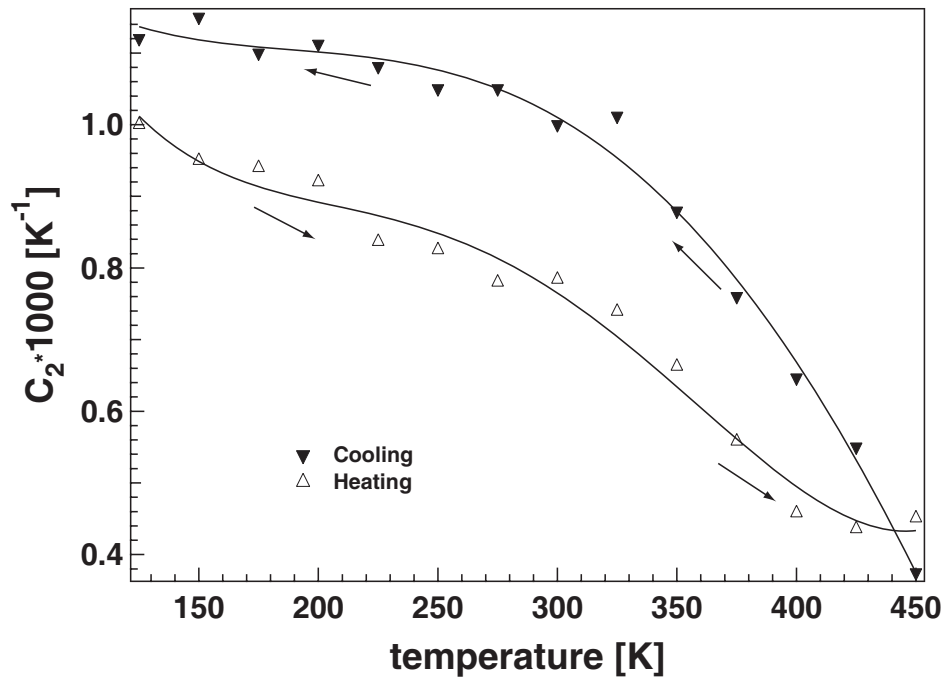


Fig. 6.8a:  $C_2$  as a function of temperature for the composite Mg/C<sub>90°</sub>.

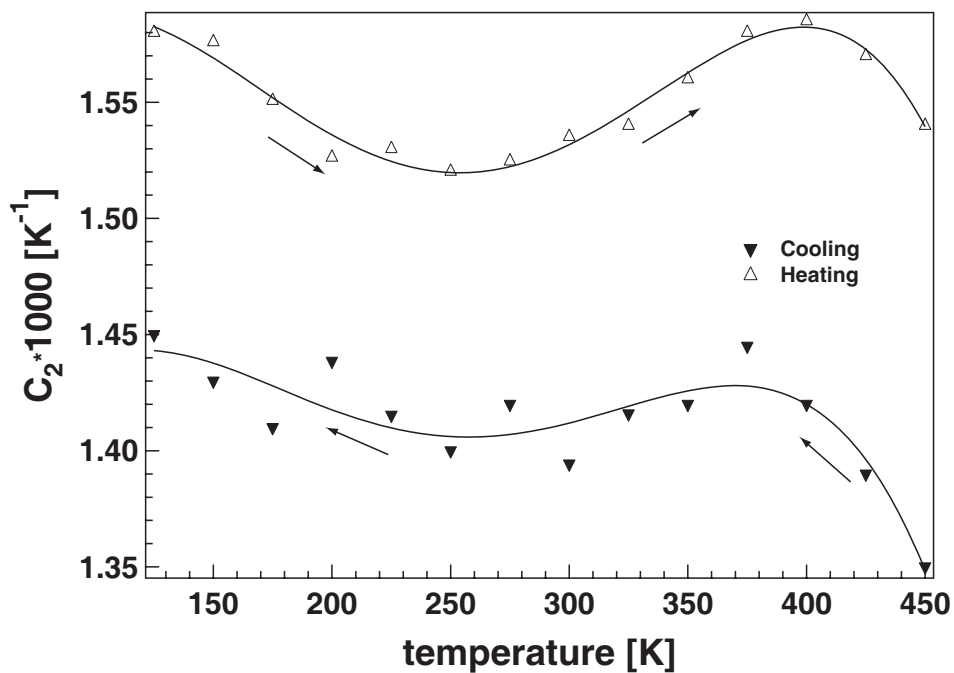


Fig. 6.8b:  $C_2$  as a function of temperature for the composite Mg/C<sub>45°</sub>.



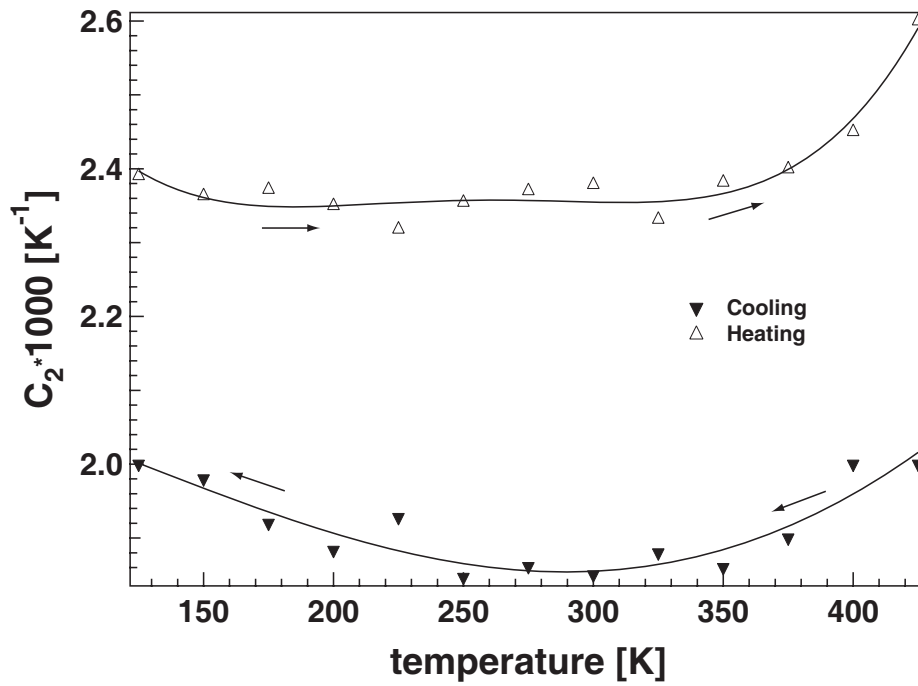


Fig. 6.8c:  $C_2$  as a function of temperature for the composite Mg/C<sub>0°</sub>.

In fig. 6.8a, for the sample Mg/C<sub>90°</sub>,  $C_2$  continuously decreases with increasing the temperature. The shear modulus of this composite (fig. 6.1a) shows the same trend. For the sample Mg/C<sub>45°</sub> it is observed that (fig. 6.8 b)  $C_2$  decreases first with increasing the temperature and then it increases at about 400 K and then it decreases again. In the sample Mg/C<sub>0°</sub> (fig.6.8c),  $C_2$  decreases first with increasing the temperature then it increases at about 400 K.

### 6.2.3 Effect of matrix orientation on the modulus anomaly

Fig. 6.9 shows the temperature dependence of the relative shear modulus for the three Mg/C composites with different orientations of the basal plane with respect to the matrix-fiber interface. The composite Mg/C<sub>90°</sub> shows a normal behavior, where the shear modulus decreases upon heating and increases upon cooling. The composite Mg/C<sub>45°</sub> shows an anomalous behavior between 350 K to 400 K, where the shear modulus curve shows a slope both upon heating and upon cooling. In the composite Mg/C<sub>0°</sub>, the modulus anomaly is more pronounced. Between 200 K and 425 K there is a large increase of the shear modulus during heating and a large decrease during cooling.

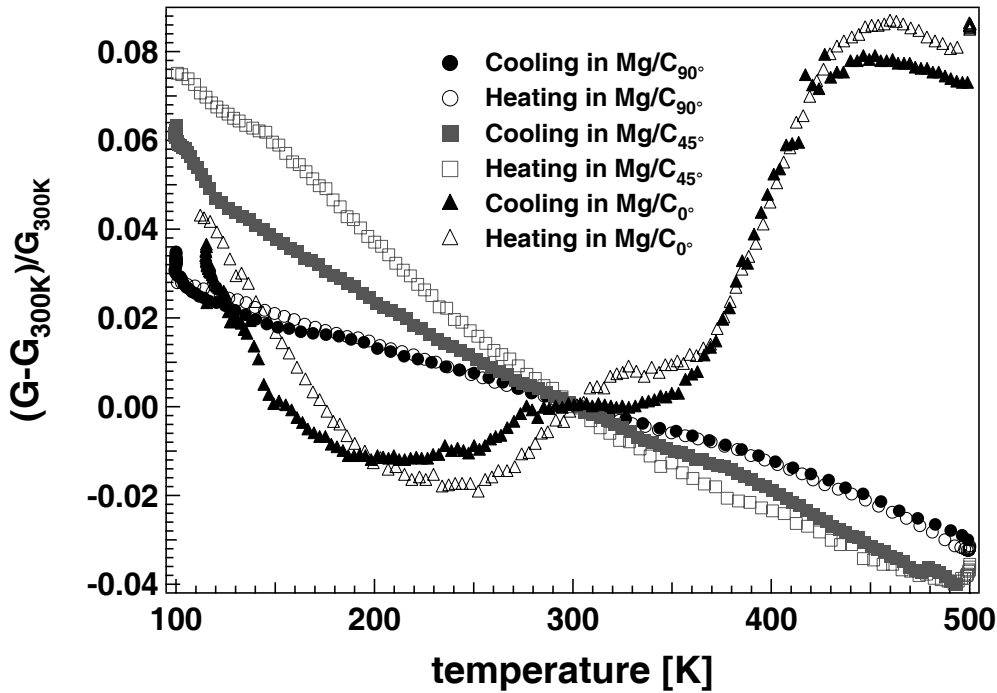


Fig. 6.9: Relative shear modulus as a function of temperature during cooling and heating for Mg/C composites with different orientations of the basal plane with respect to the matrix-fiber interface.

The composites  $\text{Mg/C}_{45^\circ}$  ( $\tan \gamma = 1$ ) and  $\text{Mg/C}_{0^\circ}$  ( $\tan \gamma = 0$ ) show a modulus anomaly because in each case the radial misfit

$$\Delta r_m = \Delta \alpha |\Delta T| r_0 \left( \frac{l_0}{r_0 \tan \gamma} - 1 \right) \geq 0 \quad (\text{eq. (4.6)}).$$

One should notice that eq. 4.6 just indicates a trend. Qualitatively, for  $\text{Mg/C}_{0^\circ}$ ,  $\tan \gamma \rightarrow 0 \Rightarrow \Delta r_m \rightarrow \infty$ , which is obviously unrealistic. For  $\gamma = 0$ , no dislocation is available to relax the thermal misfit in the z-direction. For the composite  $\text{Mg/C}_{90^\circ}$  ( $\tan \gamma = \infty$ ) the radial misfit term  $\Delta r_m < 0$ , which suggests no interfacial debonding. The experimental data are in agreement with this model. The same dislocations are responsible for the decrease of the interfacial bonding when they move away from the interface upon cooling and for an increase of bonding upon heating when they come back towards the interface.

#### 6.2.4. $C_1$ and $C_2$ parameters as a function of interface nature

As the parameters  $C_1$  and  $C_2$  are related to the interface thermal stress relaxation process, it is interesting to investigate how they depend on the interface nature. Therefore, another type of matrix-reinforcement interface has been studied, i.e., the interface in the composite Mg/steel (cf. §. 3).

In fig. 6.10, the transient mechanical loss  $\tan\phi_{Tr}$  is plotted as a function of  $\dot{T}/\omega$  for the composite Mg/steel. Even if the reinforcing steel fibers have a diameter 10 times larger than the C fibers with a much lower volumetric fraction, the behavior is the same. The experimental points are in agreement with the theoretical model developed here above. The two fitting parameters  $C_1$  and  $C_2$  are obtained by the fits using eq. 2.47 (fig. 6.11).

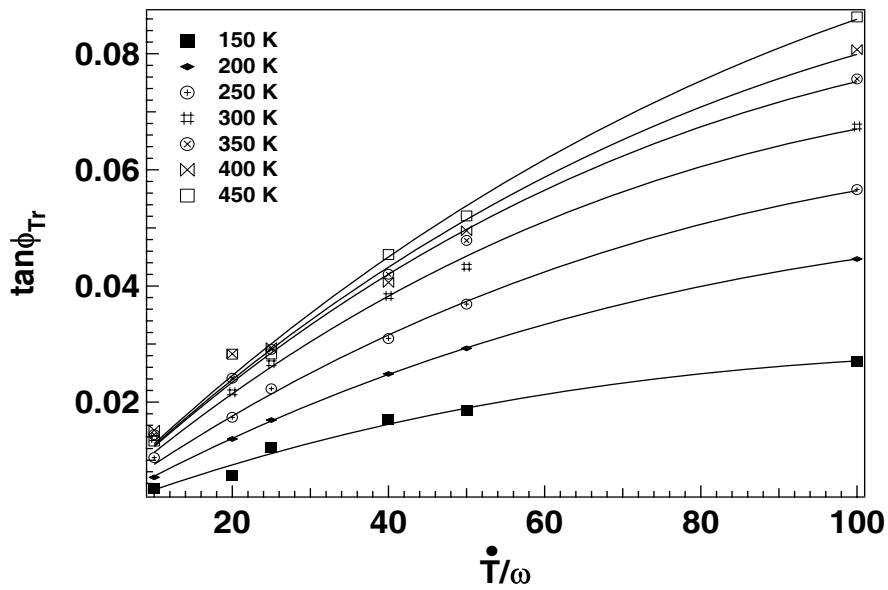


Fig. 6.10a: Transient mechanical loss  $\tan\phi_{Tr}$  for the Mg/steel composite as a function of  $\dot{T}/\omega$  for different temperatures during heating. The solid lines correspond to fitting curves at different temperatures.

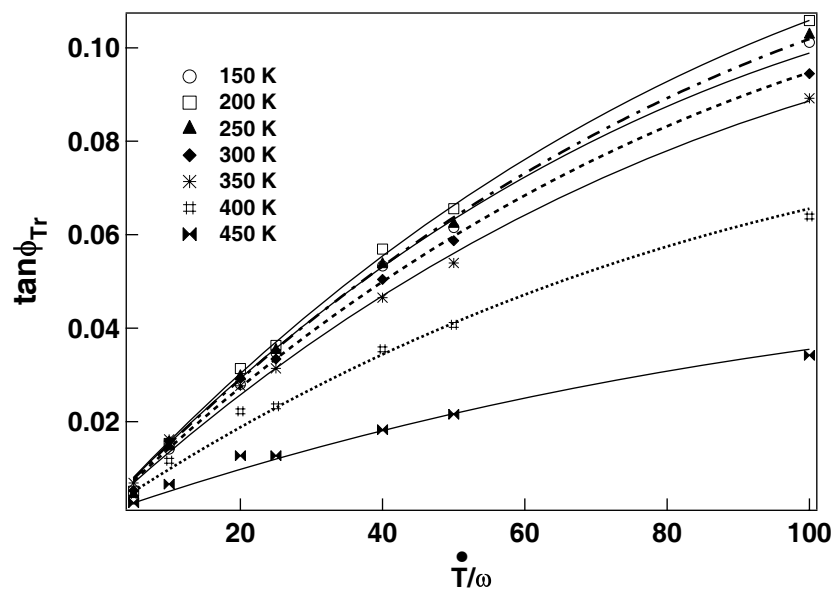


Fig. 6.10b: Transient mechanical loss  $\tan\phi_{Tr}$  for the Mg/steel composite as a function of  $\dot{T}/\omega$  for different temperatures during cooling. The solid lines correspond to fitting curves at different temperatures.

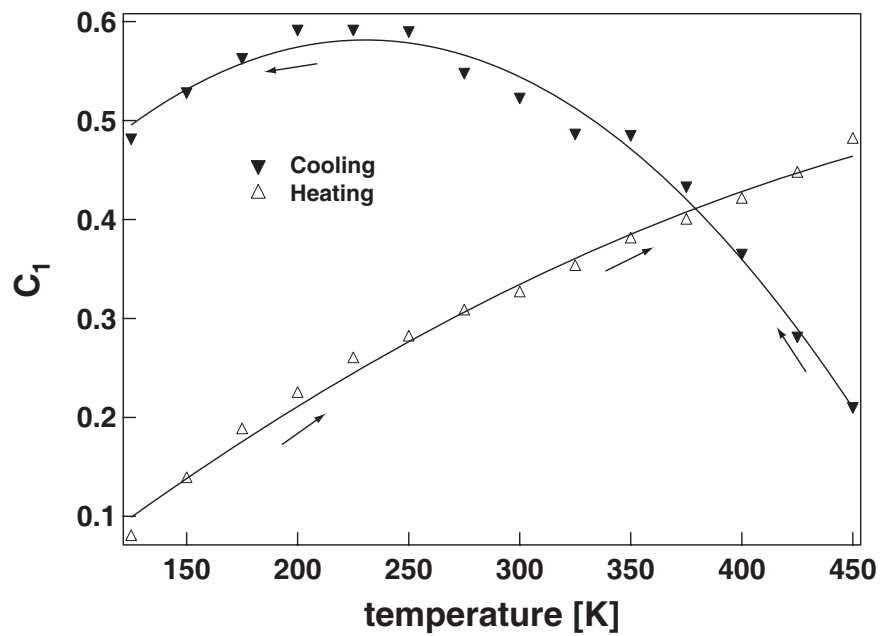


Fig. 6.11a:  $C_I$  as a function of temperature for the Mg/steel composite.

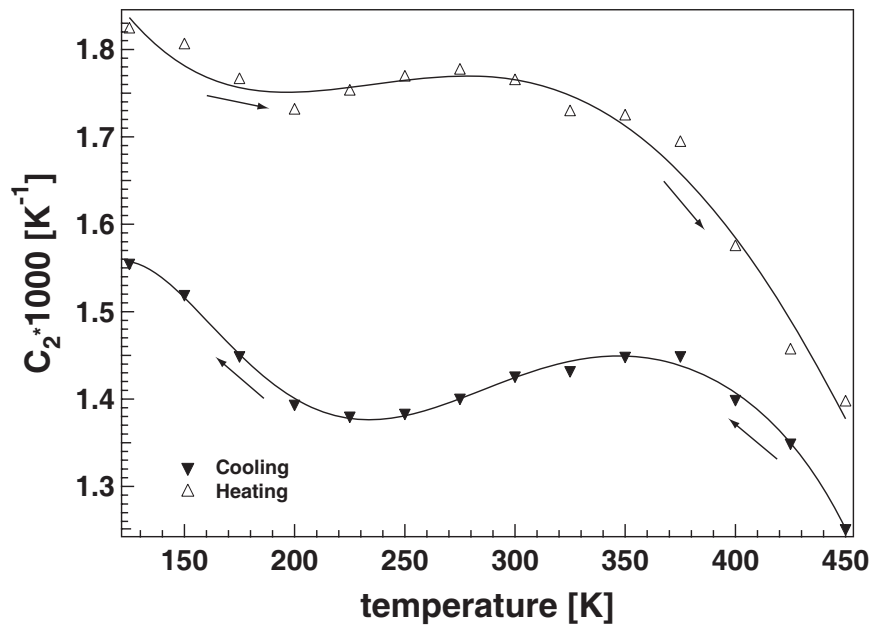
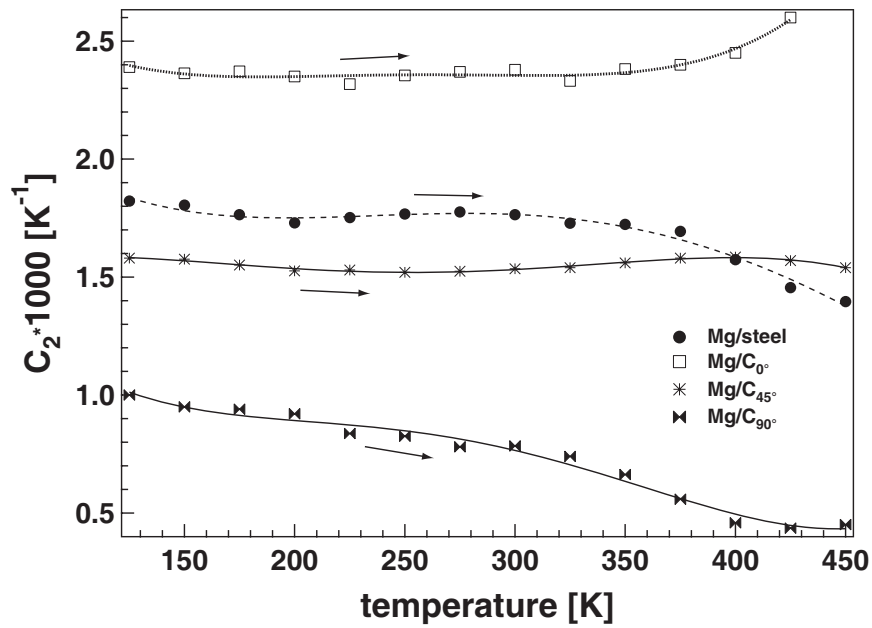
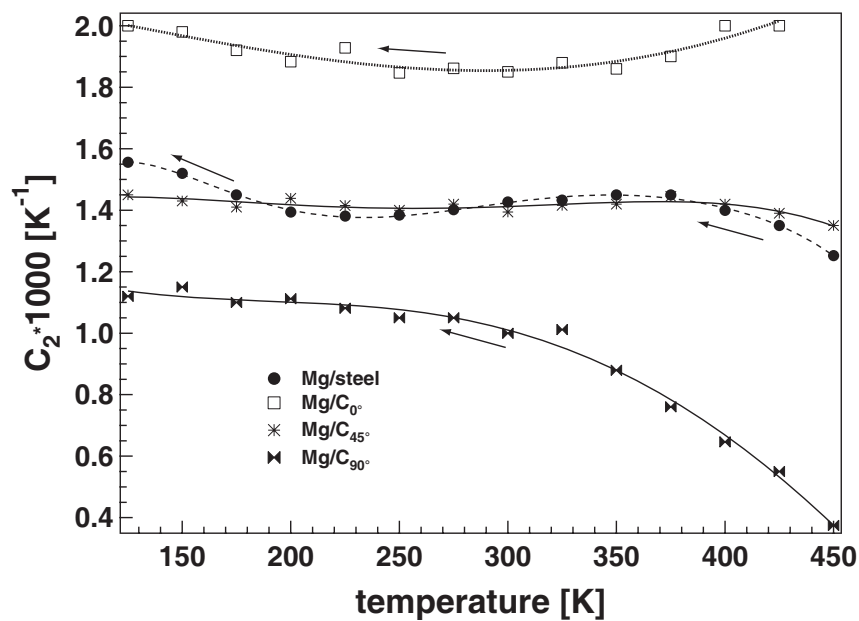


Fig. 6.11b:  $C_2$  as a function of temperature for the Mg/steel composite.

The behaviors of  $C_1$  and  $C_2$  as a function of temperature are shown in fig. 6.11a and 6.11b, respectively. The behavior of  $C_1$  in the case of Mg/steel composite is analogous to that of Mg/C<sub>45°</sub>, where the basal plane for these two composites makes an angle of 45° with respect to the matrix-fiber interface.

### 6.3 Interfacial response due to mechanical loss

Fig. 6.12 shows a comparison of the fitting parameter  $C_2$  for different composites between heating and cooling. The relative magnitude of  $C_2$  is maximum and minimum for Mg/C<sub>0°</sub> and Mg/C<sub>90°</sub>, respectively. It is interesting to notice that for Mg/steel and Mg/C<sub>45°</sub> the behavior of  $C_2$  is almost identical. These two composites were measured in the as-received state and one can consider that the basal planes of the polycrystalline matrix were almost identical for these two composites, which make on average an angle of 45° with respect to the matrix-fiber interface. At lower temperature,  $C_2$  is higher for Mg/steel than for Mg/C<sub>45°</sub>, while at higher temperature  $C_2$  decreases sharply for Mg/steel. This may be due to the size effect between the reinforcements. As the diameter of stainless steel fibers is almost 10 times larger than that of carbon fibers, their interfacial area is also much larger. Thus, the effects of bonding and debonding by contraction and expansion of the matrix, respectively, during thermal cycle is more pronounced in the Mg/steel composite. This effect is reflected by the anomalous behavior of the relative shear modulus observed in fig. 4.2.

Fig. 6.12a:  $C_2$  as a function of temperature during heating.Fig. 6.12b:  $C_2$  as a function of temperature during cooling.

## 6.4 Conclusion

Mechanical spectroscopy can be used to analyze the evolution of the microstructure and the matrix-fiber interfacial bonding as a function of temperature. Thermal stress relaxation in magnesium matrix composites is governed by the hysteretic motion of dislocations, which is interpreted by using a model based on friction in solid solution. The mechanical loss calculated from such a model is strongly time dependent. A transient damping component

that depends exponentially on heating/cooling rate is controlled by two fitting parameters  $C_1$  and  $C_2$ , which relates to the evolution of the mobile dislocation density and of the interfacial bonding with respect to the temperature, respectively. It is shown that the damping depends strongly on the orientation of the basal plane (001) of magnesium with respect to the matrix-fiber interface. Thus, by orientating the basal plane one can control the dislocation glide plane as well as  $C_1$  and  $C_2$  values. The anomalous behavior of the shear modulus is also reflected in  $C_2$  behavior, which also depends on the orientation of the glide plane.





## Chapter 7: General discussions

The aim of this work was to investigate the thermal stress relaxation at the interface of metal matrix composites by means of mechanical spectroscopy. Magnesium has been chosen as the matrix due to its high damping capacity, which is very desirable in the transportation and machine tools industry where reduction of noise is crucial. For improving the mechanical strength, magnesium has been reinforced with carbon or stainless steel fibers.

A systematic study of the mechanical loss spectra of magnesium matrix composites shows that the damping is clearly due to the motion of dislocations along the basal plane in the hcp structure of magnesium. In comparison with an aluminum matrix, magnesium has a lower number of slip systems, which gives rise to large dislocation loops. The energy dissipation due to thermal stresses in magnesium is due to the motion of these dislocation loops in the glide plane (Reihani 1980).

The mechanical loss spectra of the magnesium composites exhibit a thermal hysteresis, which is due to the inversion of the thermal stresses between heating and cooling. This is due to the fact that the same dislocations are relaxing the stresses at the interface. Due to the inversion of these thermal stresses between heating and cooling, the dislocations, which are relaxing these stresses, move in opposite directions upon heating and cooling and experience also different interaction forces during their motion. This reversible motion of dislocations improves the cyclic fatigue resistance.

The mechanical loss depends on the heating and cooling rate  $\dot{T}$  and on the excitation frequency. The mechanical loss increases with the heating rate  $\dot{T}$  and decreases by increasing the excitation frequency  $\omega$ . In the mechanical loss spectra, a transient damping depending on  $\dot{T}$  is superimposed on the isothermal equilibrium damping (Mayencourt 1998). The transient damping was always obtained by subtracting the mechanical loss for  $\dot{T} = 0$  from damping obtained for  $\dot{T} \neq 0$ , which corresponds to a thermal equilibrium. We have observed that this subtraction leads to a value  $\tan \phi_{tr} \neq 0$  for  $\dot{T} = 0$ , which contradicts the definition of transient damping.

The time evolution of the mechanical loss spectra shows that they can be separated into two regimes: a fast, linear one, known as transient damping, which depends on  $\dot{T}$  and instantaneously disappears when  $\dot{T} \rightarrow 0$ , and a slow exponential one related to the microstructure evolution, which is time dependent. Thus, the true transient mechanical loss is obtained by separating this exponential evolution from the complete mechanical loss spectra.

There was no temperature shift of the mechanical loss observed over a broad frequency range, which indicates that the relaxation phenomenon is athermal. A systematic study of the time dependent evolution of the microstructure relaxation shows that the thermal stress relaxation is athermal and follows the Granato-Lücke equation (Granato 1956). The thermal stress relaxation is due to the breakaway and gliding mechanism of dislocations from segregated point defects. The experimental points are in excellent agreement with the theoretical values. From the slope of the Granato-Lücke plot, a critical stress ( $\sigma_{0cr} = 0.216$  MPa) was calculated (Gremaud 1987, 2001).

To the best of our knowledge, this is the first time that the complete evolution of the mechanical loss as a function of the stress amplitude  $\sigma_0$  is obtained, where the mechanical loss first increases with the stress amplitude, reaching a maximum at  $\sigma_0 = \sigma_{0cr}$ , and then decreases. Previous results were obtained only for values  $\sigma_0 < \sigma_{0cr}$ , where the mechanical loss increases with increasing the stress amplitude. The same experiment on pure magnesium gives values only for  $\sigma_0 < \sigma_{0cr}$ . In effect, our findings may be interpreted as due to the fact that in composite materials thermal stresses due to fibers bias the applied stress, i.e., even if small they are high enough to overcome the breakaway threshold.

The athermal relaxation process observed in the magnesium matrix is very interesting for developing a material with high damping, as it can be utilized over broad frequency and temperature ranges.

The transient mechanical loss, due to the thermal stress relaxation by the motion of dislocations depends on the measurement parameters  $\omega$ ,  $\dot{T}$  and  $\sigma_0$ . This interpretation is in agreement with a number of other authors (Carenno-Morelli 2001, Vincent 1996). The experimental results show a non linear dependence of the transient damping on  $\frac{\dot{T}}{\omega\sigma_0}$ . The

model of Mayencourt and Schaller (Mayencourt 1998) allows one to distinguish between the thermal stress relaxation mechanisms controlled either by viscous friction or by solid friction. Fig. 2.10 shows the behavior of the transient mechanical loss as a function of the inverse of the frequency of oscillations (eq. 2.43), as controlled by a viscous friction mechanism. The behavior shows that the transient mechanical loss either diverges or is a linear function of the inverse of the frequency of oscillations for different B values (B being the coefficient of viscous gliding, which depends on temperature). However, this type of behavior of the mechanical loss was never observed in the case of magnesium matrix composites. The experimental points clearly show a non linear behavior as a function of the measurement parameters  $\frac{\dot{T}}{\omega\sigma_0}$ . The Mayencourt's model predicts a non linear behavior of the transient damping on  $\frac{\dot{T}}{\omega\sigma_0}$  when the relaxation is due to the solid friction mechanism. In fact, the experimental points were analogous to the first region of fig. 2.12, which shows the behavior of the transient mechanical loss as a function of  $\frac{\dot{T}}{\omega\sigma_0}$ , according to the Mayencourt's model.

The good fit of the experimental points with the theoretical model of Mayencourt suggests that the thermal stress relaxation in magnesium matrix composites is due to a solid friction mechanism, i.e., the pinning and depinning of dislocation segments from the segregated point defects. In fact, a systematic study shows that the intrinsic damping is also due to a solid friction mechanism that follows the Granato-Lücke model. We have shown that regardless of the reinforcement type, size and volume fraction, as well as matrix crystallographic orientation, the magnesium matrix composites exhibit a hysteretic damping.

The Mayencourt and Schaller's model has been applied to all the composites studied in this work, and it has been observed that the experimental points are well fitted by the theoretical curves. However, it can be seen that when  $\sigma_0 = 0$ , the right term in eq. 2.47 diverges. The equation for the transient damping does not hold when the applied stress is zero, since the dislocations move only when a coupling between the thermal stress and the applied stress is achieved.

The model predicts two fitting parameters  $C_1$  and  $C_2$  corresponding to the density of the mobile dislocations and to the interface profile and the strength of the interfacial bonding, respectively.

$C_1$  represents well the evolution of the dislocation microstructure versus the temperature for all the samples.  $C_1$  shows a thermal hysteresis between heating and cooling cycle, as the mechanical loss spectra. The evolution of  $C_1$  with temperature is analogous to that of the mechanical loss spectra, as  $C_1$  is proportional to the mobile dislocation density, and therefore to the transient mechanical loss.

The parameter  $C_2$  reflects the strength of the interfacial bonding as well as the geometry of the interface.  $C_2$  shows an anomalous behavior during heating and cooling, which is reflected in the relative shear modulus spectra, where an anomaly is observed between 350 K to 425 K. This has been attributed to the interfacial debonding resulting from the motion of dislocations relaxing the thermal stresses. It has been observed that the modulus anomaly depends strongly on the orientation of the basal plane. The higher the orientation of the basal plane favoring the easy gliding of the dislocations, the higher the modulus anomaly. The modulus anomaly depends also on the geometry of the reinforcements. It has been observed only for composites where the aspect ratio of fibers is large. Also, the shear modulus anomaly suggests that the interfacial strength decreases at lower temperature and increases at higher temperature. A weak interface is positive for material toughness because crack propagation is stopped at the soft interface. On the other hand, a strong interface may lead to crack propagation and then a brittle behavior can be observed. Thus, by considering the temperature dependence of the shear modulus and the fitting parameter  $C_2$ , one can conclude that a magnesium matrix is ideal because the interface is strong at high temperatures, where creep resistance is required, and weak at low temperatures, where toughness improvement is needed.

The magnesium matrix composites can also withstand a large number of cycles without exhibiting fatigue. This is due to the fact that the same dislocations are responsible for the relaxation of the internal stresses. In fact, Mayencourt has not observed any fracture of the Mg-2%Si/C composite after 150 000 cycles, while its modulus had decreased by <1%. In the Mg-2%Si/Al<sub>2</sub>O<sub>3</sub> composite, the modulus decreased during the first 100 000 cycles (Mayencourt 2002). After 120 000 cycles, the rate of modulus decrease suddenly increased,

and after 140000 cycles fracture of the sample occurred. This was due to the fact that in the Mg-2%Si/Al<sub>2</sub>O<sub>3</sub> composite too many impurities were present in the magnesium matrix, due to interfacial reaction. The damping capacity was then decreased and mechanical stresses were relaxed by damage accumulation, and so the fatigue resistance was not good. On the contrary, in the Mg-2%Si/C composite, which has a relatively pure Mg matrix, the damping capacity was high and the mechanical fatigue resistance was strongly increased. Also, Kiehn showed that the Mg-based AZ91-Saffil composite can withstand more than 1000 thermal cycles (Kiehn1994). The Mg/C and Mg/steel composites used in this work should also exhibit a strong mechanical and thermal fatigue resistance as the matrix is pure and SEM observation prevails that the bonding between the matrix and the fiber is only physical. No chemical reaction between the fiber and the matrix was observed.

The mechanical properties of composites depend strongly on the infiltration method and environment. In fact, for the Mg/TiC composites, it was observed that the mechanical strength of the composite increases with processing temperature by pressureless melt infiltration (Contreras 2004). Another work shows that the amount of porosity and the pore size of the preform affect the infiltration rate (Demir 2004). By controlling the fabrication procedure of Al<sub>2</sub>O<sub>3</sub>/SiC and infiltration conditions, high strength aluminum composites were obtained. Couteau has observed that the elastic modulus varies with the orientation of the fiber with respect to the matrix (Couteau 2004). He obtained for Mg/SiC<sub>long fibers</sub> a Young's modulus of 72 GPa and a shear modulus of 18.4 GPa and for Mg/Saffil<sup>TM</sup> a Young's modulus of 63 GPa.

From table 7.1 it can be seen that the Young's moduli obtained here for the Mg/steel and Mg/C composites are high compared to previous results (Couteau 2004). However, from the mixture law, the calculated Young's moduli for the Mg/C and Mg/steel composite are 243 and 96.67 GPa (measured by a free-free vibrating rod) and the shear moduli 24.33 GPa and 23 GPa, respectively. The experimental Young's modulus for the Mg/steel composite is very close to that obtained by a mixture law, while for Mg/C composite the modulus is too low. This is due to the fact that voids and porosity formed during the infiltration as well as during directional solidification process, which was observed by SEM and optical microscopic observations (fig.3.8). As we have measured the Young's modulus by means of bending tests, the interface plays a major role on the modulus of the composite. The experimental shear moduli for both composites were far too low from the calculated values. Again, the interface

quality is responsible for this discrepancy. A small amount of voids at the interface can reduce the modulus significantly.

Sample	Difference in CTE ( $\Delta\alpha$ ) K <sup>-1</sup>	Young's modulus (GPa)	Shear Modulus (GPa)	$C_2 \cdot 1000$ (K <sup>-1</sup> )	$C \cdot 10^{-7}$	$\frac{2}{3\pi} \cdot \frac{1}{C_2}$ at 300K	$\frac{\dot{T}}{\omega}$ max.
Mg/steel	6.28	95.78	19.75	1.43	0.21	148.39	100
Mg/C <sub>90°</sub>	24.08	150.22	11.68	1.0	2.49	212.21	200
Mg/C <sub>45°</sub>	24.08	165.95	12.05	1.39	3.13	152.67	133
Mg/C <sub>0°</sub>	24.08	151.24	7.48	1.86	4.6	114.09	100

Tab. 7.1: Different parameters measured for different composites.  $C_2$  was obtained at 300K with 0.9 MPa stress amplitude during cooling.

From eq. 2.47, it is observed that a nonlinear behavior of the transient mechanical loss as a function of  $\frac{\dot{T}}{\omega}$  is obtained for values  $\frac{\dot{T}}{\omega} < \frac{2}{3\pi} \cdot \frac{1}{C_2}$ . It is observed from table 7.1 that the

condition  $\frac{\dot{T}}{\omega} < \frac{2}{3\pi} \cdot \frac{1}{C_2}$  was always consistent with the experimental and the calculated values for all the composites.

From table 7.1, it is observed that the value of  $C$  is higher for the Mg/C composites than for the Mg/steel composite. From its definition (eq. 2.36),  $C$  takes into account the stress profile at the interface and the fiber concentration. The fiber concentrations in the Mg/C composites were much larger, due to the small diameter of fibers, which justifies the higher value of  $C$  for these composites. However,  $C$  also depends on the stress profile at the interface, which varies according to the orientation of the glide plane. In fact, the values of  $C$  in table 7.1 show that they are the highest for the composite Mg/C<sub>0°</sub>, followed by Mg/C<sub>45°</sub> and Mg/C<sub>90°</sub>, respectively. The same sequence is obtained for  $C_2$ , which reflects the interfacial strength. The experimental values of  $C_2$  indicate that a better interfacial strength can be obtained by orienting the matrix from the crystallographic viewpoint, in order to achieve the maximum

gliding condition for the dislocations. This is logical, as this condition will relax the maximum thermal stresses by the motion of dislocations without creating any debonding or crack propagation.

It is observed that besides the mechanical strength, the geometrical structure factor  $C$  is a very important parameter for determining the mechanical properties of a composite. As thermal stresses are proportional to  $C$ , it can give a quantitative analysis of the thermal stress relaxation at the interface of the metal matrix composites. It would be interesting to compare this parameter for different metal matrix composites with different mechanical strengths.





## Conclusion

Composites with magnesium reinforced with C or stainless steel fibers were processed by the gas pressure infiltration method. In some of the composites, the matrix was oriented with respect to the crystallographic viewpoint by means of the Bridgman method. The main objective of this work was to characterize the damping property as well as the microscopic structure of the matrix-reinforcement interface. Mechanical spectroscopy is particularly suitable, since it gives a measurement of macroscopic properties of the materials, like damping and dynamic modulus, and at the same time is very sensitive to the microscopic movements of the defects.

The experimental results show that the thermal stress relaxation in magnesium matrix composite is due to a hysteretic solid friction mechanism, regardless of reinforcement type, size and matrix crystallographic orientation. The transient mechanical loss was clearly distinguished from the isothermal intrinsic damping and time dependent microstructure evolution. The intrinsic damping of magnesium matrix composites is also due to a hysteretic solid friction mechanism that obeys the Granato-Lücke model. We have obtained the first complete behavior of the mechanical loss as a function of vibration amplitude.

The damping strongly depends on the orientation of the matrix glide plane, which also confirms that the main relaxation phenomenon in magnesium matrix composites is due to the motion of dislocations in the basal plane. The experimental results have validated the model of Mayencourt over a large range of parameter values. Taking into consideration the matrix crystallographic orientation, the model of Mayencourt has been modified. This model predicts two fitting parameters  $C_1$  and  $C_2$ , which are based on the mobile dislocation density and the interfacial geometry and bonding of the interface, respectively. The compared evolution of these two parameters as a function of temperature between different composites suggests that the damping as well as the interfacial strength depend strongly on the crystallographic orientation.

The results show that the anomalous behaviors of the fitting parameter  $C_2$  as well as of the relative shear modulus for the magnesium matrix composites are due to the interfacial debonding caused by the relaxation of the thermal stresses by the motion of dislocations. The

interfacial bonding as well as the elastic shear modulus depend strongly on the orientation of the glide plane. The particular character of the interfacial bonding in Mg based MMC provides a great potential of application. Indeed, the interface strength decreases at low temperatures, allowing for a better toughness, whereas it increases at high temperatures, improving the creep resistance.

## References

- Aghdam A. A., Falahatgar S.R., Com. Str., 66, 415-420, (2004)
- Arsenault R J., Fisher R., Scripta Metall. 17, 67-71, (1983)
- Arsenault R.J., Taya M., Metal Matrix Composites: thermo mechanical behavior. Pergamon Press, Oxford, (1989)
- Arsenault R.J., Wang L., Feng C., Acta Metall. Mater. 39, 47-57, (1991)
- Ashbee K., Fundamental Principles of Fiber Reinforced Composites, Technomic Publishing Co., Basel, (1993)
- Ashby M., Jones D., Engineering Materials, Oxford: Butterworth-Heinemann, Oxford, 1996
- Babout L., Bréchet Y., Maire E., Fougères R., Acta Mater., 52, 4517-4525, (2004)
- Carreno-Morelli E., Cutard T., Schaller R., Bonjour C., Mat. Sci. Eng. A, 251, 48-57, (1998)
- Carreno-Morelli E., Urreta S.E., Schaller R., Sci. & Eng. of Composite Materials, 8, No. 1, 45-53, (1999)
- Carreno-Morelli E., in Mechanical Spectroscopy  $Q^{-1}$  2001 with Applications to Material Science, R. Schaller, G. Fantozzi, G. Gremaud, Eds., Mater. Sci. Forum (Transtech Publications LTD) p.570, (2001)
- Chan K.S., Davidson D.L., Eng. Frac. Mec. Vol. 33, No. 3, 451-466, (1989)
- Chawla K.K., Esmaeli A., Datye A., Vasudevan A., Scripta Metall. 25, 1315-1319, (1991)
- Chawla N., Chawla K.K., Metal Matrix Composites, Springer, (2006)
- Chmelík F., Lukác P., Kiehn J., Mordike B.L., Kainer K.U., Langdon T.G., Mat. Sci. Eng. A, 325, 320-323, (2002)
- Chowdhury A. S. M. Fahim, D. Mari, R. Schaller, Mat. Sci. Eng. A, 521-522, 310-313, (2009)

- Chowdhury A. S. M. Fahim, D. Mari, R. Schaller, Phys. Stat. Sol. (a) 205 No. 2, 249-254, (2008)
- Christman T., Suresh S., Acta Metall., 36, 1691-1704, (1988)
- Clyne .T.W., Mason J.F., Metal. Trans. A 18, 95, (1987)
- Clyne T.W., Withers P., An Introduction to Metal Matrix Composites, Cambridge University Press, New York, (1993)
- Contreras A., Lòpez V.H., Bedolla E., Scripta Mater. 51, 249-253, (2004)
- Couteau O., Schaller R., Mat. Sci. & Eng. A, 387-89, 862-866, (2004)
- Daehn G., Andersson P., Hongyang H., Scripta. Metall. 25, 2279, (1991)
- Davidson D.L., Chan K.S., Mcminn A. and Leverant G.R., Metal. Trans. A. 20 A, 2369-2378, (1989)
- Demir A., Altinkok N., Com. Sci. & Tech. 64, 2067-2074, (2004)
- Derby B., Proc. 12<sup>th</sup> RISO International Symposium on Material Science, 31, (1991)
- Dinwoodie J., Moore E., Langman C.A.J., Symes W.R., Fifth Chemical International Conference on Composite Materials, San Diego, California, U.S.A., (1985)
- Durante S., Rabezzana F., Rutelli G., Surface and Coating Technology, 94-95, 632-640, (1997)
- El-Al F. Abed, Göken J., Riehemann W. and Mordike B.L., Proc. Magnesium Alloys and their Applications, 351-356, (1998)
- Fantozzi G., Esnouf C., Reihani Seyed S.M., Revel G., Acta Metall., 32, No.12, 2175-2183, (1984)
- Fleteren R. V., Adv. Mater. and Processes, 5, 33, (1996)
- Gang L., Zhehua Z., Shang J., Acta. Metall. 42, 271, (1994)
- Ghosh A.K., Fundamentals of Metal Matrix Composites, Butterworth-Hinemann, Stoneham, MA, pp 3-22, (1993)

- Garcés G., Rodríguez M., Pérez P., Adeva P., Com. Sci. & Tec. 67, 632-637, (2007)
- Granato A., Lüke K., J. Appl. Phys., 27, 583, (1956)
- Gremaud G., Journal de Physique Colloques 48, Tome C8, N° 12, (1987)
- Gremaud G., in Mechanical Spectroscopy Q<sup>-1</sup> 2001 with Applications to Material Science, R. Schaller, G. Fantozzi, G. Gremaud, Eds., Mater. Sci. Forum (Transtech Publications LTD) p.218, (2001)
- Gu J., Zhang X., Gu M., Gu M., Wang X., J. of Alloys Compd. 372, 304-308, (2004)
- Gu J., Zhang X., Gu M., Mater. Letters., 58, 1952-1955, (2004)
- Gu J., Zhang X., Qui Y., Gu M., Com. Sci. & Tec., 65, 1736-1742, (2005)
- Gutiérrez I.-U., Nó M.L., San Juan J., Mat. Sci. Eng., A, 370, 555-559, (2004)
- Hamann R. and Fougères R., Proc. 12<sup>th</sup> RISO, 373-378, (1991)
- Hack J.E., Page R.A. and Leverant G.R., Metall. Trans. A, 15 A, 1389-1396, (1984)
- Hull D., Clyne T.W., An Introduction to Composite Materials. Cambridge University Press, Cambridge, (1996)
- Janczak J., Schaller R., Kulik A. Proc. 1st Int. Conf. on Composite Engineering, New Orleans, 767-768, (1994)
- Jiang Z., Li G., Lian J., Ding X., Sun J., Com. Sci. & Tec., 64, 1661-1670, (2004)
- Kiehn J., Köhler C., Kainer K.U., Key Eng. Mater. 97-98, 37, (1994)
- Kiehn J., Trojanová Z., Lukác P., Kainer K.U., Key Eng. Mater, Vols. 127-131, 993-1000, (1997)
- Kim W., Koczak M., Lawley A., Proc. New Developments and Applications in Composites, St. Louis, 41, (1978)
- Kim W., Koczak M., Lawley A., Scripta Metall. 25 2359, (1991)

- Kumar S., Mondal A.S., Dieringa H., Kainer K.-U., *Com. Sci. & Tech.*, 64, 1179-1189, (2004)
- Kúdela S., Oswald S., Kúdela S. Jr., Baunack S., Wetzig K., *J. of Alloys. Compd.*, 378, 127-131, (2004)
- Kurz W., Fischer D.J., *Fundamentals of Solidification*, Trans Tech Publications, (1984)
- Lu L., Lim C.Y.H., Yeong W.M., *Com. Str.*, 66, 41-55, (2004)
- Luo A., *Metall. Mater. Trans. A*, 26 A, 2445-2455, (1995)
- Levitt A.P., Di Cesare E. and Wolf S.M., *Metall. Trans.*, 3, 2455-2459, (1972)
- Llorca J., Ruij J., Healy J.C., Elices M. and Beevers C.J., *Mat. Sci. Eng. A185*, 1-15, (1994)
- Lloyd D.J., in *Composites Engineering Handbook* (P.K. Mallick, ed.) Marcel Dekker, New York, pp 631-669, (1997)
- Mahesh S., Hanan J.C., Üstündag E., Beyerlein. I.J., *Int. J. of Sol. and Str.*, 41, 4197-4218, (2004)
- Masur L.J., Mortensen A., Cornie J.A., Flemings M.C., *Metall. Trans. A*, 20 2549, (1989)
- Mayencourt C., Schaller R., *Mat. Sci. Eng. A*, 325, 1-2, 286-291, (2002)
- Mayencourt C., Schaller R., *Acta Mater*, 46, 6103, (1998)
- Mayencourt C., Schaller R., *Phys. Stat. Sol. (a)*, 163, 357, (1997)
- Mayencourt C., Thèse no. 2060, (EPFL), page 28, (1999)
- Menet P., Bréchet Y., Dumant X., 12th RISO International Symposium on Material Science, 523, (1991)
- Miracle D.B., Donaldson S.L., editors, *ASM Handbook: Composites, Volume 21*, ASM International, Material Park, (2001)
- Miserez A., Rossol A., Mortensen A., *Acta Mater*, 52, 1337-1351, (2004)
- Mortensen A., Cornie J. A., Flemings M.C., *J. Met.* 40, 12, (1988)

- Mortensen A., Masur L. J., Cornie J.A., Flemings M.C., Metall. Trans. A. 20 2535, (1989)
- Mortensen A., Pedersen O.B. and Lilholt H., Scripta Mater., 38, No 7, 1109-1115, (1998)
- Nakanishi M., Nishida Y., Matsububara H., Yamasda M., Tozaya Y., J. Mat. Sci. Lett. 9, 470, (1990)
- Nó M.L., Oleaga A., Esnouf C., San Juan J., Phys. Stat. Sol. (a) 120, 419 (1990)
- Nowick A., Berry B., Anelastic Relaxation in Crystalline Solids, Academic Press, New York, (1972)
- Parke S., British Journal of Applied Physics 17, 271, (1966)
- Parrini L., Schaller R., Metall. Mater. Trans. A, 26 A, 1457, (1995)
- Parrini L., Thesis no. 1420, Ecole Polytechnique Fédérale de Lausanne, Suisse, (1995)
- Parrini L., and Schaller R., Acta Mater, 44, 4881 (1996)
- Patterson W., Taya M., Proc ICMM 5, ed Harrigan W., Warrendale, 53, (1989)
- Pérez P., Garcés G., Adeva P., Com. Sci. & Tec., 64, 145-151, (2004)
- Rack H., proc. 6th Int. Conf. on Composite Materials, New York, Elsevier, 382, (1987)
- Rao S., Mechanical vibrations, Addison-Wesley, Reading, (1990)
- Reihani Syed S.M., Fantozzi G., Esnouf C. and Revel G., Scripta Metall., 13, 1011-1015, (1979)
- Reihani Syed S.M., Esnouf C., Fantozzi G. and Revel G., J. de Physique Tome 42, C5, 145-150, (1981)
- Reihani Syed S.M., Thèse, Université Claude Bernard Lyon I, France, (1980)
- Riehemann W., in: B.L. Mordike, K.U. Kainer (Eds.) Magnesium Alloys and their Applications, Werkstoff-Informationen-Gesellschaft MbH, Frankfurt, p. 61, (1998)
- Ritchie I., Pan Z-L., Sprungmann K.W., Schmidt H.K., Dutton R., Can. Metall Q, 26, 239-50, (1987)

- Rohatgi P., Advances in MMCs. Adv. Mat. Proc., 137: 39-44, (1991)
- Sallit I., Richard C., Adam R., Robbe-Valloire F., Materials Characterization, 40, 169-188, (1998)
- San Juan J. in Mechanical Spectroscopy  $Q^{-1}$  2001 with Applications to Material Science, R. Schaller, G. Fantozzi, G. Gremaud, Eds., Mater. Sci. Forum (Transtech Publications LTD) p.416, (2001)
- Schäff W., Proc. 12<sup>th</sup> International Conference of Composite Materials, (1999)
- Schaller R., Fantozzi G., Gremaud G., Mechanical Spectroscopy  $Q^{-1}$  2001, Transtech publications, Zurich, (2001)
- Schwartz M., Composite Materials: processing, fabrication and applications, Vol. 2, Prentice-Hall, London, (1996)
- Schwarz R.B., Funk L.L., Acta Metall. 31, p. 299, (1983)
- Sugimoto K., Niiya K., Okamoto T. and Kishitake K., Trans. Jpn. Inst. Met., 18, 277-288, (1977)
- Sugimoto K., Inst. Sci. Ind. Res., Osaka Univ., 35, 31-44, (1978)
- Suresh S., Christman T., Sugimura Y., Scripta Metall. 23, 1599, (1989)
- Taya M., Arsenault R. J., Metal Matrix Composites, Thermomechanical behavior, Pergamon Press, P. 103, (1989)
- Trojanová Z., Lukác P., Riehemann W. and Mordike B.L., Mat. Sci. Eng. A226-228, 867-870, (1997)
- Trojanová Z., Lukác P., Riehemann W. and Mordike B.L., Proc. Magnesium Alloys and their Applications, (1998)
- Trojanová Z., Gärtnerová V., Lukác P., Drozd Z., J. of Alloys Compd., 378, 19-26, (2004)
- Vittoz B., Secrétan B., Martinet B., Zeitschrift für Angewandte Mathematik und Physik 14, 46, (1963)
- Wren G.G., Kinka V.K., J. Mater. Sci., 30, 3279-3284, (1995)



Xiaonong Z., Di Z., Renjie W., Zhengang Z. and Can W., *Scripta Mater.*, 37, 1631-1635, (1997)

Xin X.J., Daehn G.S. and Wagner R.H., *Acta Mater.*, 45, No. 5, 1821-1836, (1997)

Xiuqing Z., Haowei W., Lihua L., Naiheng M., *Com. Sci. & Tec.*, 67, 720-727, (2007)

Zener C., *J. of Appl. Phys.* 18, 1022, (1947)

Zweben C., National Electronic Packaging and Production Conference, Boston, (1988)



## Appendix

The model of Mayencourt and Schaller interprets the relaxation of thermal stresses at the interface of metal matrix composites by the motion of dislocation controlled by a solid friction mechanism. However, the model was independent of the orientation of the matrix glide plane. A modification of the model elaborated in this work as described in chapter 6.2, eq. 6.15 is describe here.

Due to the mismatch of thermal expansion coefficient between the fibers and the matrix ( $\Delta\alpha = \alpha_m - \alpha_f$ ), internal thermal stress appears at the interface of the metal matrix composites. The thermal stress ( $\sigma_{th}$ ) is expressed as

$$\sigma_{th} = CE\Delta\alpha\dot{T}t \quad (A.1)$$

Where  $C$  is a geometrical factor that takes into account the stress profile at the interface and the fiber concentration.  $E$  is the Young's modulus,  $\Delta\alpha$  is the mismatch of thermal expansion coefficient and  $\dot{T}$  is the heating or cooling rate.

The component of the applied mechanical stress ( $\sigma_m$ ) along the glide plane is

$$\sigma_m = \sigma_0 \sin(\omega t) \cos \gamma \quad (A.2)$$

Then the total stress ( $\sigma_{tot}$ ) acting on the dislocation segment is

$$\sigma_{tot} = \sigma_m + \sigma_{th} \quad (A3)$$

When the applied stress and the thermal stress are in the same direction, these stresses are coupled, which is intense enough to induce breakaway of dislocation segments from immobile point defects and the dislocation can glide. Thus a dislocation can glide only in the half cycle where the applied stress is in the same direction as the thermal stress. Due to the hysteretic motion, the dislocation will not move back when the total stress is lower than the

critical stress. Therefore the dislocation stops. Thus the dislocation motion takes place only between a part of the period  $t_1$  and  $t_2$  as shown in fig. A1.

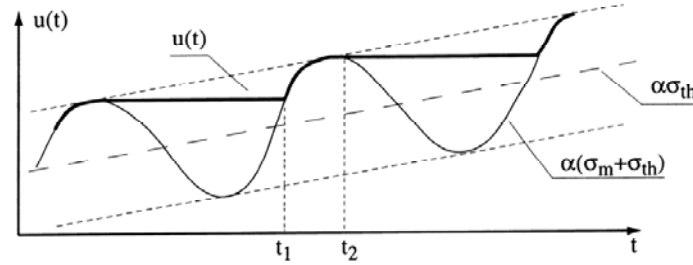


Fig: A1: Dislocation displacement as a function of time for the case of solid friction. Periodic stress is superimposed to an increasing thermal stress that is obtained by temperature scan. Dislocation can move only between  $t_1$  and  $t_2$  where the stress acting on the dislocation is higher than the critical stress necessary for the breakaway of the dislocation segment.

The motion of the dislocations leads to a relaxation that balances exactly the thermal and the mechanical stress

$$\sigma_r = \sigma_{th} + \sigma_m \quad (A4)$$

with

$$\sigma_r = \frac{Ku}{b} \quad (A5)$$

where  $\sigma_r$  is the relaxed part of the stress,  $K$  is the relaxation coefficient,  $b$  is the Burger's vector and the mean dislocation movement  $u$  is expressed as:

$$u = \frac{b}{K} (CE\Delta\alpha\dot{T}t + \sigma_0 \sin(\omega t) \cos \gamma) \quad (A6)$$

Applying the Orowan equation, the anelastic strain can be calculated as

$$\varepsilon = \frac{\Lambda b^2}{K} (CE\Delta\alpha\dot{T}t + \sigma_0 \sin(\omega t) \cos \gamma) \quad (A7)$$

Where  $\Lambda$  is the mobile dislocation density. The transient mechanical loss can be calculated as

$$\tan \phi_{Tr} = \frac{1}{\pi J_{el} \sigma_0^2} \oint \sigma d\varepsilon_{an} \quad (A8)$$

This equation cannot be solved analytically. A good and soluble approximation is obtained by taking an approximation of triangular excitation of a sinusoidal one:

$$\sigma_m = \frac{2\omega \sigma_0 \cos \gamma}{\pi} t \quad 0 < t < \frac{\pi}{2\omega} \quad (A9)$$

Then the transient mechanical loss can be written as

$$\tan \phi_{Tr} = \frac{\Lambda b^2}{\pi J_{el} K} \left( \frac{4\omega^2}{\pi^2} \right) \cos \gamma \left( 1 + \frac{\pi}{2} CE \Delta \alpha \frac{\dot{T}}{\omega \sigma_0 \cos \gamma} \right) \frac{1}{2} [t_2^2 - t_1^2] \quad (A10)$$

The dislocation moves only between  $t_1$  and  $t_2$ , which gives

$$\varepsilon \left( t_1 + \frac{2\pi}{\omega} \right) = \varepsilon(t_2) = 0 \quad (A11)$$

For low values of  $\frac{\dot{T}}{\omega}$ ,  $t_1$  and  $t_2$  lies between 0 and  $\frac{\pi}{2\omega}$ , where time  $t_2$  corresponds to maximum local deformation and can be written as  $t_2 = \frac{\pi}{2\omega}$ .

Then from eqs. A7 and A11, one can calculate

$$t_1 = \frac{\sigma_0 \left( 1 - \frac{3}{2} \pi CE \Delta \alpha \frac{\dot{T}}{\omega \sigma_0 \cos \gamma} \right)}{\frac{2\omega}{\pi} \sigma_0 \left( 1 + \frac{\pi}{2} CE \Delta \alpha \frac{\dot{T}}{\omega \sigma_0 \cos \gamma} \right)} \quad (A12)$$

Putting the values of  $t_1$  and  $t_2$  into eq. A.10 one can calculate the transient mechanical loss, that depends on the orientation of the glide plane of the matrix

$$\tan \phi_{Tr} = 2C_1C_2 \cos \gamma \left( \frac{\dot{T}}{\omega} \right)^{\frac{1 - \frac{\pi}{2}C_2 \frac{\dot{T}}{\omega \cos \gamma}}{1 + \frac{\pi}{2}C_2 \frac{\dot{T}}{\omega \cos \gamma}}} \quad (\text{A13})$$

$$\text{with } C_1 = \frac{\Lambda b^2}{J_{el}K} \quad \text{and} \quad C_2 = \frac{CE\Delta\alpha}{\sigma_0}$$

## Acknowledgements

Thanks to the Almighty Allah who enabled me to accomplish this work.

I would like to express my deep gratitude to Prof. Robert Schaller for giving me the opportunity to work in his group. His continuous guidance and encouragement facilitated me to complete this work. Prof. Schaller was always with ideas and thoughts. His enthusiasm towards work always motivated me. It was a real pleasure to work with him.

I am extremely grateful to Dr. Daniele Mari. My office was next to his office, which was always open for discussions. He was open minded and ready to give immediate feedbacks.

Many thanks to Prof. Gerard Gremaud for helping during the teaching activities. Dr. Iva Tkalcic deserves special acknowledgement. She spent a lot of time for helping me regarding the experimental trouble shooting. Also many thanks to Dr. Claudia Ionascu and Mehdi Mazaheri for helping me taking SEM pictures, and John Hennig for interesting theoretical discussions. I would like to thank Dr. Ronan Martin and Alessandro Sellerio for their valuable advices for writing the thesis.

I would like to thank Mr. Bernard Guisolan, Mr. Guillaume Camarda, Mr. Gérald Beney, and Mr. Antonio Gentile for the fabrication and the polishing of the samples, and Madam Monique Bettinger, Madam Caroline Pletscher, and Madam Evelyn Ludi for all the administrative works. In the moment of need they were always available with a big smile.

I am indebted to my teacher Prof. Habibul Ahsan and my uncle Mr. Shamsul Majid Choudhury for their advice and support.

Without having the continuous moral support and love from my parents and my dear wife Tamanna, it would have been impossible for me to be here. On this occasion, I would like to convey my deep gratitude to them.





## Curriculum Vitae

**Abu Salek Md. Fahim Chowdhury**

Born in Sylhet, Bangladesh on the 7<sup>th</sup> November, 1978

### EDUCATION

---

- 2005-2009**    École Polytechnique Fédérale de Lausanne (EPFL), Switzerland  
Assistant doctorant at the Institute of Complex Matter Physics.
- 2002-2005**    Diplom-Physik (Masters in Physics), University of Hannover, Germany.
- 1996-1999**    B.Sc. (Honors) in Physics, Shahjalal University of Science & Technology  
Sylhet, Bangladesh.

### RESEARCH & TEACHING EXPERIENCES

---

- 10/2005-at present**    École Polytechnique Fédérale de Lausanne (EPFL), Switzerland  
Research assistant  
Teaching assistant for the course “ Travaux pratique”
- 10/2003-02/2005**    Center for Radiation Protection & Radioecology,  
University of Hannover, Germany  
Research Assistant

### AWARDS

---

- **ICSC, World Laboratory Scholarship**, Lausanne, Switzerland, 2004 for the diplom thesis.
- **Book Prize**, Shahjalal University of Science & Technology, 1999 was rewarded for securing the highest GPA in the bachelor exam.

## CONFERENCE

---

**July 2008** 15<sup>th</sup> International Conference on Internal Friction and Mechanical Spectroscopy  
Perugia, Italy, “Analysis of transient mechanical loss due to thermal stresses  
in metal matrix composites”, A.S.M.F. Chowdhury, D. Mari, and Schaller

## LIST OF PUBLICATIONS

---

1. The effect of the orientation of the basal plane on the mechanical loss in magnesium matrix composites studied by mechanical spectroscopy, A.S.M.F. Chowdhury, D. Mari, and R. Schaller, Acta Materialia, accepted.
2. Thermal stress relaxation in magnesium matrix composites studied by dislocation breakaway, A.S.M.F. Chowdhury, D. Mari, and R. Schaller, Composite Science & Technology, in press.
3. Analysis of transient mechanical loss due to thermal stresses in metal matrix composites, A.S.M.F. Chowdhury, D. Mari, and R. Schaller, Mat. Sci. and Eng. A, 521-522 (2009) 310-313.
4. Thermal stress relaxation in magnesium matrix composites studied by mechanical spectroscopy, A. S. M. F. Chowdhury, D. Mari, R. Schaller, Phy. Stat. Sol. (a), 205, 2, (2008), 249 – 254.
5. Production of Residual Nuclides from Tungsten by Proton-Induced Reactions up to 70 MeV, R. Michel, A.S.M.F. Chowdhury, Z. Ullah, U. Herpers, U. Otto, E. Boltz, Progress Report on Nuclear Data Research in the Federal Republic of Germany, (2005), 31-34.

